POLITECNICO MILANO 1863

SCUOLA DI INGEGNERIA INDUSTRIALE
E DELL'INFORMAZIONE

EXECUTIVE SUMMARY OF THE THESIS

Micro-compressive testing and synchrotron-based damage analysis of human trabecular bone

LAUREA MAGISTRALE IN MATERIALS ENGINEERING AND NANOTECHNOLOGY

Author: Federico Renolfi, Sara Zilioli

Advisor: Prof. Laura Maria Vergani

Co-advisor: PhD Candidate Federica Buccino

Academic year: 2020-2021

---

1. Introduction

The study of bone multi-scale structure and its pathologies have crescent interest in medical research, due to its impact on public health costs and everyday life of patients. Femur, especially, holds a central role in many studies, since its fracture brings to a high number of surgeries and hospitalizations every year. The estimated annual direct costs in the EU are €24 billion, rising to €37 billion per year accounting for the indirect costs of care and prevention [2]. Finding a way to perform early diagnoses, risk assessments and ad-hoc therapies would be a great step beyond in orthopedic medicine. Nevertheless, due to its hierarchical organization, it is really hard and imprecise to define the real properties of bone as a whole, but we have to refer to its different scales [6]:

- *Whole-bone level (50 cm - 10 mm)*, where bone is considered in its totality as part of the skeletal system.
- *Meso-scale (10 mm - 500 μm)*, where we can distinguish between a compact cortical shell and a spongy, cellular-like inner trabecular structure.
- *Micro-scale (500 μm -1 μm)*, where bone cells (osteocytes) reside inside small voids called lacunae and continuously create and resorb bone tissue adapting to external stimuli [5].
- *Nano-scale (1 μm -10 nm)*, where bone is considered an organic-inorganic composite material made of water, collagen fibers and hydroxyapatite crystals.

Especially at the micro-scale, detailed mechanisms of bone fractures are not clarified yet, due to multiple factors such as the presence of lacunae, cement lines, toughening mechanisms and bone diseases. For these reasons, this work is focused on the characterization of the local mechanical properties of human femoral bone and on the damage mechanisms at the micro-scale, using a portable micro-compressive device and synchrotron-based imaging techniques.

2. Materials and Methods

2.1. Mechanichal tests

2.1.1 Sample preparation

Prior authorization from the Ethics Committee (ClinicalTrials.gov ID: NCT04787679), each femoral head removed from the patient is immediately partitioned by the surgeon, obtaining three different regions along the coronal plane

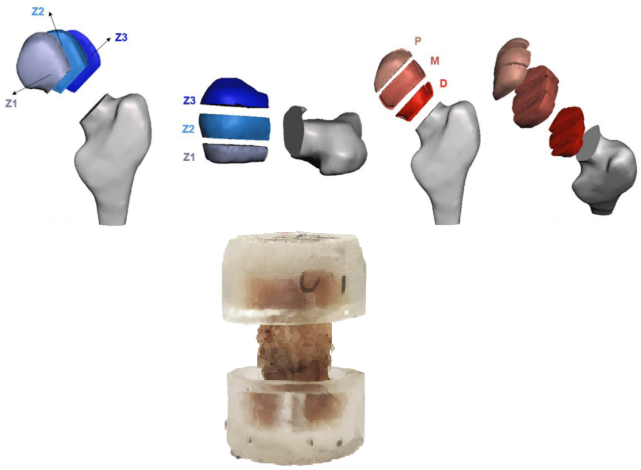

Figure 1: Partitioning of femoral head in zones (left), sub-zones (right), and the finished specimen (bottom) embedded into epoxy endcaps.

identified as Z1, Z2 and Z3. Each zone is then divided along the sagittal plane into three subzones: proximal (P), medial (M) and distal (D). The nine sub-regions are transferred to the *Histology Laboratory of Istituto Ortopedico Galeazzi* in Milan, where trabecular-bone, parallelepiped samples ($16mm^2$ in section and $14mm$ in height) are cut and mounted onto epoxy-resin endcaps (Figure 1).

2.1.2 Testing protocol

In this study, 8 female femoral heads (FH) have been tested to map their local mechanical properties: four of them come from osteoporotic patients (OP), and four from non-osteoporotic ones (non OP). In Table 1 are reported all the detailed information for each FH.

Table 1: Specific information for each FH: age, diagnosis, and additional clinical observations. The definition of osteoporosis reported is in accordance with the WHO guidelines.

FH	Age	Diagnosis	Observations
FH1	61	Non OP	Large bone spurs
FH2	90	OP	-
FH3	62	OP	Local arthritis
FH4	84	OP	Thick cortical shell
FH5	76	Non OP	Detected osteopenia
FH6	56	Non OP	Local displasic arthritis
FH7	59	Non OP	Detected osteopenia
FH8	77	OP	Local arthritis

Mechanical tests were performed with a micro-compressive device (MCD), designed at *Politecnico di Milano*. After preliminary calibration operations are completed, axial quasi-static micro-compressions are applied to the trabecular bone samples. Twelve micro-compressions per sample are performed, with a step amplitude of 0.1 mm and a displacement rate of 0.1 mm/s. Each compression step is followed by a 3 minutes-relaxation time where the displacement is kept constant. The output data are collected and analyzed with *Matlab*, which draws the stress-strain curves and extrapolates the values of Young's modulus, ultimate stress and strain, and yield strength.
All mechanical parameters undergo statistical analysis with the certified software *Minitab*, using Shapiro-Wilk normality test and then two sample T-test or ANOVA test to make comparisons. The confidence level is set to 95%.

2.2. Synchrotron-based analysis

µ-Computed Tomographies of samples were performed at the *ELETTRA Synchrotron* in Trieste, meanwhile they were undergoing micro-compressive testings in the MCD. For all samples an unloaded tomographic acquisition (STEP 0) is performed firstly, to visualize the initial situation. Then, other acquisitions are done (STEP 1, STEP 2, STEP 3). To cover the entire specimen height, 3 distinct acquisitions are needed. All scans are reconstructed and filtered with dedicated software and *Matlab* codes, to obtain the final images. Synchrotron radiation provides a resolution of 1.6 µm-per-pixel (below the lacunae level). From those images, using software *Fiji-ImageJ*, direct measurements of the main crack parameters were taken:

- **Crack propagation velocity**, measuring crack length along the height (Z direction) and section (XY plane) of the specimen, between two subsequent acquisition steps, and calculating the velocity as:

$$v_{crack} = \frac{\Delta a_{step(n)-step(n-1)}}{\Delta t_{step(n)-step(n-1)}} \qquad (1)$$

- **Crack Opening Displacement** (COD) along the crack path
- **Crack Tip Opening Displacement** (CTOD) ahead of each non-crossing crack. From this value, it was possible to calculate the relative value of fracture toughness with

the approximation:

$$CTOD = \frac{K_I^2}{E\sigma_{ys}} \qquad (2)$$

And compare it with the values calculated using the classical LEFM equation:

$$K_I = Y\sigma_n\sqrt{\pi a} \qquad (3)$$

Where Y is a coefficient (chosen 1.1), σ_n the acting nominal stress, and a the crack length. Two different approaches were taken into account for the selection of the material properties. The former consists of obtaining the values directly from the experimental stress-strain curve and considers the material as it was not porous, the latter accounts for bone porosity following *Gibson and Ashby "density power law model"* [1], assuming a linear relationship.

Considering the complexity of the localization of cracks, a FEM 3D model for the whole sample was implemented to localise the most stressed region. Firstly, all the single tomos are stitched together and downsized, to create an .STL file, where a hexahedral mesh is applied using *Altair Hypermesh*. In *Abaqus* a linear elastic simulation is performed, with the aim of reproducing the mechanical test. The specimen is fixed at the base with an encastre and on the top surface a displacement of 0.4 mm is applied, in order to simulate the first acquisition step. The material input for bone are: Young's modulus of 413 MPa, derived from the experimental test, and Poisson's ratio of 0,3.

3. Results

3.1. Local mechanical properties

The results for the statistical analysis of the Young's modulus for the 8 femoral head are reported in Figures 2, 3, 4.

3.2. Computational model

The finite element model finds that the most stressed region highlighted by the analysis corresponds to an actual broken trabecula visible in the tomographic images (Figure 5).

This result will be helpful in detecting the most critical region where cracks will develop first.

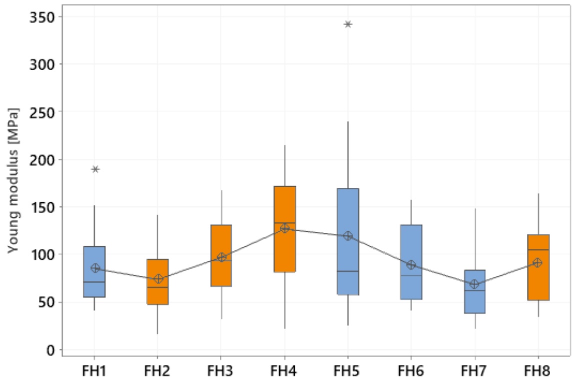

Figure 2: Values of Young's modulus for all the 8 FHs. In orange the OP, while in blue the non-OP ones.

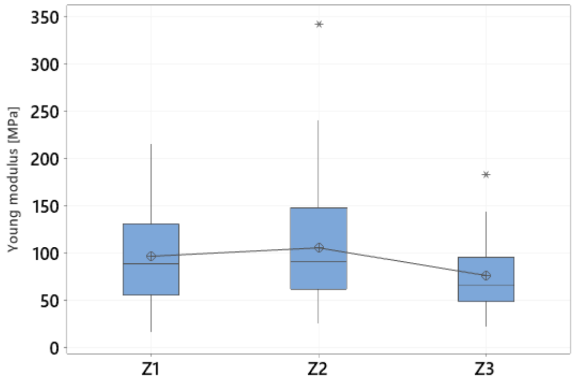

Figure 3: Values of Young's modulus divided by zone.

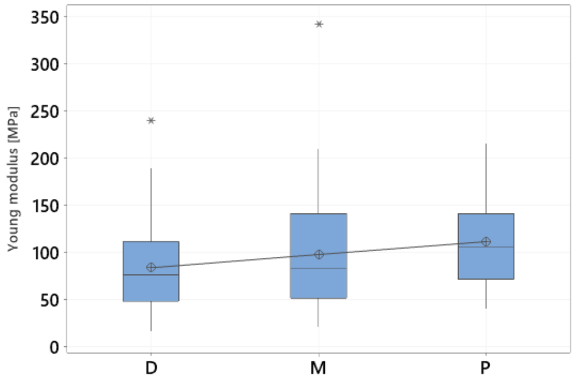

Figure 4: Values of Young's modulus divided by subzone.

3.3. Tomographic analysis

Regarding the investigation of the synchrotron-based tomographic images, four specimens had been fully reconstructed and analyzed, two os-

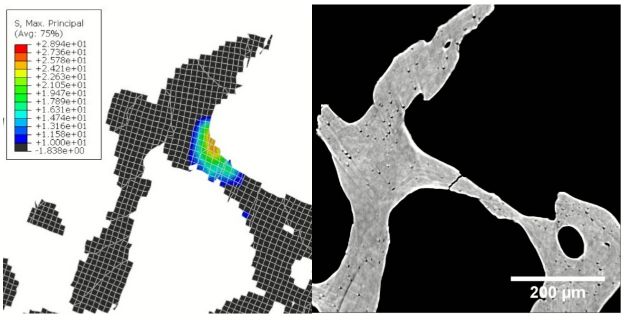

Figure 5: Most stressed region of the computational model (on the left), corresponding to a cracked trabecula (on the right) at STEP 1.

teoporotic, called FH2-S53 and FH4-S31, and two non-osteoporotic ones, called FH1-S7 and FH5-S33.

3.3.1 Crack propagation velocity

A number of 10 different cracks per sample have been considered in this study (Figures 6, 7). Depending on the actual presence of the crack in some acquisitions and the quality of the available images, some measures were taken between different tomographic steps.

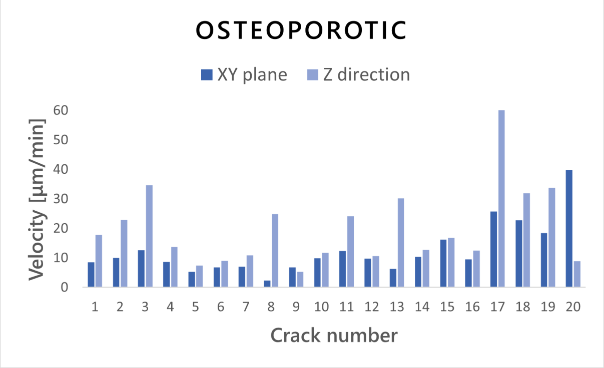

Figure 6: Propagation velocities of cracks in the osteoporotic samples.

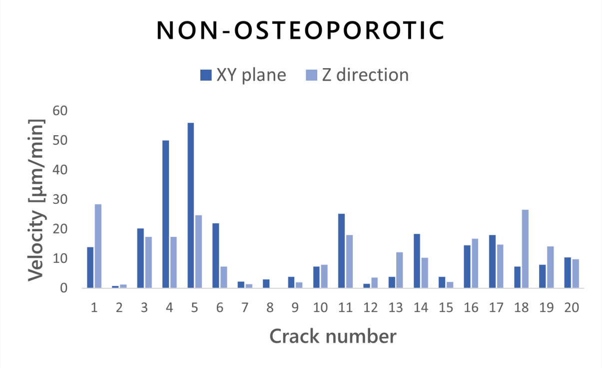

Figure 7: Propagation velocities of cracks in the non-osteoporotic samples.

3.3.2 Crack Tip Opening Displacement

Regarding CTOD, 5 different cracks for each specimen have been considered. The majority of cracks in the available slices cross completely the trabeculae, so it is difficult to spot non-crossing ones where to define a crack-tip. The presented values are an average between at least three measures taken on different heights, in order to have a more general and representative value.

Table 2: Average CTOD values for each sample.

Sample	CTOD average value [µm]
FH1-S7	3.9
FH2-S53	3.8
FH4-S31	4.3
FH5-S33	3.1

Furthermore, K_{CTOD} and K_I were calculated as explained in Section 2.2, and the average results are reported in Table 3 and Table 4; the values obtained considering the sample as non-porous are indicated with the superscript "sample", the ones obtained taking account of the porosity with the superscript "bone". The loading curve was missing for sample FH2-S53, so it is not considered in this analysis.

Table 3: Comparison between average K_{CTOD} and K_I for the different samples.

Sample	K_{CTOD}^{sample} [MPa$\sqrt{m}$]	K_I^{sample} [MPa$\sqrt{m}$]
FH1-S7	6.59×10^{-2}	2.05×10^{-1}
FH4-S31	4.25×10^{-2}	1.54×10^{-1}
FH5-S33	5.30×10^{-2}	3.80×10^{-1}

Table 4: Comparison between average K_{CTOD} and K_I for the different samples, accounting for porosity.

Sample	$\mathbf{K}_{CTOD}^{bone}$ [MPa$\sqrt{m}$]	$\mathbf{K}_{I}^{bone}$ [MPa$\sqrt{m}$]
FH1-S7	2.20×10^{-1}	6.84×10^{-1}
FH4-S31	2.13×10^{-1}	7.72×10^{-1}
FH5-S33	1.77×10^{-1}	1.26

4. Discussion

4.1. Mechanical properties comparisons

Since the inter-patients variability is very high, a normalized Young's modulus (E/Emax) was used, which is more representative of the real situation. In fact, normalizing the Young's modulus with respect to the maximum value detected in each femoral head, allows neglecting intrinsic variations linked to the donor age or femoral head morphology.

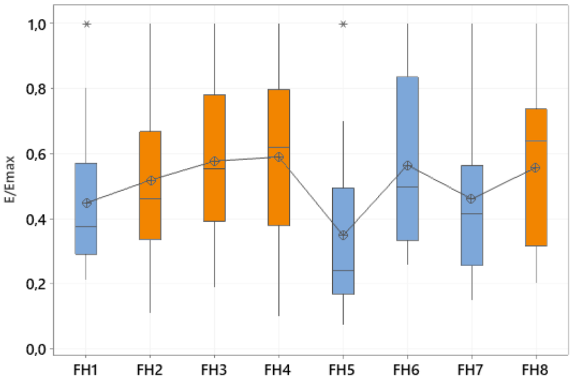

Figure 8: Statistical comparison for the normalized Young's modulus between all 8 FHs. In blue non-OP samples, in orange OP samples.

A great variability of the results can be noticed in Figure 8, even more pronounced for the osteoporotic samples. Some borderline cases could be detected, with FH3, FH4, FH6 and FH8 displaying higher normalized modulus values when compared with osteoporotic FH2 and even in comparison with the non-osteoporotic FH1, FH5 and FH7 cases. Indeed, FH3, FH6 and FH8 presented also local arthritic regions, while FH4 was affected by a thickening of the cortical region in contact with the acetabulum, while showing an overall osteoporotic condition. On the other hand, sample FH5 presents lower values when compared with the others, which may be caused by the fact that the sample was actually osteopenic. Also FH7 was diagnosed with osteopenia, in fact shows values closer to FH5 ones. These considerations are particularly interesting and highlight the capability of the MCD to capture local variations of the mechanical properties.

As expected, looking at Figures 3, 4 it is immediate to notice that Z2 zone and proximal sub-zone have the best mechanical response; in fact it reflects the actual transfer of loads from the acetabulum to the femur, which remains unchanged even in presence of pathologies.

4.2. Crack parameters comparisons

Examining the graphs presented in Section 3.3.1 about crack propagation velocity in different directions, it is possible to notice how the different conformation of the bone is influencing the way cracks propagate. The crack propagation velocities for non-OP samples do not display any specific trend, while for the OP ones the velocities along Z axis are visibly higher than the ones on the XY plane. This can be explained by the fact that OP bones, in general, present thin trabeculae and a lower BV/TV when compared to non-OP bones. Indeed, the thickness of the trabeculae in this work had an average value of 180 µm for the OP and 350 µm for the non-OP (up to 800 µm in the intersection points). The samples were extracted along the principal compressive direction, so the trabeculae tend to be naturally oriented in that direction; as a consequence, Z axis of the samples becomes a preferential direction for crack propagation, especially in comparison with the XY plane of the OP samples.

For what concerns CTOD, the values measured are consistent for all the samples, as shown in Table 2, with values around 3-4 µm. Although, it is needed to take into account that the measures are performed at the limiting resolution for the images and, as a consequence, an intrinsic error of ±1.6 µm has to be considered.

Moreover, it is interesting to compare the calculated value of K_{CTOD} to the K_I: as displayed in Table 3 and Table 4, it is possible to notice that the difference in values between them is around one order of magnitude, maintained for all the samples. The obtained results differ from the ones reported in literature [3] of another order of magnitude. On the other hand, accounting for porosity, the results are very similar, and closer to literature's values. Indeed, *Taylor et al.* [4] reported values of 1-5 MPa$\sqrt{m}$, which tend to lower in elder people. Moreover, all our samples come from patients who have undergone hip surgery after fracture and bone disease diagnoses, so are not in normal physiological conditions. Another aspect to be considered is that the values from the literature refer to cortical human bone, while there is a lack of data regarding trabecular bone due to its complexity.

As a final consideration, it is important to remark that the methodology for the measurement of crack parameters performed in this work is tailored on the small dimension of the samples, and may differ from the one used in other papers [3]. Moreover, the images available for this work are at an extremely high resolution (1.6 µm per pixel), making it is possible to see very fine cracks, leading to smaller CTOD and, consequently, an average lower value of K$_{CTOD}$.

5. Conclusion

It is possible to conclude saying that:

- it was possible to find interesting trends of the properties in the different zones and sub-zones, with the best results in terms of mechanical properties for Z2 zone and P sub-zone, as expected;
- the full-specimen FEM model developed is capable of providing, with good precision, which are the most critical zones where the first fractures will form. This will help lightening the tomographic analysis procedure;
- cracks in OP patients mainly develop along the vertical direction of the sample, because of the low thickness of the trabeculae in the slicing plane;
- the calculated fracture toughness has lower values than the ones reported in literature, probably because of the different methodology used, based on direct measurement of the parameters and tailored for the small samples we have, and the bone quality of our donors.

References

[1] IJ Gibson and Michael Farries Ashby. The mechanics of three-dimensional cellular materials. *Proceedings of the royal society of London. A. Mathematical and physical sciences*, 382(1782):43–59, 1982.

[2] Emma Hernlund, A Svedbom, M Ivergård, J Compston, Cyrus Cooper, J Stenmark, Eugene V McCloskey, BKJA Jönsson, and John A Kanis. Osteoporosis in the european union: medical management, epidemiology and economic burden. *Archives of osteoporosis*, 8(1):1–115, 2013.

[3] NK Sharma, DK Sehgal, and RK Pandey. Orientation dependence of elastic-plastic fracture toughness and micro-fracture mechanism in cortical bone. *Engineering letters*, 19(4), 2011.

[4] David Taylor, Jan G Hazenberg, and T Clive Lee. Living with cracks: damage and repair in human bone. *Nature materials*, 6(4):263–268, 2007.

[5] Julius Wolff. Das gesetz der transformation der knochen. *DMW-Deutsche Medizinische Wochenschrift*, 19(47):1222–1224, 1893.

[6] Elizabeth A Zimmermann, Björn Busse, and Robert O Ritchie. The fracture mechanics of human bone: influence of disease and treatment. *BoneKEy reports*, 4, 2015.

POLITECNICO DI MILANO

SCHOOL OF INDUSTRIAL AND INFORMATION ENGINEERING

MASTER OF SCIENCE THESIS IN

MATERIALS ENGINEERING AND NANOTECHNOLOGY

Micro-compressive testing and synchrotron-based damage analysis of human trabecular bone

Advisor:

Prof. **Vergani Laura Maria**

Co-advisor:

PhD Candidate **Buccino Federica**

Authors:

Renolfi Federico

Student ID: 942354

Zilioli Sara

Student ID: 944700

ACADEMIC YEAR 2020-2021

Ringraziamenti

Con questo progetto di tesi si conclude un importante capitolo della nostra vita; è quindi doveroso ringraziare le persone che ci hanno accompagnato durante questo percorso.

Ringraziamo la professoressa Vergani per l'opportunità di poter studiare ed approfondire un argomento così interessante ed interdisciplinare e Federica, per averci seguito e supportato in tutte le fasi del lavoro sempre col sorriso.

Ringraziamo tutte le persone con cui siamo venuti in contatto per la realizzazione di questo progetto di tesi. In particolar modo Filippo e Nicola per averci introdotto al lavoro nelle fasi iniziali, Cristina e Gabriele per aver condiviso con noi parte di questo progetto, ed il team di ELETTRA per averci aiutato con professionalità e simpatia durante gli esperimenti a Trieste.

Infine un ringraziamento speciale alle nostre famiglie e amici tutti, per averci sostenuto in tutti questi anni.

Sara e Federico

Contents

Abstract

Bone structure complexity and the strong inter-dependence between mechanical properties and its meso and micro-architecture are particularly visible in the human femur, especially in presence of diseases such as osteoporosis and osteoarthritis. The present work is focused on the micro-scale, where a detailed knowledge of damage mechanisms is missing, being influenced by the presence of lacunae, cement lines and toughening mechanisms. For this purpose, a portable micro-compressive device and synchrotron imaging has been used to map bone local mechanical properties, evaluate cracks propagation mechanisms, and measure fracture mechanics parameters that could characterize damage patterns' differences. Analyzing four healthy and four osteoporotic femoral heads, intra-patients variability shows increased resistance to compression in the proximal sub-region, close to the acetabulum, where loads are transmitted from the hip to the femur. Furthermore, it has been measured values of crack tip opening displacement (CTOD) around 3-4 μm, K of the order of 10^{-2}-10^{-1} MPa$\sqrt{m}$ and crack propagation velocities around 10-20 μm/min, with a preferential propagation along Z-direction in osteoporotic samples.

Keywords: osteoporosis, human trabecular bone, femoral head, micro-compression, SRμCT, bone damage.

Sommario

La complessità della struttura ossea e la forte interdipendenza fra proprietà meccaniche e la sua meso e micro-architettura sono particolarmente visibili nel femore umano, specialmente in presenza di malattie quali osteoporosi ed osteoartrite. Il presente lavoro si concentra sulla microscala, per la quale non si ha ancora una conoscenza dettagliata dei meccanismi di danneggiamento, poiché influenzata dalla presenza di lacune, linee cementizie e dal verificarsi di fenomeni tenacizzanti. A tal proposito, si è sfruttato un set up di prova coniugato con l'imaging al sincrotrone per mappare le proprietà locali dell'osso, osservarne l'avanzamento delle cricche e misurare alcuni parametri di meccanica della frattura che possano caratterizzarne il comportamento a frattura. Analizzando quattro teste femorali sane e quattro osteoporotiche, la variabilità intra-paziente mostra maggiore resistenza a compressione nelle sub-zone prossimali, vicine all'acetabolo, dove i carichi vengono trasmessi dal bacino al femore. Inoltre sono stati misurati per le cricche valori di crack tip opening displacement (CTOD) attorno ai 3-4 μm, K dell'ordine di 10^{-2}-10^{-1} MPa$\sqrt{m}$ e velocità di propagazione sui 10-20 μm/min, con direzione preferenziale di propagazione lungo la direzione Z nei campioni osteoporotici.

Parole chiave: osteoporosi, osso trabecolare umano, micro-compressione, testa femorale, SRμCT, danneggiamento osseo.

List of Figures

List of Tables

Chapter 1

State of the Art

1.1 Introduction

The study of bone multi-scale structure and its pathologies have an increasing interest in medical research, due to their impact on public health costs and everyday life. Moreover, due to its complex architecture, its damage mechanisms are not clear yet. Femur, especially, holds a central role in many studies, since its fracture brings to a high number of surgeries and hospitalizations every year and has a delicate mechanobiological equilibrium. Thus, finding a way to perform early diagnoses, risk assessments and ad-hoc therapies would be a great step beyond in orthopedic medicine. In this context is placed our thesis work, concerning micro-compressive testing and synchrotron-based damage analysis of both healthy and osteoporotic trabecular femoral bone.

1.2 Complex hierarchical structure of bones

Bone is a complex organic-inorganic composite material organized in a hierarchical structure along different scales as shown in Figure 1.1. It is a multi-scale mineralized living connective tissue that makes up the skeleton and provides multiple mechanical and biological functions for the entire body. Beyond its structural support to the body, allowing movements and locomotion, it protects the vital internal organs (heart, lungs, brain) and enables sound propagation and transduction in the ears; it also guarantees the maintenance of mineral homeostasis, being a reservoir of calcium and phosphorus. Moreover, it provides a proper environment for the production of blood cells (hematopoiesis) within the marrow of the cancellous bone [19, 60]. Due to its complexity, it is really hard and imprecise to define the real properties of bone as a whole, but we have to refer to its different components:

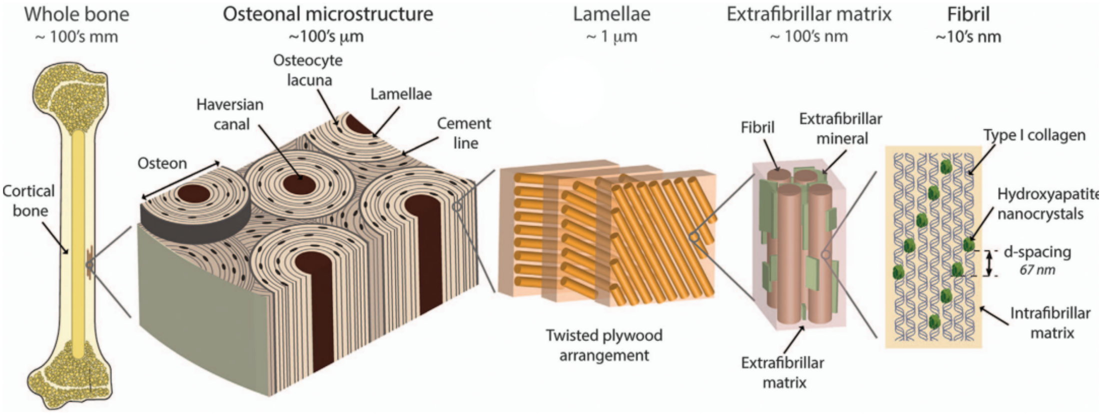

Figure 1.1: Representation of the hierarchical structure of a human bone [86].

1. *Macro-scale or whole-bone level (50 cm - 10 mm)*: this is the highest level, where the bone is considered in its totality as part of the skeletal system. The most recognized medical classification distinguishes between long bones (e.g. femur, radius), short bones (e.g. carpal, patellae), flat bones (e.g. skull, ribs) and irregular bones (e.g. vertebrae, coccyx). The shape is strictly correlated to its specific function and adaption to the local loading conditions.

2. *Meso-scale (10 mm - 500 μm)*: at this level it is possible to distinguish between two microstructures: cortical and trabecular, which are detectable through his-

tological evaluation [59]. The adult human skeleton is composed of 80% cortical bone and 20% trabecular bone overall [24], but the relative ratio varies between different bones and skeletal sites.

Cortical bone is dense and compact and surrounds the marrow space. Its porosity is <5% [19] (the minimum to accommodate cells and vascular network) and has typically less metabolic activity than trabecular bone. In cortical bone the mechanical properties are influenced greatly by the porosity, the mineralization level and the organization of the solid matrix [59]. In particular, bone strength increases with cortical shell thickness and diameter, while decreases with porosity [22].

Trabecular or cancellous (spongy) bone is a spongy, honeycomb-like structure composed of a network of interconnected small rods and plates (trabeculae). Those structs are some 100 μm thick and separated by 1mm-wide holes [60]. Within this network we have the bone marrow compartments, where new blood cells are created. Cancellous bone has a higher metabolic activity than cortical, which means that it is remodeled more often, therefore is younger on average than cortical one; it is important to remark that bone structure is not constant in time, but changes due to the incessant work of the bone cells (osteocytes, osteoclasts and osteoblasts). They remodel cyclically the bone by reabsorbing and producing tissue after biomechanical inputs.

3. *Micro-scale (500 μm -1 μm)*: at this scale both cortical and trabecular bone are composed of 3-7 μm [63] thick sheet-like structures, called lamellae, organised in concentric or rod-like structures. Here reside bone tissue cells, osteocytes, located in microscopic pores called lacunae.

4. *Nano-scale (1 μm -10 nm)*: at its smallest scale, bone is an organic-inorganic composite material. The inorganic mineral part ranges between 50 to 70%,

and is mainly composed of hydroxyapatite (HA) [$Ca_{10}(PO_4)_6(OH)_2$] and small quantities of carbonates, magnesium and acid phosphates. The organic part consists of 20 to 40% collagen matrix, 5-10% water and a few percent of lipids [19].

1.3 Human femur

In femur this hierarchical complexity is particularly evident, and, among all human bones, it holds great clinical interest due to the high incidence of fractures caused by incidents or diseases such as osteoporosis, osteoarthritis and rheumatoid arthritis. It is estimated that femoral fractures have an incidence rate of 5.4 per 1000 persons per year, compared with 4.9 for wrist fractures and 1.9 for upper humerus [64]. Especially in the elder population, hip fracture still represents one of the most important causes of morbidity and mortality. Apart from the direct impact on patient's social life, the economic burden and costs due to hospitalization, treatments and rehabilitation are high, and are continuously rising along with the average age of the population: it is estimated to increase from $57 billion in 2018 to $95 billion by 2040 [7], while the annual number of cases will increase to 6.26 million by 2050 [61]. From these projections, it is immediate to understand the importance of studying in depth femur's properties and meso-architecture, in order to prevent such diseases and formulate more effective treatments.

1.3.1 Femur meso-architecture

The femur, or thigh bone, is the longest and strongest bone of the human body. It is formed by a central hollow shaft called diaphysis, an upper and a lower end called epiphyses. The upper end of the femur includes a rounded femoral head, which articulates with acetabulum to form a hip joint, the neck, which is a 3cm-long concave

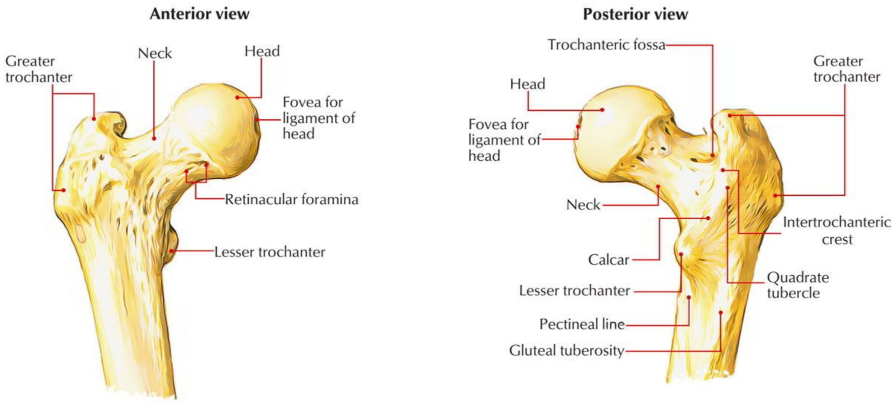

Figure 1.2: Human femur anatomy.

connection between head and shaft, and two prominences called greater and lesser trochanter (Figure 1.2). The shaft is almost cylindrical, with a cortical shell and a spongy trabecular core, wide at the extremities and narrower in the middle. Its composition varies depending on the site: particularly, the cortical-to-trabecular ratio is 50:50 for the femoral head, while it rises to 95:5 along the radial diaphysis [19], so also its strength will be dependent on the site tested.

Another important aspect that must be considered is that bone structure is not constant in time, but changes due to the incessant work of the bone cells: osteocytes, osteoclasts and osteoblasts, that remodel cyclically the bone by reabsorbing and producing tissue inside the osteons after biomechanical inputs. This phenomenon is known since the 19th century by Julius Wolff's work [83], who provided a law for cancellous bone adaptation to external mechanical loadings that has been widely recognised and used in modern computational modelling works [74, 28]. The microarchitecture of the trabecular network has a substantial impact on bone strength. In particular connectivity and orientation play a fundamental role: the higher the number of bridges between distinct trabeculae, the higher is the strength [39], while the more those shafts are aligned with the acting load, the more the bone results

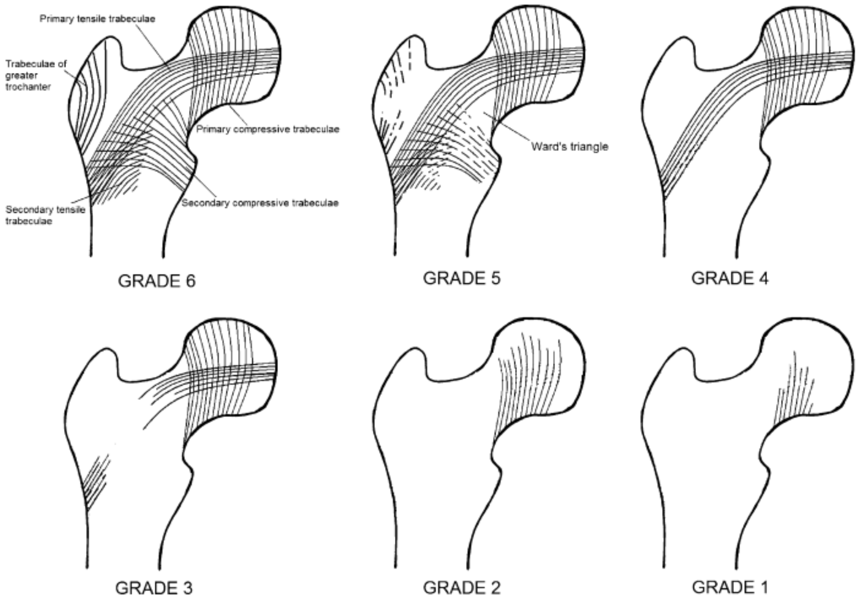

Figure 1.3: Singh index from Grade 6 (normal healthy bone showing trabecular tensile and compressive patterns) to Grade 1 (severe osteoporotic bone with a dramatic reduction in cancellous bone) [5]. The orientation of trabeculae reflects the force lines of external loads acting on the femur.

stiff [31]. Another important parameter is also trabecular thickness in determining strength. Trabecular failure occurs by buckling and bending, so the strength of the trabecular strut is proportional to the square of its radius [22]. Following Wolff's approach, in 1970 *Singh Et.al.* [67] studied and proposed a simple mean to account for femoral bone quality based on a trabecular pattern that can be easily visualized with x-ray radiography [5]: the Singh index. As shown clearly in Figure 1.3, proximal femoral trabeculae are aligned according to different directions, that follow the force lines of the principal applied external loadings. In the case of bone diseases, such as osteoporosis and osteoarthritis, those patterns disappear, compromising the mechanical performance.

1.3.2 Human femur mechanical properties

Due to its heterogeneous structure, also mechanical properties are strongly site-dependent and vary depending on the zone considered. Several works have been published throughout the years, for sake of simplicity, many of them were conducted on animal samples, particularly on rats [43, 1], ovine [16, 84] and bovine [84, 33]. On the other hand, many tests have been conducted on human samples too, considering different bones: the most studied are vertebrae, tibia, radius, iliac and femur [84, 25]. For all of them, different testing procedures and methods are available, and each research group tends to use its own, but generally the most used are:

- Bending (3 or 4-point-bending) [7, 84, 27].
- Tension [16, 33, 84, 25], both macro and micro-mechanical.
- Ultrasound and resonance frequency [84, 15].
- Compression, as exposed in detail in the following.

The most used and efficient testing method is compressive loading, due to the simplicity of its set-up and the fact that it mimics the natural external impacts and loads the femur is daily subjected to [21, 41, 2, 11]. Moreover, a compressive load is often the main cause of failures and subsequent hospitalization.

Reviewing the principal and most representative publications found in literature, below (Table 1.1) is reported a sum of the principal results concerning *human femur under external compressive load*.

All the reported compressive tests are quasi-static, conduced with displacement-rate control ranging from 0.065 to 0.33 mm/s, apart from the micro-compressive test on the single trabecula, where a loading ramp of 57 mN/s was applied. Applying a known displacement, the output force originated as a reaction by the samples is recorded with a load cell. The resulting stress (σ) is calculated dividing the force by the cross section of the specimen, while strain (ε) is calculated dividing the applied displacement by the original reference length, according to the well-known formulas from solid mechanics:

$$\sigma = \frac{F}{S} \quad \varepsilon = \frac{\Delta l}{l_0} \tag{1.1}$$

To define precisely the strain, usually a strain-gauge is applied onto the bone specimen, or it is calculated manually monitoring the sample motion with a high-frequency camera or a video-extensometer (not to damage the bone surface). Finally, Young's modulus (E) is calculated as the slope of the stress-strain curve in the linear elastic region.

From Table 1.1 it is possible to see how the Young's modulus (above all) covers a wide range of values. This shows that the mechanical property of the bone is not only scale-dependent but is related also to multiple factors such as the donor itself, the site of extraction of the specimen and its geometry (shape, size and aspect ratio) and the experimental operative conditions (wet or dry bone, displacement rate, presence of endcaps at the edges of the sample). Two exceptions to highlight are the micro-compressive tests, in fact the values of modulus are of units of GPa, while for mesoscale tests the values barely overcame 500 MPa: this clearly highlights the strong dependence of mechanical parameters on the scale and on the hierarchical build-up.

Table 1.1: Comparisons between different compressive tests on healty human femurs. For each author are reported femural site, geometry of the extracted specimen and the values of Young's modulus (E), yielding stress (σ_y), ultimate strain (ε_f) and ultimate stress (σ_u).

Author	**Femural site**	**Specimen geometry**	σ_y **[MPa]**	**E [MPa]**	ε_f **%**	σ_u **[MPa]**
Aleixo et al., 2013 [2]	Femural head, trabecular bone, principal compressive	Cylinder $\varnothing$=15mm, h=30mm	4.35-10.53	212.4-761.0	30 (chosen)	7.31-10.54
Sugita et al., 1999 [69]	Femoral head primary compressive group	Cubic l=6.5mm		150-450		1-16
Hambli, 2013 [34]	Proximal femur and greater trochanter trabecular bone	Cylinder $\varnothing$=7.04mm, h=5.5-10mm			2.2-2.85	5-34
Bini et al., 2002 [6]	Femur single trabecula	single trabecula		1410-1890		
Hong et al., 2007 [84]	Femoral head, trabecular bone	Cubic l=0.3mm		2540-3470		
Fleps et al.,2020 (review) [25]	Femur, mainly trabecular bone	Cylinders and cubes, l=several mm				2-35
Spatafora, 2014 [68]	Femural head, trabecular bone	Cylinder $\varnothing$=11mm, h=9-16mm	1-6	100-280	3-8	1.5-6.5
Li et al.,1997 [45]	Femoral neck, trebecular bone	Cylinder $\varnothing$=9mm, 7.8±2.0mm in height	1.05-1.5	130-175		

1.3.3 Bone diseases and mechanical properties

Mechanical properties are deeply influenced by the presence of bone diseases, particularly osteoporosis (OP) and osteoarthritis (OA), which have a great impact on people's lives and on the sanitary system. In the EU, a report estimated that in 2010, 6.6% of men and 22.1% of women aged over 50 years had osteoporosis and that there were 3.5 million fragility fractures. The annual direct costs attributable to fracture treatment in the EU equate to approximately €24 billion, rising to €37 billion per year accounting for the indirect costs of care and prevention [36]. On the other hand, OA of the hip affects 5% of adults >65 years in North America and Europe [49]. In Italy are estimated 4 million cases, and it is the primary cause for invalidity [26].

Osteoporosis

Osteoporosis (Figure 1.4), is defined by the World Health Organization (WHO) as a "progressive systemic skeletal disease characterised by low bone mass and micro-architectural deterioration of bone tissue, with a consequent increase in bone fragility and susceptibility to fracture" [47]. It is the most common bone disease in elderly people, often leading to femoral neck fracture and subsequent surgery.

Osteoporosis is the major cause of fracture in individuals over the age of 50 years. Fragility fractures become more common with age and are significantly more common in women than man, as shown in Figure 1.5, with a risk of 50% for women and 20% for men in Western populations [79].

Being characterized by alteration of internal bone composition, it often shows its symptoms only when bone fracture occurs, becoming difficult to diagnose in advance. Bone mass and architecture physiologically grow and change during childhood and adolescence, reaching their peak before the third decade of life [81] and then progressively decays with aging (Figure 1.6).

The current WHO operational diagnosis of osteoporosis is based on a DXA (Dual-

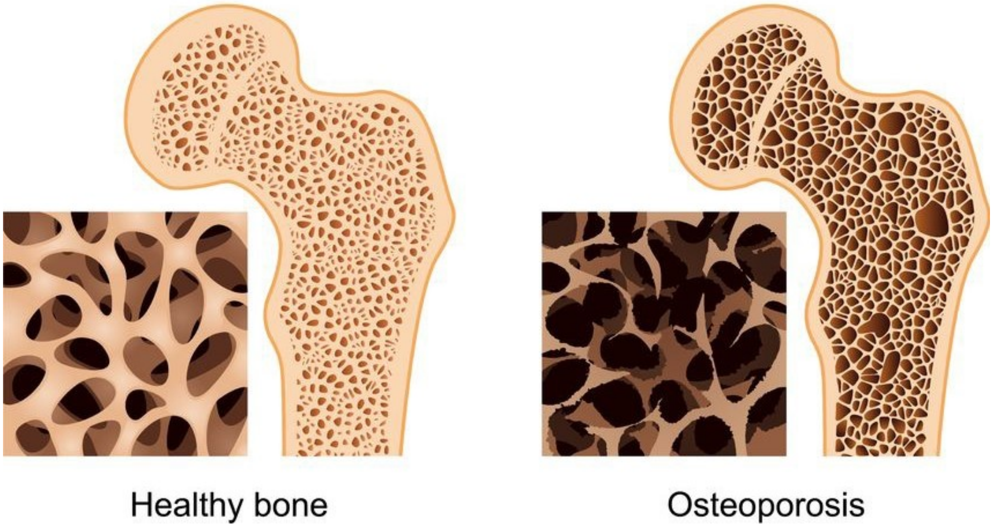

Figure 1.4: Comparative illustration between healthy (left) and osteoporotic (right) femural bone, with a detailed view of the deteriorated cancellous tissue.

Energy X-ray Absorptiometry) measurement of the Bone Mineral Density (BMD), following the clear link between lower BMD and increase of fracture risk. This densitometry test provides as output the T-score parameter: values above -1 are considered as normal, between -1.1 and -2.4 are classified as osteopenic (low bone mass), while values below -2.5 are osteoporotic. However, this correspondence is not completely accurate, and BMD can be considered more as a risk factor than as a disease in itself [47].

Osteoarthritis

Arthrosis or osteoarthritis is, together with osteoporosis, the most common chronic degenerative disorder affecting one or several joints. Formerly it was classified between primary and secondary, depending on the prevalence of the disease, but nowadays it is considered more as a group of distinct, heterogeneous and overlapping joint disorders with similar clinical and pathological outcomes [26, 49]. This disease involves the whole joint, including alterations both in the cartilage and in the underlying

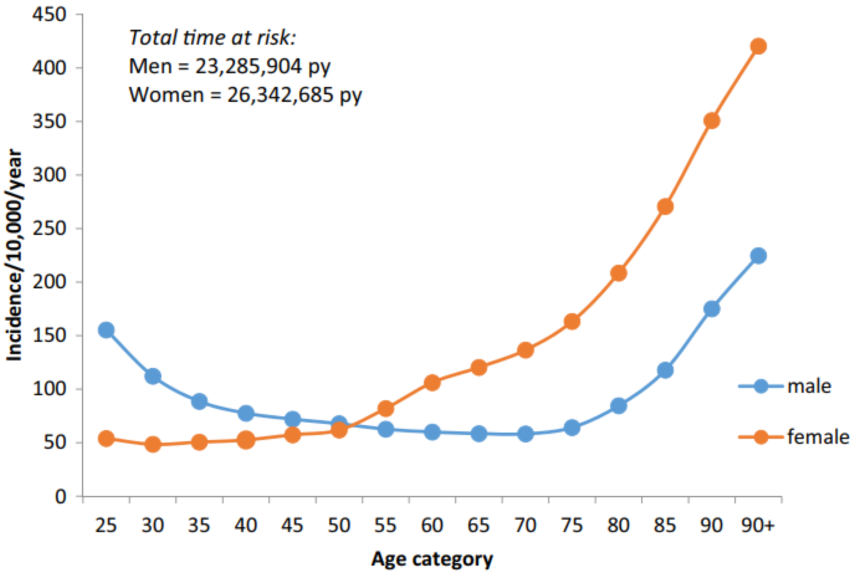

Figure 1.5: Incidence of any osteoporotic-related fracture by age and sex in the UK [78].

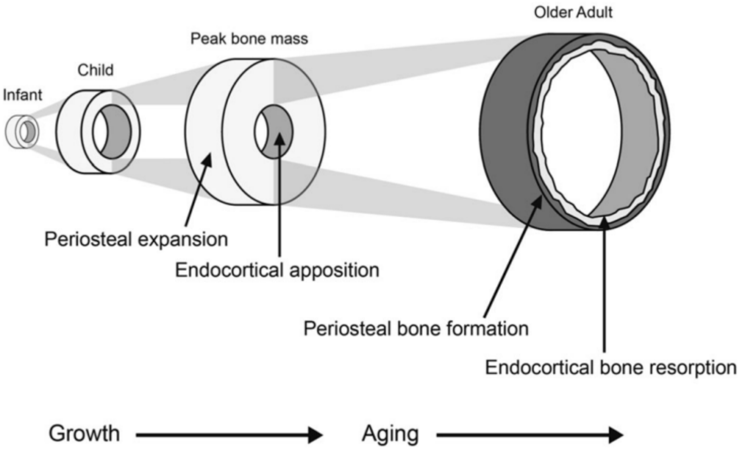

Figure 1.6: Changes in bone structure and mass throughout the lifespan. Particularly, bone gains mass during the first 30 years, while looses it afterwards [81].

subchondral bone, but also in the capsule and synovial membrane. The first symptoms are joint pain during motion, changes in size and morphology of the bone visualized with radiography and alteration of mechanical properties, leading to a possible joint failure (Figure 1.7).

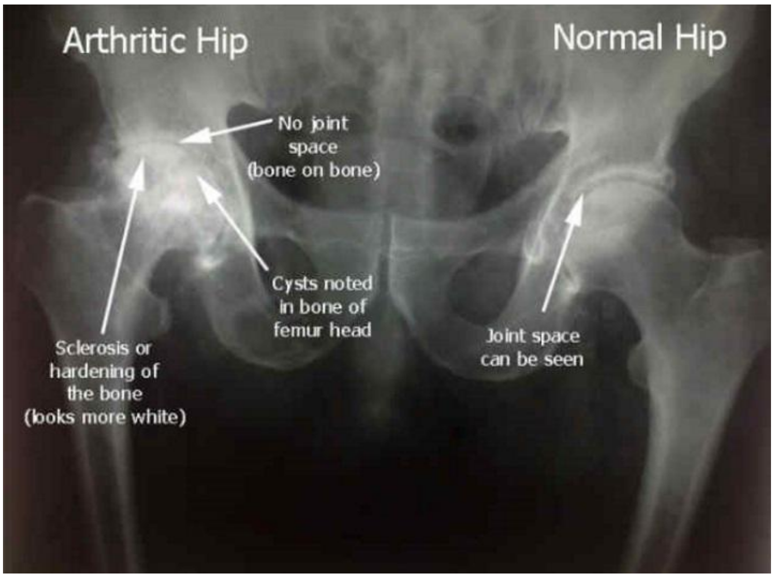

Figure 1.7: Radiography comparing osteoarthritic hip joint (left) with a normal one (right), highlighting the consumption of cartilage, presence of bone cysts and thickening of the subchondral femoral head. (Source: Orthopaedic Associates)

Regarding the subchondral bone, OA is associated with an increase in volume, thickness and shape of the cortical shell, but also alterations in the trabecular bone architecture, in bone mass and mineralization, and formation of cysts and marrow lesions. The main classification distinguishes between four clinical pictures, depending on the interested site and disease advancement. The one that involves the hip joint is the *rapidly destructive coxarthrosis*. As the name suggests, it rapidly brings to a painful and accentuated symptomatology, with great damage in the joint, but without showing bone enlargement (atrophic OA).

Structural OA is more frequent among women than men at any given age >50 years, with the sex difference most pronounced for hand and especially knee OA [56].

Prevalence rates rise steeply with age in both sexes. Knee OA variant is found to be most frequent among older women (>65 years of age) [49].

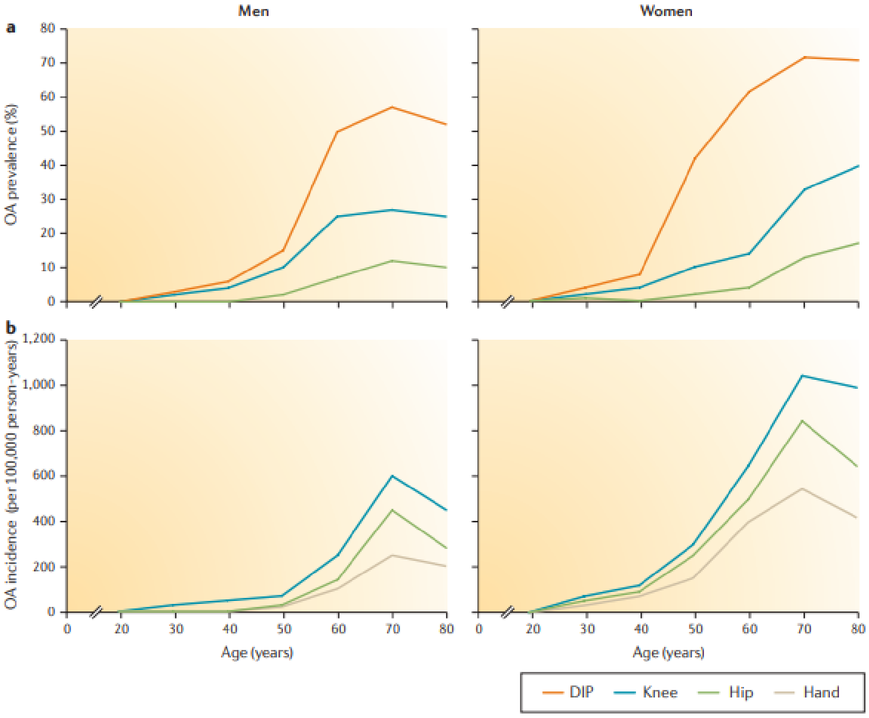

Figure 1.8: Prevalence and incidence of OA. a) Age-specific and sex-specific prevalence rates for structural osteoarthritis (OA) that affects the distal-interphalangeal (DIP), knee and hip joints in a large Dutch population. b) Incidence of symptomatic OA of the hand, knee and hip [55].

Correlation and role of OP-OA on mechanical properties

Since OA and OP are the two most common skeletal diseases in the aged population, frequently in literature are reported comparisons between them, both from the point of view of bone composition and mechanical properties. Nevertheless, their relationship is still controversial: while OP can occur in bone inflammatory processes, it seems that OA and OP are not likely to occur together, but show an inverse correlation [23, 62, 20]. In fact, OA shows opposite characteristics when compared to OP in terms of bone alterations, microstructure and mechanical response:

- Cortical and trabecular thickness and volume are significantly higher in case of osteoarthritis [62, 20], resulting in higher stiffness and strength of the subchondral region. Particularly, studies have found that patients with cox-OA have increased cancellous wall thickness (+21%), associated with a reduction in the number of osteocytes (-21%) and lacunar densities (-23%) [23], while an increase of 72% in the trabecular volume, compared to a loss of about 20% in the OP group with respect to normal bone. OA patients can show an overall increase up to 30% [14] in total bone volume.

- Osteoarthritic patients have a higher bone mineral density (correlated with bone strength) and show lower fragility fracture risk than patients with OP. General BMD is found to increase of up to 15% [14] in OA, while in specific sites such as femoral neck it can increase of 3.5% [23]. Also apparent density, which is bone mass divided by total sample volume (bone and porosity combined), is higher in OA because of the increased number of trabeculae and reduced separation between trabeculae. However, material density, which is bone mass divided by bone volume, is significantly less in OA subjects. This can be explained by two factors: firstly, the great increase of bone volume which is at the denominator of the ratio. Secondly, as many researchers highlighted, osteoarthritis brings altered amounts of minerals and water. Overall is shown a 5-7% reduction in minearal in the tissue and a concomitant increase in water, which replaces mineral on a 1:1 ratio in bone [23]. Focusing on trabecular bone, the mineral content can be 5% lower and the water content 20% higher than normal, while the mineral content of the OA calcar bone was found to be nearly 4% greater than that of the OP bone and the water content 8% less. So, OA trabecular bone shows an increased apparent density but a reduced material density, whereas the calcar bone shows a small, but significant, increase in mineral content compared with the OP group [45].

- OA cases with hip fracture were mostly due to trochanteric failure, and not of femoral neck (common of OP cases). This can be caused by fatigue microcracks originating in the subchondral bone and propagating in the cancellous; due to higher stiffness in subchondral region, eventual bone deformation is not dissipated efficiently, accumulating in a dangerous way [23].

Nevertheless, their exact relationship is still controversial, and other reports supported their coexistence [72]; in fact, it is not uncommon to find in globally osteoporotic femur a local thickening and densification of cortical shell, compatible with arthritic disease. Particularly, it must be noted that, while OA involves joints mainly near the cartilage level, OP regards the entire bone system: so, densitometric measurements of the hip with OA may be elevated due to subchondral osteosclerosis and may not reflect the status of the contralateral hip or the general skeleton. Moreover, it is known that inflammatory processes are a risk factor for both diseases [70], but while OA is painful and debilitating, OP may be silent until the subject has a fragility fracture. Several studies report that between 20% to 29% of women and men with OA have occult OP, which increases their risk of fracture [30].

Regarding their role on the mechanical properties of bone, in Table 1.2 are presented four studies, comparing the mechanical properties of two groups: osteoporotic and osteoarthritic ones. The specimens used in each paper are equal for the two groups in terms of size and geometry; also testing conditions (quasi-static compression, displacement control) are the same within each study.

Looking at this table, it is immediate to notice that the values of stiffness and strength are higher in the case of OA than OP, confirming the predicted trend, and showing once more how the mechanical properties are influenced both by trabeculae and cortical bone, but also on bone composition. The only study that does not show significant differences is the one by Catarina Vale et al., where it is supposed that the different fracture incidence is due to different fracture mechanisms, rather than material properties. The wide range of values obtained for the single property is due to multiple factors, such as age of the patients, intrinsic factors, bone characteristics (BMD, BV/TV) and, above all, testing operating conditions and sample geometry, as specified in Table 1.2.

Table 1.2: Different studies showing comparisons between osteoarthritic and osteoporotic femurs, reporting for each author: specimen geometry, values of Young's modulus (E), ultimate stress (σ_u), yielding stress (σ_y).

Author	**Specimen geometry**	**Osteoarthritic (OA)**			**Osteoporotic (OP)**		
		E [MPa]	σ_u **[MPa]**	σ_y **[MPa]**	**E [MPa]**	σ_u **[MPa]**	σ_y **[MPa]**
Chun Li et al. [46]	Parallelepiped, 15x15x10mm	95 ± 40	6 ± 2		55 ± 40	3.5 ± 1.5	
Li et al.[45]	Cylinder ⌀=9mm, h=7,8±2.0mm	310 ± 40		3.8 ± 0.8	75 ± 30		0.8 ± 0.15
Catarina Vale et al. [77]	Cylinder ⌀=15mm, h=30mm	443.28 ± 154.29	9.05 ± 4.23		502.45 ± 224.35	10.72 ± 4.67	
Sun et al. [70]	Cubic, 1cm in length	829 ± 215		17.2 ± 4.2	363 ± 154		5.7 ± 2.3

1.4 Role of the micro-scale

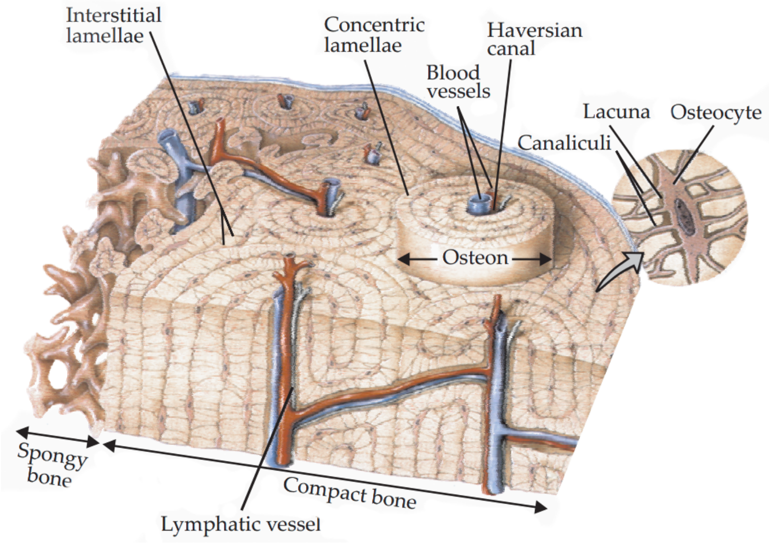

Figure 1.9: Representation of cortical bone at the micro-scale [60].

The hierarchical complexity is reflected also at the micro-scale (500 μm - 1 μm). In cortical bone (Figure 1.9), lamellae are packed in cylindrical, concentric structures called osteons or Haversian systems with diameter of approximately 200-300 μm [63] and several millimeters in length. On the outer surface of each osteon there is a thin layer of mineralized cement-like material called cement lines. Osteons run preferentially following the bone's long axis, so are more aligned to the external main loads. At this level is also possible to find *lacunae*, microscopic pores that host bone cells (osteocytes) and are interconnected through a network of tiny channels called canaliculi of about 100 nm in diameter [63]. In trabecular bone, lamellae do not form cylindrical Haversian systems, but are packed into rods and struts giving the single trabecula. Each trabecular packet has a semilunar shape and an average thickness of 50-400 μm [19]. Neither osteons nor canals are found in trabecular bone, nevertheless there are lacunae hosting cells and canaliculi. Therefore, trabecular bone is characterized by two levels of porosity: one given by the cancellous spongy structure itself, and a lower one represented by the lacunar network. This feature makes the study of bone architecture even more articulated [10].

A deep comprehension of the micro-scale organization, the lacunar network distribution and interaction with an eventual fracture, plays a fundamental role also in the development of specific treatments for bone disease. In fact, pharmacological treatments act at this scale on the metabolic activity of the osteocytes residing inside lacunae. Anti-resorptive agents, including estrogen, bisphosphonates, and selective estrogen receptor modulators (SERMs), are the major drugs of choice for osteoporosis [17], inhibiting excessive bone resorption. Also anabolic agents (parathyroid hormone and related peptide analogs), that promote new-bone creation, have major roles in current treatment regimens [75], together with the nutritional support of calcium and vitamin D.

1.5 Fracture mechanisms

In the last study by *Ural et al.* [76] there has been an increased emphasis on bone's hierarchical structure and its influence on bone quality. Material composition and structural design of bone, defined as bone quality, have a critical role in deciding the penchant of bone to to fracture and have the capability to improve fracture risk assessment [76]. Structure determines loads that can be tolerated but loads also determine structure since bone adjusts its material composition and structure to accommodate loads by adaptive modeling and remodeling [65].

To determine the fracture resistance of bone and to understand the role of different toughening mechanisms, it is crucial to look at the fracture as a multi-scale process. Indeed, at each length scale, different mechanisms contribute to bone resistance based on local needs to provide required bone functionalities and mechanical properties at that scale [76, 63]. At the macro-level, BMD is the parameter that is most commonly used clinically to determine bone deterioration with age and to predict bone's susceptibility to fracture [63]. However, research has clearly shown that reduced BMD is just part of the explanation since alterations in other skeletal traits also contribute to increasing fracture risk [9]. In fact, another representative measure of bone quality is toughness (K), defined as the measure of energy absorption capacity up to failure [63].

Descending to a smaller scale, the dissertation is more complex and the exact mechanisms regulating bone fracture have not been clarified yet. However, it is clear that age-related changes in the microstructure such as total porosity, average pore size and osteons may result in alterations in the fracture response of bone [76]. For this reason a more complete overview of the phenomena observed at the micro-scale is needed and is provided in the following section.

1.5.1 Microscale fracture and toughening mechanisms

At the microscale the most prominent microstructural features that influence bone strength and fracture toughness are osteons, cement lines, pores and lacunae [76, 58]. Such discontinuities could turn out to be stress concentration sites for crack initiation, even though various researchers have shown that microstructural barriers are capable of slowing or hindering crack growth. Indeed, fracture in bone is a mutual competition between intrinsic damage mechanisms ahead of a crack tip that advance cracking and extrinsic shielding mechanisms, mainly behind the tip, that prevent cracking. The intrinsic mechanisms, which are observed at length scales less than 1 mm, lead to plastic deformation and an increase in the energy dissipation capacity of the bone with an increase in the structural resistance to the initiation and growth of cracks. The extrinsic mechanisms, observed at the microscale and above, are the main sources of crack dissipation and toughening, by shielding the crack tip from applied driving forces [63, 60].

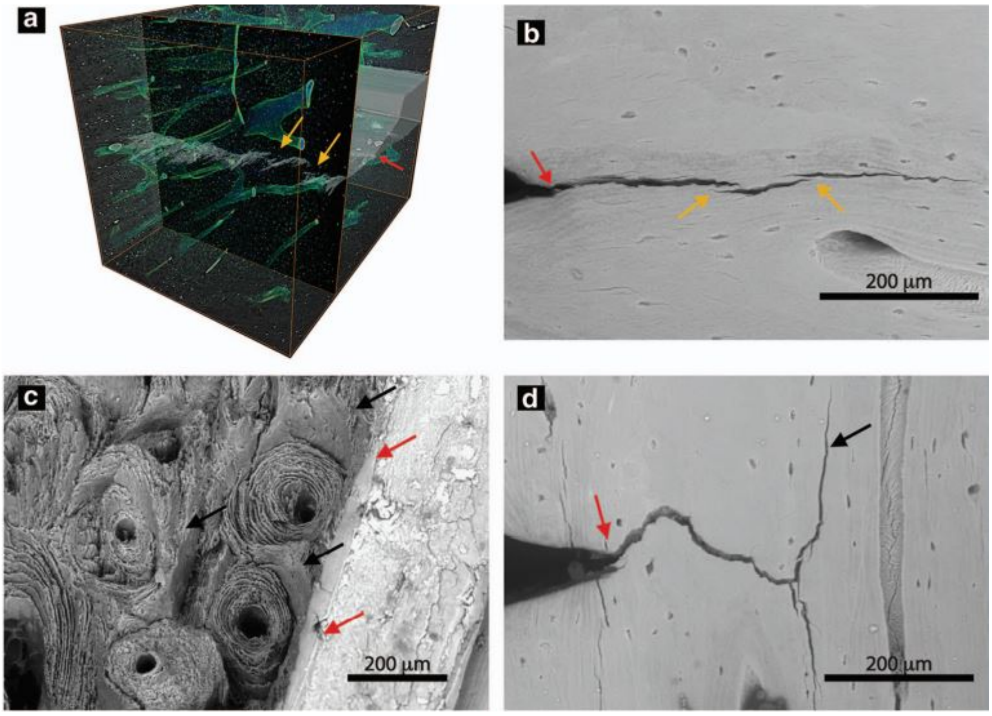

Figure 1.10: Uncraked ligament bridging (a,b) and crack deflection/twist mechanism (c,d). Images from (a) 3-D synchrotron tomography and (b) scanning electron microscopy of uncracked segments (orange arrows) in the wake of the crack generated by microcracking ahead of the crack tip (red arrows). Images from scanning electron microscope on the fracture surface (c) after testing and (d) during the test, of a crack growing from the notch (red arrows) which encounters the interfaces within the bone tissue aligned with the osteons, primarily cement lines, and deflects or twists (black arrows) [86].

The interaction of microcracks and bone microstructures results in extrinsic shielding mechanisms such as crack deflection and twisting, uncracked ligament bridging, collagen fibril bridging and constrained micro-cracking [63]. In bone, crack-tip shielding is developed primarily through crack bridging and crack deflection mechanisms (Figure 1.10) [86]. As a crack grows through the bone structure, collagen fibers or uncracked regions of the bone's matrix can remain intact in the crack wake to form 'bridges' that span the crack opening. These bridges can carry part of the load that would otherwise be used to further extend the crack, thereby lowering the driving force for crack propagation [53]. Crack deflection and twist is another extrinsic mechanism occurring when a crack encounters an interface in the bone, such as the highly mineralized cement lines at the outer boundary of the osteons or the modulating mechanical properties of the lamellae. In this case the crack may grossly deviate from the direction of maximum tensile stress and the driving force can be significantly reduced, slowing the crack progress [86, 60]. In literature is reported that an increase of the bone fracture toughness of 1-2 MPa$\sqrt{m}$ and 3-20 MPa$\sqrt{m}$ was, respectively, found for crack bridging and crack deflection/twist mechanisms, leading to an enhancement of bone's resistance to fracture.

Several studies have highlighted that microdamage in the form of diffuse damage or linear microcracks has been found to accumulate with age, with implications for both bone's intrinsic and extrinsic mechanical resistance. The fracture toughness of bone generally exhibits a steady deterioration with age, both in the longitudinal and transverse direction as highlighted by Table 1.3. Specifically, for crack extensions on the order of millimeters, the crack-growth toughness of young bone is some five times higher compared with aged bone as it is possible to see in the crack-growth resistance curves (Figure 1.11), in which decreases in the crack initiation toughness as well as in the crack-growth toughness are evident with aging [86].

Table 1.3: Reduction per decade in crack-initiation and crack-growth toughness in sample of human cortical bone.

	Crack-initiation toughness	**Crack-growth toughness**
Longitudinal direction	5-11% [8]	12-19% [8]
Transverse direction	1-4% [40]	3% [40]

1.6 Microcracks characteristic parameters

In order to investigate the propagation of the fracture at the micro-scale, it is often necessary to employ powerful high-resolution image techniques. The most used and effective one is the synchrotron radiation, thanks to which it is possible to acquire

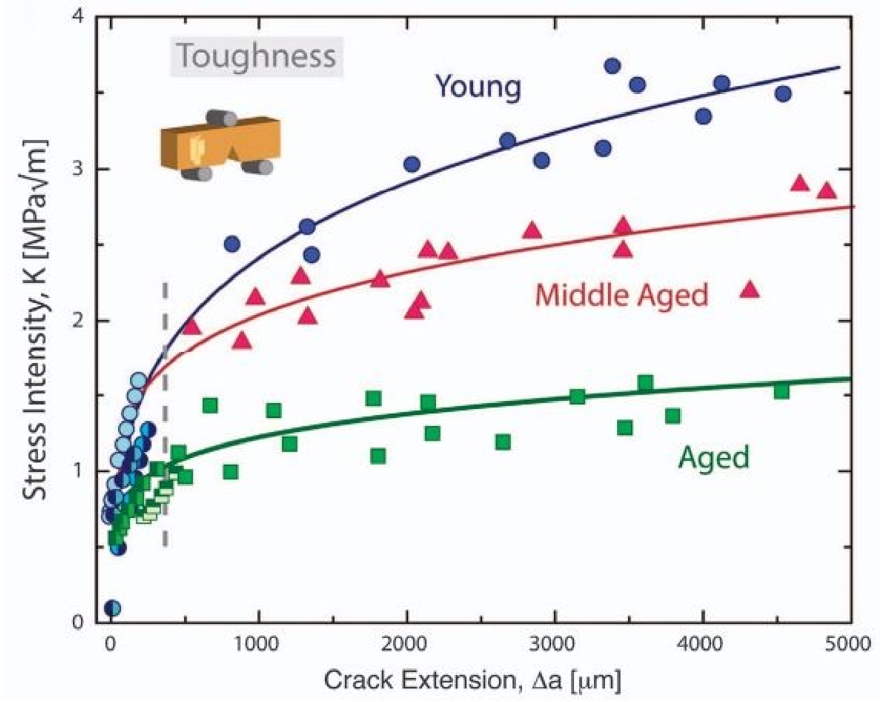

Figure 1.11: Fracture toughness crack-growth resistance curves for young, middle aged and aged samples [86].

tomographies down to the microscale, therefore with the possibility to see lacunae and microscopic cracks [48].

1.6.1 Human bone crack shape and length

In the previous studies [48] was observed that, form a qualitative point of view, different types of crack can appear:

- long linear microcracks, parallel to the trabecular surface (Figure 1.12A);
- microcrack dividing a trabecula (Figure 1.12B);
- microcrack deflected by the interface between two areas of different mineralization (Figure 1.12C);
- crack presenting the bridging phenomena (Figure 1.12D);
- tortuous crack crossing lacunae (Figure 1.12E);
- splitting cracks (Figure 1.12F).

The quantitative measurement of microcracks can be performed with direct segmentation on the 2D images as performed by *Mullins et al.* [51] or on the 3D images of the crack, computing the microcrack length and width as the axis of the best-fitting ellipsoid, as shown in Figure 1.13. The mean length and width of microcracks ranged respectively from 164 μm to 209 μm and 100 μm to 120 μm, while the respective standard deviations ranged from 57 μm to 152 μm and 36 μm to 91 μm. This reflects a high level of variability of microcracks dimensions [42].

1.6.2 Crack tip opening displacement

From the theory of fracture mechanics, an important quantity called the stress intensity factor, K, can be defined. Specifically, K is a measure of the severity of a

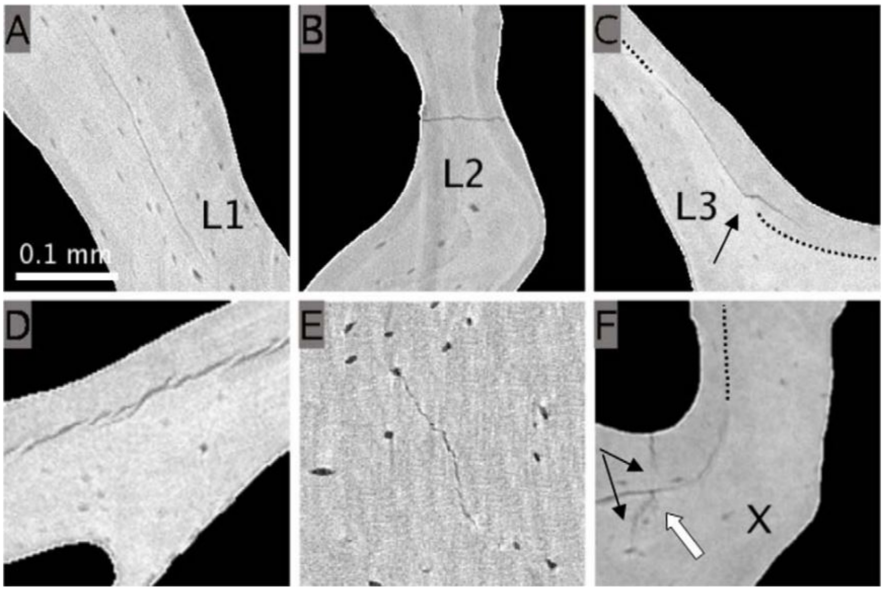

Figure 1.12: Different observable types of crack from micro-CT images [42].

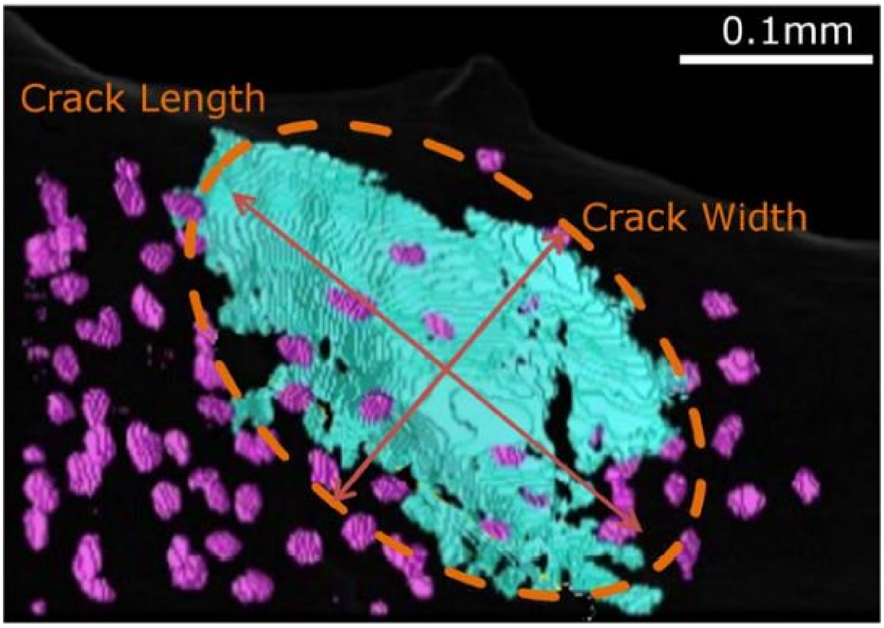

Figure 1.13: 3D rendering of a microcrack with its best-fitting ellipsoid used for the calculus of its length and width [42].

crack situation as affected by the crack size, stress, and geometry. In defining K, the material is assumed to behave in a linear-elastic manner, according to Hooke's law, so that the approach being used is called linear-elastic fracture mechanics (LEFM). A given material can withstand a crack without brittle fracture occurring as long as this K is below a critical value K_c, called the fracture toughness. Values of K_c vary widely for different materials and are affected by temperature and loading rate, and secondarily by the thickness of the part [44].

Another important fracture mechanics parameter is the crack-tip opening displacement (CTOD), to estimate the separation of the crack faces near the tip [85, 44]. Introduced by Wells [82], the CTOD approach is based on the fact that at the crack tip the stresses will always exceed the yield strength and plastic deformation will occur, so it is the plastic strain in the crack tip region that controls fracture. In 1966 Burdekin and Stone [12] provided an expression for CTOD, with a direct relation between CTOD and the stress intensity factor (K_I):

$$CTOD = \frac{K_I^2}{E\sigma_{ys}} \tag{1.2}$$

where E is the Young's modulus and σ_{ys} is the yield stress; showing that in the linear elastic regime the CTOD approach is compatible with LEFM concept [38]. The use of CTOD criterion requires a laboratory measurement of a critical CTOD value, usually associated with the onset of cleavage fracture under plane strain conditions. Such a measurement near the vicinity of the blunting crack tip is difficult and subjective [85].

The early approaches for CTOD measurements were reviewed by Burdekin [50]. The subsequent measurements were estimated using geometrical models inputting displacement measurements made remotely from the crack tip. In particular, a plastic hinge model was developed by Hollstein and Blauel [37] to determine CTOD by assuming that two arms of the specimen rotate rigidly about a plastic hinge point in the uncracked ligament. In order to apply the plastic hinge model to both elastic and elastic–plastic conditions, the total CTOD is separated into elastic and plastic components:

$$CTOD = \frac{K^2(1-\nu)}{2\sigma_{ys}} + \frac{[r_p(W-a)+\Delta a]V_{pl}}{r_p(W-a)+a+Z} \tag{1.3}$$

where a is the crack length, Δa is the crack extension, V$_{pl}$ is the plastic component of the crack mouth opening displacement, Z is the distance of knife edge measurement point from the front face of specimen, r$_p$(W-a) denotes the distance of the plastic hinge point from the cracktip, and r$_p$ is the plastic rotation factor depending on the specimen [85].

In literature information about CTOD for human trabecular bone is missing. *Sharma et al.* reported values of CTOD and K_I of buffalo cortical tibia bone around 0.04 mm in the longitudinal orientation and 0.06 mm in the transverse orientation for the CTOD and around 5.3 MPa$\sqrt{m}$ and in the longitudinal orientation and 12.7 MPa$\sqrt{m}$ in the transverse orientation for the K_I [66]. The measurements of CTOD reported were performed considering the smallest crack mouth opening displacement (CMOD) measured with a clip gauge during the test. Another article by *Bedaiwi et al.* shows values of CTOD around 0.05 mm for human tibial cortical bone [3]. While *Nalla et al.* report values of 1-5 MPa$\sqrt{m}$ for human humeral cortical bone. Further examination about the human trabecular bone has to be performed.

1.6.3 Crack opening displacement

The crack opening displacement (COD) is another parameter to analyse crack growth and refers to the distance between one edge at the other along the crack axis. One of the techniques to measure it, is presented in the article by Muller et al. [18] in which crack profiles were manually fitted by a spline and some landmarks were defined (Figure 1.14). To calculate COD at a certain point x, the normal direction to the crack plane (n) was computed. Then, the relative displacement was measured between two points p$_{1,2}$ at a distance d of 15 voxels from the crack plane such that $p_{1,2} = x \pm dn$.

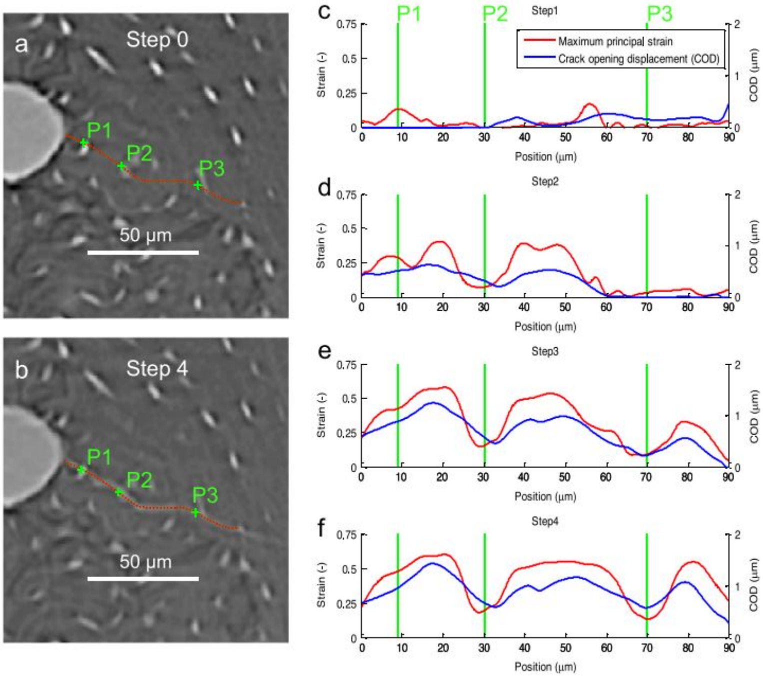

Figure 1.14: Crack profiles (a), (b) shown as an overlay on a maximum intensity projection. Maximum principal strains and crack opening displacements (c)–(f) analyzed for the individual loading steps [18].

Finally, the COD was calculated as the difference of the displacement in the two points along the normal direction to the crack plane: $COD = n \cdot (u(p_2) - u(p_1))$. COD measures were, then, reported in graphs for each loading step, in which is noticeable the further propagation and the consequent opening of the crack, with an increase in COD only up to 1.5–2.0 µm and a maximum value of 1.5 μm (Figure 1.14).

Other works, as the one by Hazenberg et al. [35], are measuring COD directly on the images, only at the mouth of the crack, with values of COD that are reaching almost 4 μm. These data present in the literature are not referring to human bone, so further investigations have to be made.

Aim of the study

This thesis work is part of the bigger GAP project (image-Guided computational and experimental Analysis of fractured Patients), the result of a pluriannual collaboration between *Politecnico di Milano, ETH Zurich, Trinity College Dublin, Gruppo San Donato Milano and ELETTRA Synchrotron Trieste*. The final purpose of this project is to have a complete comprehension of bone fracture mechanisms at its micro-scale, and of the role of lacunae and bone quality in fracture initiation and propagation, in order to predict, with the help of computational models, the eventual risk of fractures at the early stages and allow the formulation of patient-specific treatments.

Particularly, this work is the natural prosecution of the previous thesis projects [32, 4] and covers three main topics:

1. Mapping the local mechanical properties of femoral bone samples with a micro-compressive device (MCD), in order to characterize the mechanical response of bone and spot any trend.

2. Analysing high-resolution tomographic images, to characterize crack propagation and measuring fracture mechanics parameters, and see if there is any correlation between cracks and lacunar network.

3. Creating of a 3D computational model that could predict where cracks would initiate, in order to help visualization and detection of the critical zones.

Chapter 2

Materials and Methods

In the following chapter are described the materials and methods adopted for the entire thesis project. Section 2.1 deals with the experimental tests conduced at *Politecnico di Milano* and the relative femoral sample handling at *Istituto Ortopedico Galeazzi*, meanwhile Section 2.2 concerns the IGFA at *ELETTRA Synchrotron* in Trieste and the realization of a computational model to foresee critical regions. Specifically, the former includes the passages to prepare and create the trabecular specimens (Section 2.1.1), a description of the MCD testing machine and its functioning together with the testing procedure (Section 2.1.2) and the output analysis to obtain the final values of the local mechanical parameter (Section 2.1.3). The latter is focused on tomography, the operating parameters and set-up and (Section 2.2.1), the acquisition procedure (Section 2.2.2), on the multi-step process to obtain the final .TIFF images and their analysis to discern bone and crack parameters (Section 2.2.3) and finally, the procedure to obtain a 3D model of the whole bone specimen, capable of predicting the most critical zone (Section 2.2.4).

2.1 Experimental mechanical testing

In this section are described all the fundamental passages to obtain, starting from femoral head surgery, the finished trabecular sample. Then, are briefly reported the design and functioning of the MCD used for testing along with the testing procedure and the final output analysis.

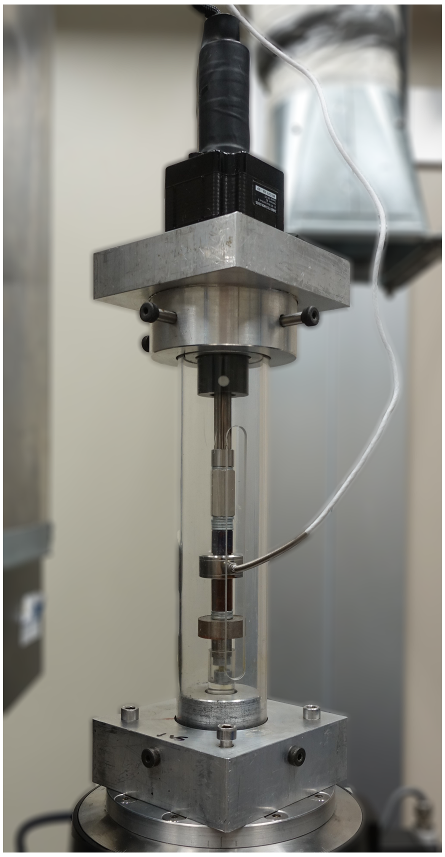

Figure 2.1: The Micro-Compression Device used for mechanical tests on human trabecular bone.

2.1.1 Femoral head partitioning and sample preparation

As previously discussed, the initial part of this study aims to test both healthy and osteoporotic human trabecular bone samples through an axial quasi-static micro-compression device. The essential collaboration with *Gruppo San Donato Foundation* allows to collect surgically removed femoral heads, prior authorization from the ethic committee and the patients themselves.

Each femoral head removed from the patient is immediately partitioned by the surgeon in the operating room right after the osteotomy, with a circular saw, obtaining three different regions along the coronal plane identified as Z1, Z2 and Z3 (Figure 2.2).

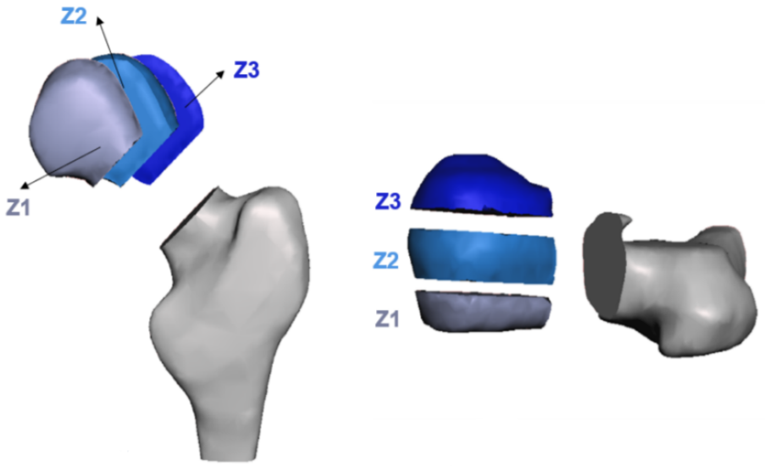

Figure 2.2: Femoral head sectioning along the coronal plane. Zones can be identified from lighter blue (Z1) to darker blue (Z3).

Each zone is then divided along the sagittal plane into three zones: proximal (P), medial (M) and distal (D) (Figure 2.3). Once the partition is concluded, the nine sub-regions are transferred to the *Histology Laboratory of Istituto Ortopedico Galeazzi* in Milan, where a biotechnologist, using a diamond blade (Buehler IsoMet Blade, 15HC, 152 mm), extracts parallelepided samples with $16mm^2$ in section and $14mm$ in height. Samples are then fixed in formaldehyde and stored in ethanol 70% to kill bacteria and prevent bone degradation. The last step to complete the samples is to fix the extremities into epoxy resin endcaps, obtained pouring resin into silicon moulds. The endcaps were designed and perfected in *Politecnico di Milano*. The

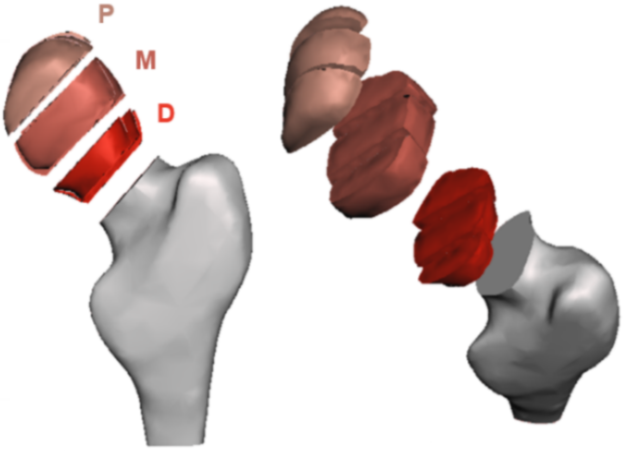

Figure 2.3: Sub-sectioning of the regions Z1, Z2, Z3 along the sagittal plane in proximal (P), medial (M) and distal (D). Zones can be identified from lighter red (P) to darker red (D).

last version [4], despite being excellent in the design (Figure 2.4), was lacking in precision due to the making procedure: the silicon mould suffers severe wear and does not guarantee planarity of surfaces, bringing to coarse endcaps and non-planar samples. For this reasons, as presented in the *Results* chapter, their realization has been renewed, opting for 3D printing of PLA filament here in *Politecnico di Milano*.

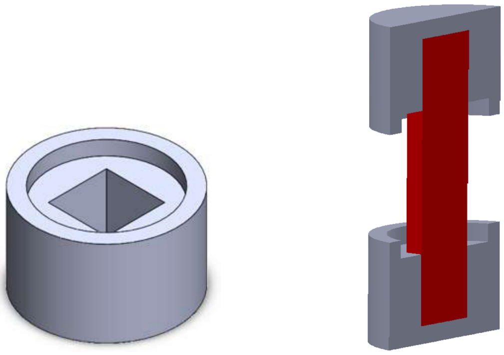

Figure 2.4: Ultimate endcap design (left) [4] and section of the mounted specimen (right).

2.1.2 Testing protocol

In this study 8 femoral heads have been analyzed, of which 4 come from osteoporotic patients (FH2, FH3, FH4, FH8) and 4 from non-osteoporotic ones (FH1, FH5, FH6, FH7) . In Table 2.1 are reported complete information about each femoral head.

Table 2.1: Specific information for each FH: age, gender, radiologic information, and additional clinical observations. The definition of osteoporosis reported, is in accordance with the World Health Organization (WHO) guidelines.

Femoral head	Age [yrs]	Gender	Radiologic diagnosis	Observations
FH1	61	Female	Non osteoporotic	Large bone spurs
FH2	90	Female	Osteoporotic	-
FH3	62	Female	Osteoporotic	Local arthritis
FH4	84	Female	Osteoporotic	Thick cortical shell
FH5	76	Female	Non osteoporotic	Detected osteopenia
FH6	56	Female	Non osteoporotic	Local displasic arthritis
FH7	59	Female	Non osteoporotic	Detected osteopenia
FH8	77	Female	Osteoporotic	Local arthritis

All mechanical tests, both the ones performed in Milan and the ones in Trieste, were performed with this device that was already designed, manufactured, verified [32] and refined [4] at the *DMEC Laboratory of the Politecnico di Milano*. Its peculiarities are lightweight, easy assembly, 360° transparency around the sample, in order to fulfill the requirements for the tests at the IGFA.

The testing procedure here described is carried out at *Politecnico di Milano* and follows several steps. Preliminary, trabecular bone samples are re-hydrated in saline physiological solution and then the distance between the two endcaps is measured with a digital calibre and increased by 2 mm (corresponding to the unconstrained bone in the two endcaps) to obtain the effective length of that sample. Due to the craftsmanship of the sample preparation, there's a huge variety in dimension with respect to the ideal 14 mm, so it is important to measure their real height. After that, specimens are inserted inside the inner cylinder, wet with physiological solution and then the machine is mounted. Using specific *ARDUINO* codes, the plate is calibrated

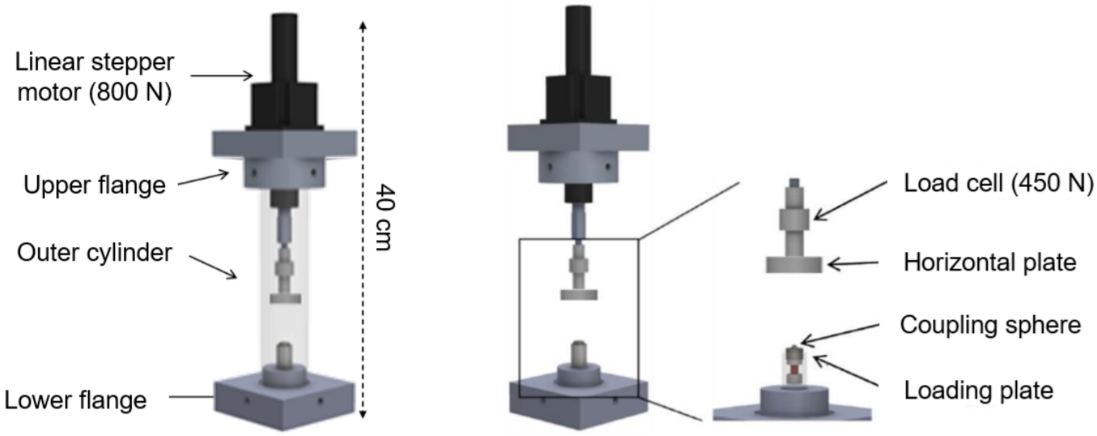

Figure 2.5: Scheme of the MCD [32, 4]. Eighth main components can be identified: the outer transparent cylinder inserted between the upper and the lower flange, the linear stepper motor which allows a precise displacement, the load cell and the horizontal plate which transmit the displacement to the sample, placed inside the transparent inner cylinder, and the coupling sphere that prevents shear loads.

and a pre-load of 2-3 N is applied with 3 consecutive cycles in order to assure the contact between plate and specimen. Once these preliminary operations are completed, the axial quasi-static micro-compressions are applied to the trabecular bone samples. Twelve micro-compressions per sample are performed, with a step amplitude of 0.1 mm and a displacement rate of 0.1 mm/s. Each compression step is followed by 3 minutes-relaxation time where the displacement is kept constant. The instantaneous load measured by the cell and the apparent strain of the sample are recorded with a sampling frequency of 10 Hz and directly send to a Microsoft Excel sheet by the PLX–DAQtool, which plots the output data in real-time allowing them to be continuously monitored during the test. Once the test is finished (40min approximately) the MCD is disassembled and the broken specimen is carefully removed.

The output coming from the micro-compression tests, namely the apparent strain applied by the motor plunger and the load measured by the cell (Equation 2.1), have

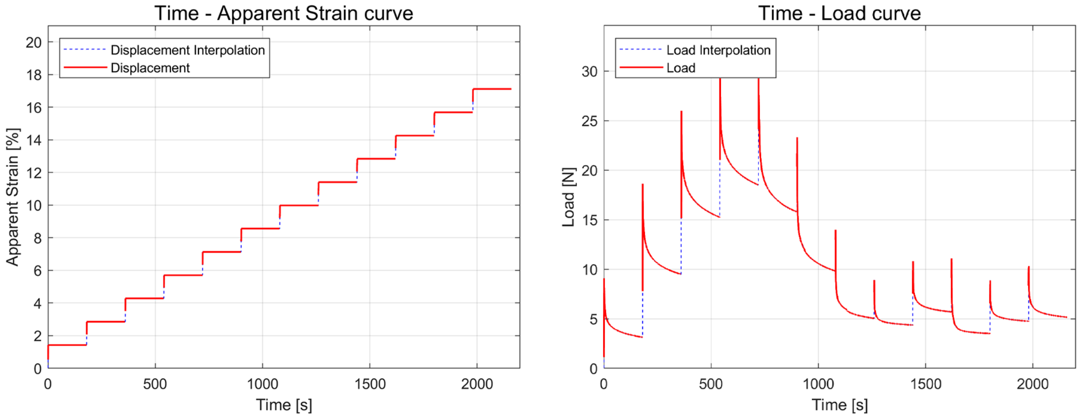

Figure 2.6: Graphs showing the 12 compression-steps of 0,1 mm each (left) and the corresponding load produced by the sample (right). Eventual negative values caused by internal compliances and system adjustment are removed by the code and substituted with blue-dotted lines.

to be processed in order to evaluate the mechanical properties at the sample level.

$$\sigma_{app} = \frac{load}{nominal\ area} \qquad \varepsilon_{app} = \frac{\#step \times 0.1}{L_{eff}} \tag{2.1}$$

To do so a dedicated *MatLab* code is used, that plots graphs for the apparent strain and stress vs time and the $\sigma - \varepsilon$ graph. From the latter, it extrapolates the values of ultimate stress (identified as the maximum point of the curve occurring before the first drop) and the corresponding ultimate strain, calculates the Young's Modulus from the linear region (which is usually between the first four compression steps), and yield strength is detected using the 0.2% strain offset method.

2.1.3 Statistical analysis

All mechanical parameters acquired from the micro-compressive tests and the subsequent analyses, undergo statistical analysis with the certified software *Minitab*. As a preliminary procedure, all data undergo the Shapiro-Wilk normality test, in order to verify whether or not data have a normal distribution. At this point two different

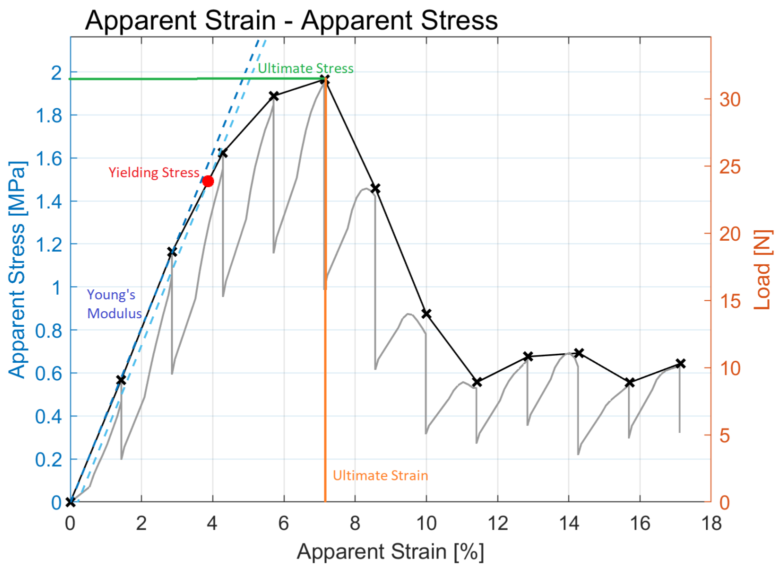

Figure 2.7: The final $\sigma - \varepsilon$ graph obtained with MatLab. Here are reported the mechanical properties: ultimate stress (green), ultimate strain (orange), yielding strength (red) and the blue-dotted line representing the linear part, from which Young's Modulus is obtained.

scenarios are possible:

- In case of normal data ($p > 0.1$), the 2-sample t test or the ANOVA test are used. The former is for comparing two different groups, while the latter to compare three or more. The confidence level is set to 95% with the initial hypothesis of equal means, so a p-value < 0.05 is required to have statistical difference. Moreover, Tukey test is performed to show the even-tual belonging to different groups
- For non-normal data ($p < 0.1$) the corresponding tests are the non-parametric Mann-Whitney (two groups) or the Kruskal-Wallis (three or more groups).

2.2 Synchrotron-based imaging

In the following section the procedure to obtain SRµCT images at the *ELETTRA Synchrotron* is presented, and in particular the *SYRMEP (SYnchrotron Radiation* *for MEdical Physics)* beamline and scanning parameters are briefly described. Then the post-processing of such images down to lacunae-resolution is depicted, and their subsequent analysis to obtain relevant information about crack propagation and parameters is described in detail.

2.2.1 Set-up and scanning parameters

Table 2.2: Scanning parameters during image acquisition.

Parameter	Value
Electron beam energy	2.0 - 2.4 GeV
Emitted beam energy	20.0 - 25.6 keV
Si thickness	1.5 mm
Sample to detector distance	150 mm
Pixel size	1.6 µm
Angle of scanning	360.2°
Projections	1802
Field of View (FOV)	3.28 x 3.28 mm

The imaging process is performed inside the experimental hutch of the *SYRMEP* beamline, one of the 28 available light sources of the *ELETTRA Synchrotron* specifically designed for medical purposes. The monochromatic beam emitted has an energy in the range of 20-30 keV, depending on the synchrotron light source, which can vary from 2.0 to 2.4 GeV depending on the operating conditions. The electron beam, before being emitted, is filtered by a silicon foil (1.5 mm thick) to reduce noise and sharpen its spectrum, and then reaches the trabecular bone sample housed in the MCD. After crossing the sample, the beam is detected by the scintillator behind, which is located at a distance of 15 cm from the specimen. Images are acquired with 1.6 µm resolution and over an angular range of 360.2° with 1802 projections: the +2 abundance is to prevent eventual delay in the rotating platform. The scan is done in fly mode, indeed the MCD continuously rotates on the platform during the acquisition and one flat field image (without the sample) ad one dark field image (without X-ray illumination) is taken. The calibration procedure is done previously by the *ELETTRA* technicians. All parameters are summarized in Table 2.2.

2.2.2 Testing procedure

The IGFA follows mostly the same testing operations as for the ones described in Section 2.1.2, with the exception of the stops in the compression steps to acquire tomographic and radiographic images. Bone samples are hydrated for 24hrs in physiologic solution, then measured with a digital calibre and mounted on the MCD and then the calibration procedure with *ARDUINO* codes is performed. With the aim of capturing and visualizing crack initiation and propagation, the compressive steps are not performed all at once, but different acquisitions among them are required. In particular, analyzing the general trend of apparent stress-strain curves of previously tested samples, a general protocol is chosen to fit at best the salient points of those curves. Of course each specimen behaves in its on particular way, and it is impossible to know exactly where fracture will start, but with this method is possible to have a general view for all samples, and moreover, the protocol can be slightly changed for each singular femoral head. As clearly shown in Figure 2.8, for all samples an unloaded acquisition (STEP 0) is performed firstly, to visualize the initial situation. Then, for non-osteoporotic bones the following acquisition are taken at 0.4 mm (STEP 1) and 0.8 mm (STEP 2) displacement, while for osteoporotic ones the acquisitions are taken at 0.3 mm (STEP 1) and 0.6 mm (STEP 2). For both groups the last acquisition is set at 1.5 mm displacement (STEP 3) where the specimen is fully collapsed.

During each acquisition, both a tomographic and a radiographic image are taken:

- **Tomographies** are used to evaluate lacunar parameters and distribution and crack propagation inside trabeculae. Since the FOV is 3.28 mm maximum, for

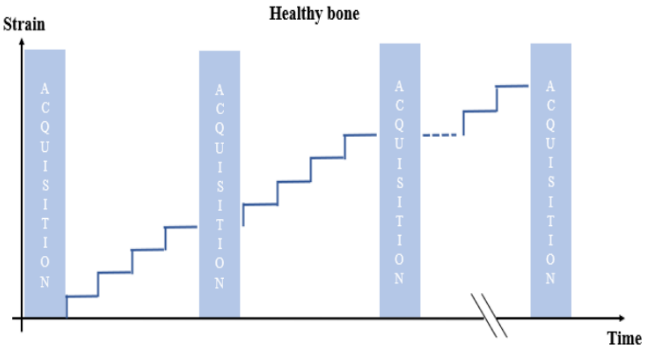

Figure 2.8: Scanning protocol of the IGFA for healthy bone samples

each acquisition step multiple scans are needed to cover the entire specimen length (typically 3, named from top to bottom H0, H3 and H6), with a certain overlap. So in total, for each specimen 12 scans are performed.

- **Radiographies** are used to evaluate sample inclination with respect to the horizontal axis and determine if the displacement has been completely transferred from the plate to the sample. For this aim, radiographic imaging is performed both at 0° and 90° rotation. Firstly 4 consecutive images of the top metallic sphere are taken, then all the bone sample is imaged, where each image is 3 mm wide.

2.2.3 Tomography analysis

Tomographic projections of the sample are acquired and stored in compressed raw files .TDF, to be processed afterwards. From this stage, several steps must be applied to those files to obtain complete information about bone fracture.

- Reconstruction: the raw .TDF file must be converted into a set of bi-dimensional image files (slices) of the entire volume to be visualized.
- Image filtering: cleaning up the raw images from noise and imperfections, especially in the voids region.

- Crack history reconstruction: visualizing the slices at the different acquisition steps, it is possible to find cracks and reproduce their propagation history inside the specimen.
- Measurements of crack parameters: in order to characterize cracks , it is possible to measure directly from tomographic images their length, height, propagation velocity, COD and CTOD.
- 3D crack model: once a crack is detected, all slices containing it are stitched together, creating a tri-dimensional visualization of it.

Reconstruction

Reconstruction is a high computational and memory-demanding phase. A single subset of the specimen and is subdivided in 2048 slices acquired at a distance of 1.6 μm, giving an overall height of 3.28 mm. The raw .TDF file associated with a sub-set has a dimension of about 26 GB. This file must be converted into a set of 2048 squared .TIFF images with dimensions in the range of 3500-4000 pixels for each side, leading to about 150 GB data-set. Moreover, a single specimen requires 3 or 4 tomographic acquisition for each of the 4 compression steps, as previously explained in Section 2.2.2. When processing SRμCT data, it is important to set the right parameters to avoid image defects, such as stripes and ring artefacts, metal and material attenuation of the beam, shifted rotation centre and misalignment.

The software used is *SYRMEP Tomo Project (STP) v 1.6*, an open-source software used and implemented at the SYRMEP beamline. Many of the parameters for the reconstruction are dependent on the experimental setting used, and so are precompiled and not changed. The ones tuned for the reconstructions are: the *extended field of view overlap*, the α/β *ratio* for grey-scale phase retrieval and *angle projections*. The optimal value is, in first attempt, guessed automatically by the software, and then confirmed or slightly modified manually watching the result in a reduced volume (preview). This last step is very important to be carried on before launching the reconstruction, otherwise there is a huge waste of computational time. The final result can be seen in Figure 2.9.

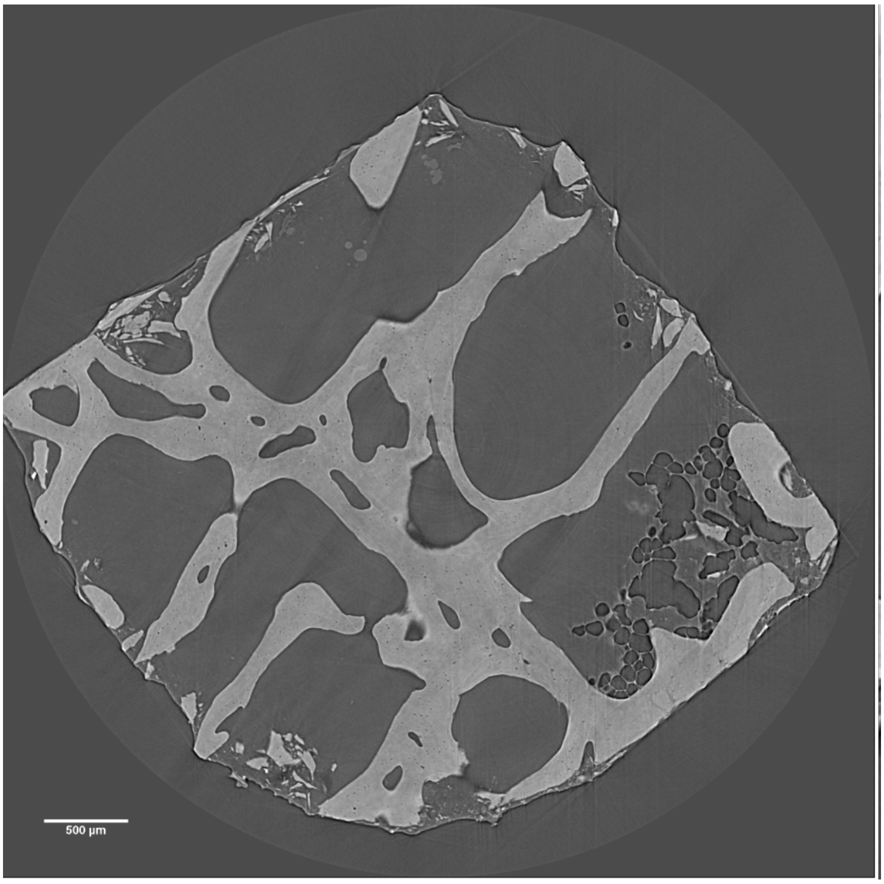

Figure 2.9: Reconstructed image. It is immediate to notice some disturbing elements such as bone particles, spots and stripes and formaldehyde voids.

Image filtering

As clearly shown in Figure 2.9, the reconstructed images contain a lot of noise and disturbing or unwanted elements, especially in the inter-trabecular voids due to formaldehyde fixing. Because of this, a filtering and cleaning procedure is needed, and consists

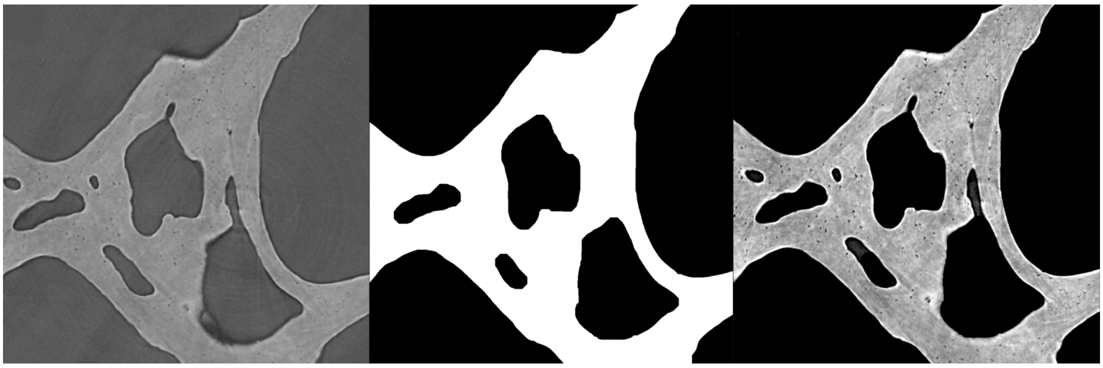

Figure 2.10: Image filtering process: focus on non-filtered image (left), the applied binary mask (center) and the final processed image (right).

in a series of passages through different *MatLab* codes implemented by *Bertolini & Bracco* [4]:

1. Gaussian filter with 2.5 standard deviation;
2. Binarization, to distinguish between voids and bone using a threshold value in the pixel gray-scale;
3. Opening operation with a squared kernel of 15 pixels;
4. Closing operation using disk-shaped kernel of 20 pixels;
5. Mask application, to clean the original image without loosing in resolution.

The final result can be seen in Figure 2.10.

Crack history reconstruction

After the above mentioned preliminary procedures, it is possible to visualize the 2D-slices at the different time steps. Since the aim is to reconstruct the propagation in time of cracks inside trabeculae, a time-consuming consultation of all the 2048×12 images per sample is needed. The software used for this operation is the open-licence *Fiji-ImageJ*.

First of all the research for cracks starts at the last acquisition step (step 3), where the specimen is completely broken and so there are surely cracks. Then, selected the fracture of interest, the same search is done on the preceding steps (step 2, step 1 and step 0), trying to find the closest one-to-one correspondence as possible between the single slices. Once found this correspondence, the serial number of the slice and the total number of interested slices are noted for each step, to make it easier future re-examinations.

Measurement of crack parameters

Thanks to the extremely-high resolution of the images (down to 1.6 µm per pixel), it is possible to measure directly on them multiple crack parameters, again using *Fiji-ImageJ* software.

- Crack length is measured using the 'Measure' tool, with the scale set to 1 pixel=1.6 µm. Along the cross-section plane (XY plane) the crack path is run with a segmented line and its length is annotated, while along the height of the specimen (Z direction), is counted the number of slices containing the crack and then multiplied for the scaling factor.

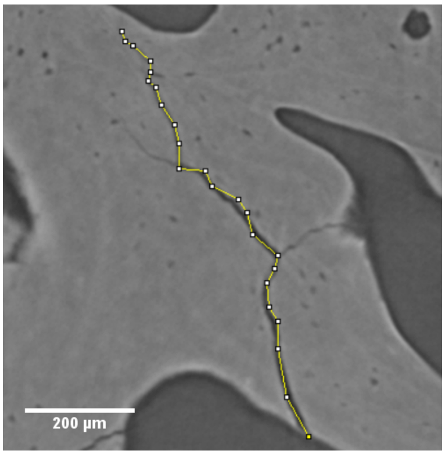

Figure 2.11: Crack length measure with ImageJ segmented line tool.

- Propagation velocity can be easily calculated by measuring crack length in two subsequent tomographic acquisitions and adapting the formula from fracture mechanics:

  $$v_{crack} = \frac{\Delta a_{step(n)-step(n-1)}}{\Delta t_{step(n)-step(n-1)}} \tag{2.2}$$

  Where Δa is the difference in length (or height) of the same crack between the two subsequent steps, while Δt is the interval of time between one acquisition and the following (see Section 2.2.2). It must be mentioned that this is an approximated method, since it is impossible to know precisely at which compression step the crack initiated; we only have two subsequent acquisitions that differ from several compressions to compare. Not finding any other similar procedure on literature, we arbitrary chose to adopt this convention. Calculating it both in the XY plane and in the Z direction, it is useful to calculate a total velocity as the vector sum of the two, with its module being the pitagoric sum of their values: $v_{XYZ} = \sqrt{v_{XY}^2 + v_Z^2}$.

- COD and CTOD can be directly measured, as well, using the same software. For COD, being intrinsically a variable quantity along the crack, multiple measures are taken for the single crack along its profile. Repeating the measures in the same points but in the corresponding image of the previous step, it is possible to calculate a COD widening velocity, with the exact same Equation 2.2 as for crack propagation. Regarding CTOD, being the value very close to the tomographic resolution, it has been arbitrary decided to measure it inside the crack tip-zone considering the darkest-gray pixels.

- From the values of CTOD it is possible to calculate the corresponding toughness values (here called K$_{CTOD}$) with the approximated Equation 1.2, and compare the results with the toughness (K$_I$) found using the classical LEFM equation:

$$K_I = Y\sigma_n\sqrt{\pi a} \tag{2.3}$$

Two different approaches were taken into account for the selection of the material properties. The former consists of obtaining the values directly from the experimental stress-strain curve and considers the material as it was not porous, the latter accounts for bone porosity following *Gibson and Ashby "density power law model"* [29], assuming a linear relationship. In the following Table 2.3 the obtained values are displayed. For the values of BV/TV a 20% was chosen for the OP bone and 30% for the non-OP one [57, 71].

Table 2.3: Values of Young's modulus (E), yielding stress (σ_y) and BV/TV of the analyzed specimens. The values obtained considering the sample as non-porous are indicated with the superscript "sample", the ones obtained taking account of the porosity with the superscript "bone".

	E^{sample} [MPa]	σ_y^{sample} [MPa]	BV/TV [%]	E^{bone} [MPa]	σ_y^{bone} [MPa]
FH1-S7	162.0	7.0	30	540.5	23.2
FH2-S53	12.0	0.7	20	60.0	3.5
FH4-S31	97.6	4.3	20	488.0	21.5
FH5-S33	107.0	8.3	30	358.0	29.0

3D crack representation

The single slices containing the same crack can be piled up, thus obtaining a high-resolution tri-dimensional representation of the fracture as in Figure 2.12. To obtain this result, again with *Fiji-ImageJ*, it is necessary to decouple the three most important elements at the trabecular level: crack, bone and lacunae. Once isolated, inside the whole slice and along the specimen height, the smallest portion containing the entire crack, the images must be cropped in that area, then binarized and inverted. In this

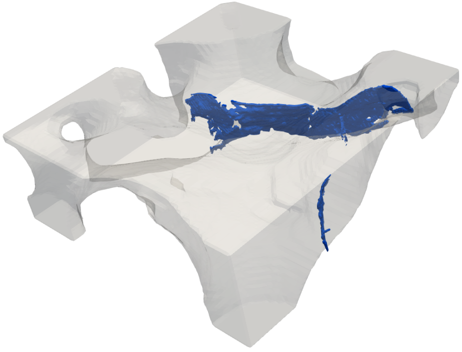

Figure 2.12: Tri-dimensional visualization of a crack (blue) propagated inside trabecular bone (grey).

way we only have voids and bone in b&w scale. Using the 'Subtract Background' tool with a radius = 3±1 pixel, we can erase all that is not part of the crack, then, using the 'BoneJ Isosurface' command, the stitching procedure is implemented and an .STL file containing the model is created. At this stage, due to the radius chosen in the subtraction operation, also some lacunae are present in the model, but they are quite deformed and irregular, since the procedure is tailored just for wider voids such as cracks. They could be useful for a preliminary study of lacunae distribution and eventual interactions with the crack, but their rendering precision is low. Nevertheless, erasing those disturbing elements is quite easy by means of any 3D-visualizing software such as *Paraview* or *Rhinoceros*. To obtain the bone-model, it is necessary to repeat the same procedure, cropping at the same coordinates as before, but this time using the masks obtained from the filtering procedure instead of the finished images, and inverting the selection. The precise rendering of the lacunar network can be obtained with a dedicated *Python* code provided by *ETH Zurich*. The complete visualization is performed on *Paraview*, overlapping the .STL file containing the crack, the one containing only bone, and the eventual lacunae.

2.2.4 Computational model of human bone

Considering the complexity of the localization of cracks, the implementation of a 3D model for the whole bone may be of help to localise the most stressed region. The aim of this section is to describe the procedure in order to obtain the 3D model of the entire sample of interest.

Since the electron beam is not able to entirely cover the length of the specimen, sample tomographies are acquired in separate sub-sets (tipically 3). Hence, to obtain a complete model of the specimen a 3D stitching of the sub-sets must be performed using *Matlab* code implemented by *Bertolini & Bracco* [4], with the scope of correcting any overlaps in the vertical direction and any shifts in the horizontal plane. The output images have all the same dimension and are saved downcasting the original 32-bit to 8-bit in order to keep the dataset manageable. These images are imported in the software *Fiji-ImageJ* and, using the 'BoneJ Isosurface' command, it is possible to obtain a .STL file. The latter can be visualized using the software *Paraview*, as shown in Figure 2.13.

Finally, using another Matlab code implemented by *Bertolini & Bracco* [4], it is possible to compute the BV/TV value for each slice, considering the ratio of full pixels over the nominal section of the specimen, in order to obtain the visualization of the BV/TV trend for the whole sample (Figure 2.14).

Once the isosurface is generated, one very fast method to obtain the solid mesh is the Shrink Wrap Mesh operated by *Altair Hypermesh*. In this case the hexaedral mesh was chosen since this type of mesh is highly recommended for models that involve bone [13]. After choosing the element type, in order to choose the element size, it has been necessary to do a convergence analysis in order to choose a size that is good enough such that it does not change the output of the simulation, but, at the same time, that guarantees an appropriate computational time. The convergence analysis has been carried out through Abaqus with the sample being meshed with different

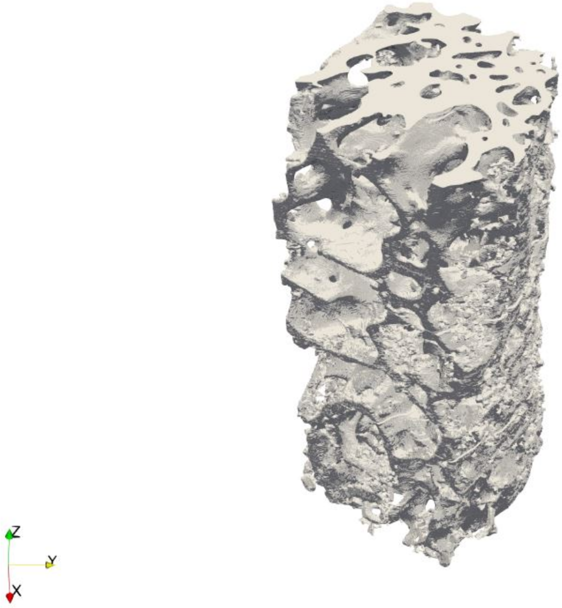

Figure 2.13: 3D model of the sample of interest from the non-osteoporotic femoral head FH5.

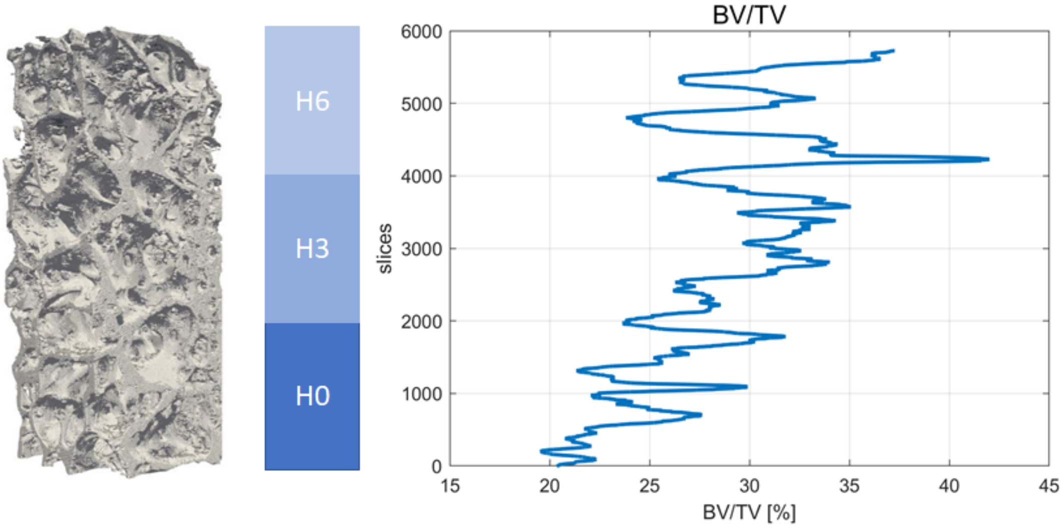

Figure 2.14: BV/TV distribution of the sample of interest extracted from the non-osteoporotic femoral head FH5.

element sizes reported in the Table 2.4, with the corresponding value of the maximum principal stress at the critical point.

Table 2.4: Different element sizes and maximum principal stress values at the critical point for the convergence analysis.

Element size	S max principal [MPa]
15	15.08
13.5	19.47
12	21.67
10.50	19.68
9	21.23
7.5	28.88
6	28.94
4.5	32.92

The result of the convergence analysis is represented in Figure 2.15, from which is possible to state that, once the element size is smaller than 7.5 the variation of the displacement is not significant, therefore a 7.5 mesh size has been chosen for the presented analysis.

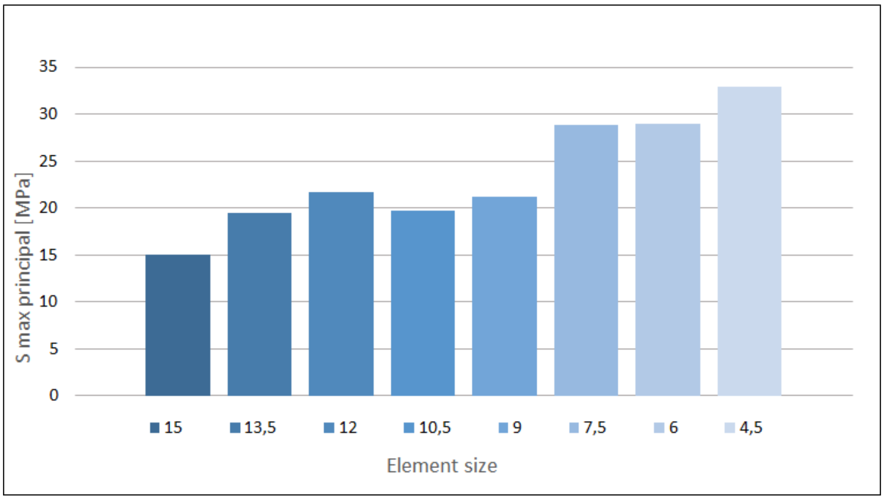

Figure 2.15: Convergence analysis graph.

In Abaqus a linear elastic simulation is performed, with the aim of reproducing the mechanical test explained in Section 2.2.2. The specimen is fixed at the base with an encaster and on the top surface a displacement of 0.4 mm is applied, in order to simulate the STEP 1 of the mechanical test (Figure 2.16). The material input for the bone are a Young's modulus of 413 MPa, derived from the experimental test, and a Poisson's ratio of 0,3.

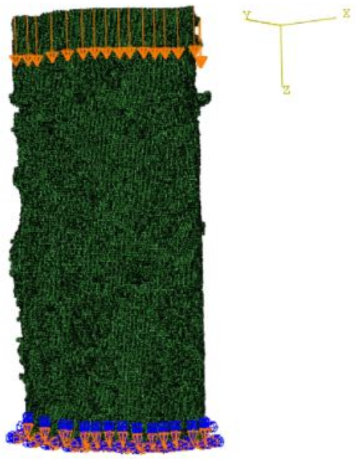

Figure 2.16: Set up for the FEM simulation in Abaqus.

Chapter 3

Results

3.1 Testing and mechanical properties

3.1.1 Endcap 3D printing

As previously hinted in Section 2.1.1, handmade epoxy resin endcaps have a problematic issue with surface finishing, tolerances and planarity, due to the severe wear of the silicon mould. For this reasons a 3D printing procedure has been implemented at the *HAPRE lab of Dipartimento di Meccanica in Politecnico di Milano*. Material selection criterium was based on its Young's modulus and hardness value, which must be higher than bone's, in order to assure complete transfer of the displacement to the sample and also as close as possible to the epoxy ones. All properties are taken from *Ultimaker* materials data-sheets or, as for the epoxy resin, from the *Cambridge Engineering Selector (CES)* materials database. As reported in Table 3.1 the best candidates were poly-carbonate (PC) and poly-lactic-acid (PLA), both already present in the laboratory. The final choice fell on PLA, due to its higher value in Modulus and better printing parameters (printing speed, filament handling, vessel temperature), together with its environmental-friendly peculiarities: PLA is in fact biodegradable

Figure 3.1: Endcaps comparison. On the left the old epoxy-resin one with some defects and residual scrap, while on the right the new 3d-printed PLA one, showing excellent finishing and geometrical precision.

and comes from biological and renewable sources.

Table 3.1: Material selection. For each candidate is reported its producer's brand, Young's Modulus (E), Hardness Shore D.

Material	Brand	E [GPa]	Hardness ShoreD
Epoxy resin	Buehler	1.7-2.5	80
Poly-Carbonate	Ultimaker	2.13	82
Poly-Lactic-Acid	Ultimaker	2.35	83

The same design was maintained, only the outer cylinder diameter was shortened from a nominal 10 mm to 9.6 mm, to allow higher tolerances with the coupling sphere. For printing it has been used a *Ultimaker S5* with the printing parameters reported in Table 3.2.

Table 3.2: 3D Printing parameters.

Material	Ultimaker PLA Silver metallic AA0.4 mm
Profile	Fine 0.2 mm
Infill	100%
Brim width	2 mm

The new manufacturing process allows precise surface finishing and tolerances, planar surfaces and prevents the formation of hardly-removable residues at the endcap base. In return, samples are easier to assemble and are more aligned along the vertical axis, showing less inclination and so a better distribution of the compressive load.

3.1.2 Local mechanical characterization of femoral heads

As presented in the Materials and Methods section 2.1.3, a statistical analysis was performed. Even if some border-line distributions (p-value around 0.1) were detected, being the ANOVA test highly resistant to non-normal data distribution, the introduction of a non-parametric test was unnecessary. In FH2, FH6, FH8 specimens coming from zone Z3 were unavailable, so a 2-sample t-test was performed on them, having only to compare two groups. This test was also used to compare the mechanical properties between healthy and osteoporotic groups.

Below are reported the results of these analyses, comparing, for each femoral head, the values of the mechanical parameters between the different zones (Z1, Z2, Z3) and subzones (P, M, D) of extraction. Boxplots signed with an orange dot mean that a statistical difference has been detected.

Table 3.3: Statistical comparison between femural zones and subzones in FH1.

FH1	Zones	Subzones
E [MPa]	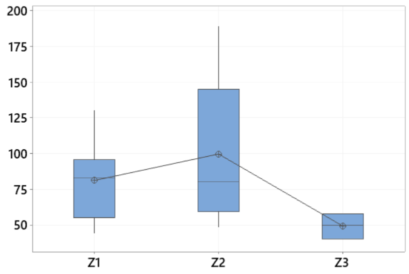	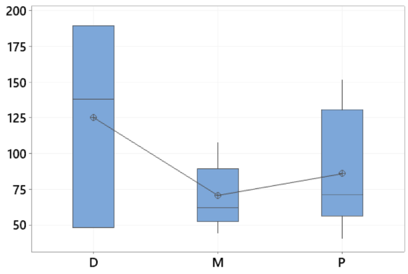
σ_y [MPa]	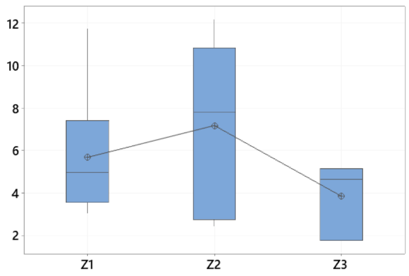	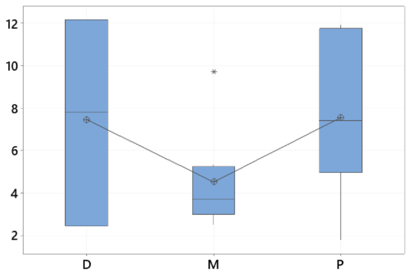
σ_u [MPa]	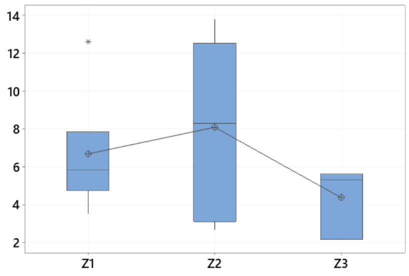	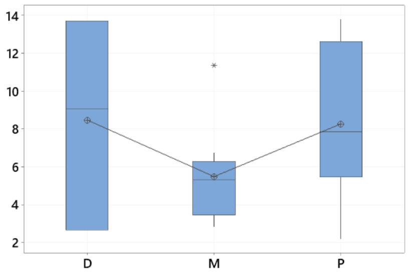
ε_u [%]	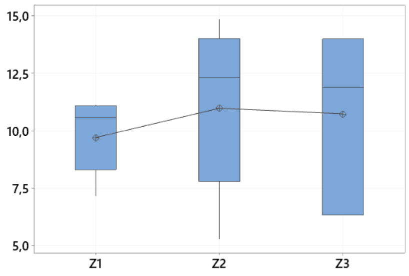	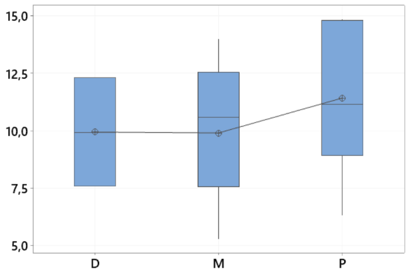

Table 3.4: Statistical comparison between femoral zones and subzones in FH2.

FH2	Zones	Subzones
E [MPa]	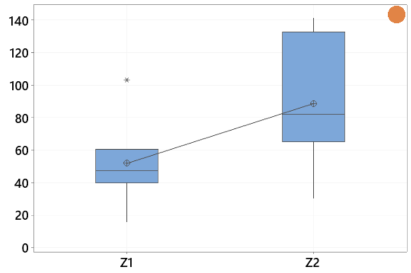	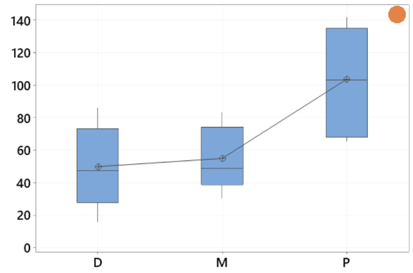
σ_y [MPa]	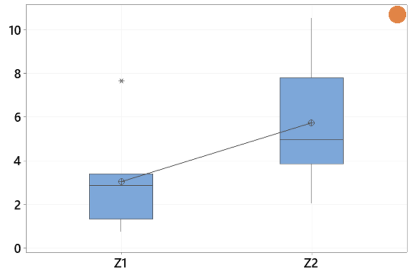	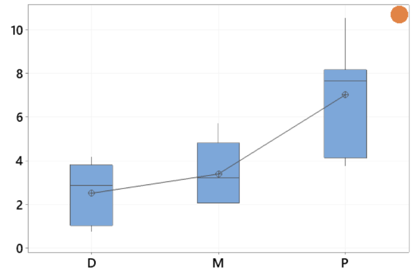
σ_u [MPa]	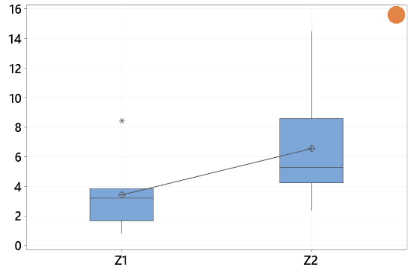	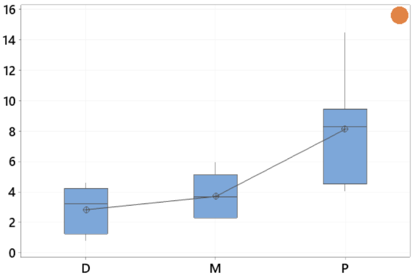
ε_u [%]	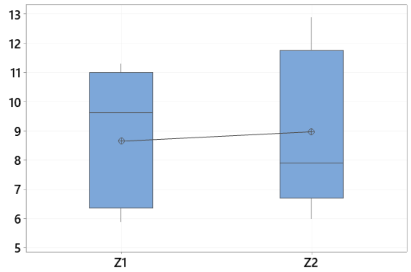	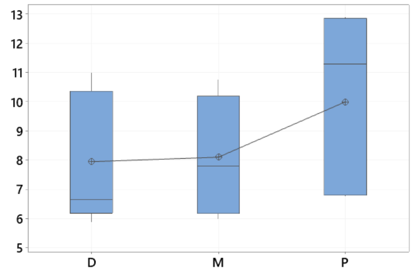

Table 3.5: Statistical comparison between femural zones and subzones in FH3.

FH3	Zones	Subzones
E [MPa]	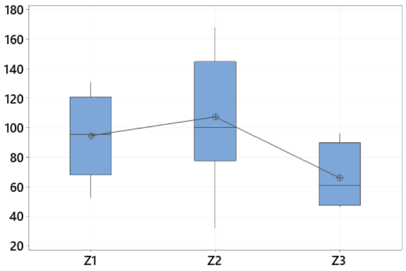	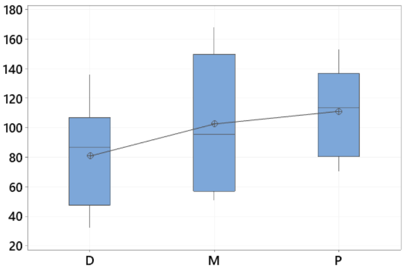
σ_y [MPa]	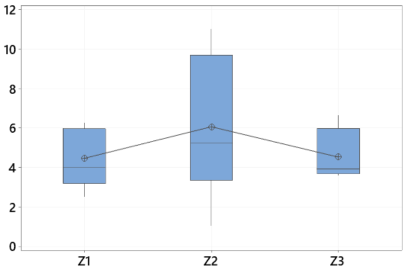	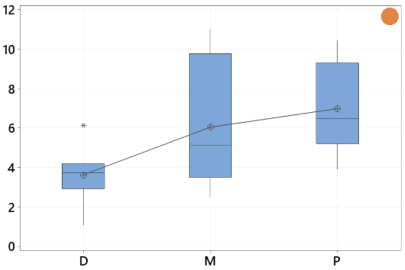
σ_u [MPa]	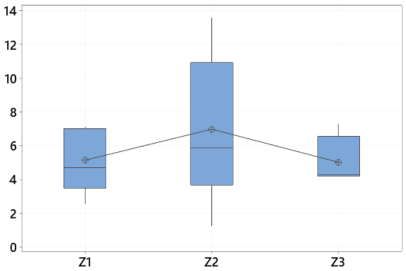	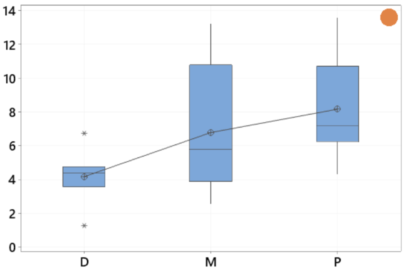
ε_u [%]	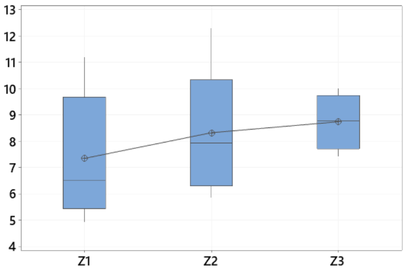	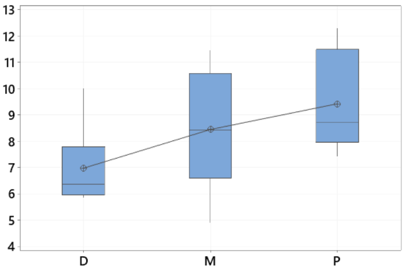

Table 3.6: Statistical comparison between femural zones and subzones in FH4.

FH4	Zones	Subzones
E [MPa]	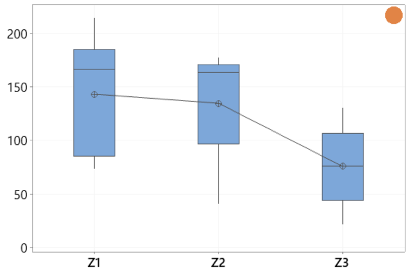	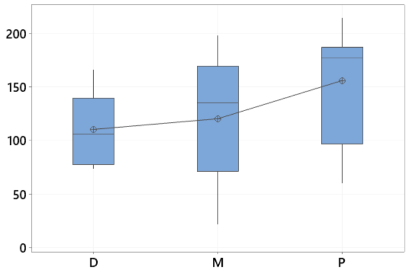
σ_y [MPa]	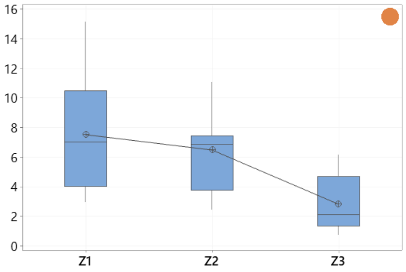	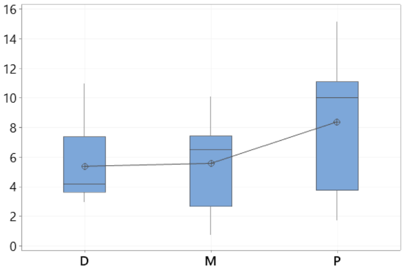
σ_u [MPa]	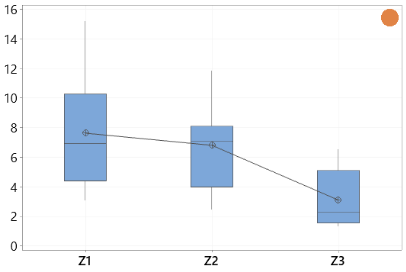	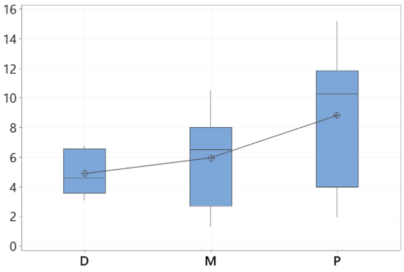
ε_u [%]	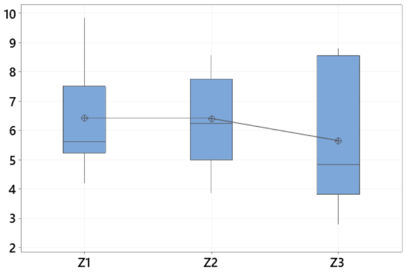	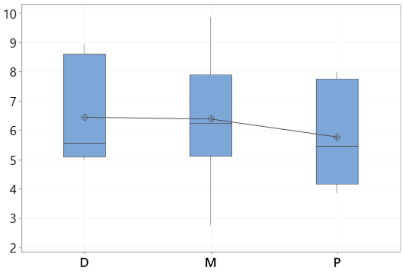

Table 3.7: Statistical comparison between femoral zones and subzones in FH5.

FH5	Zones	Subzones
E [MPa]	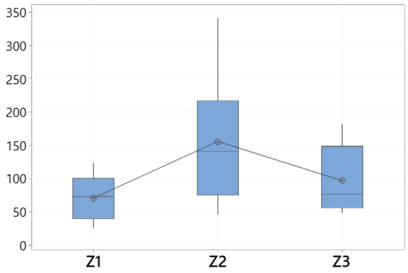	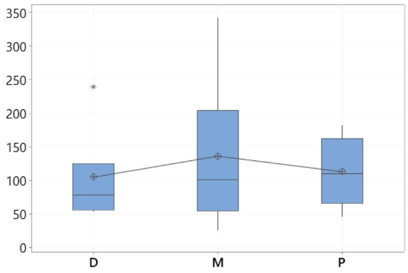
σ_y [MPa]	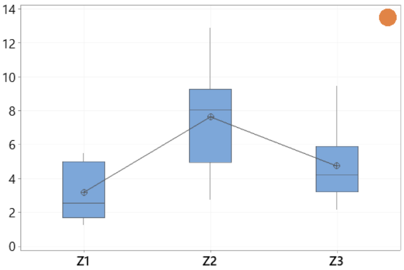	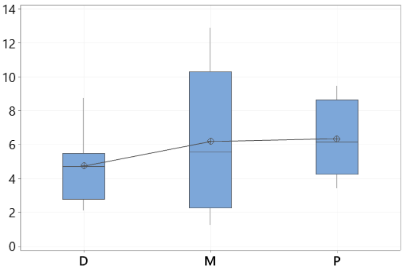
σ_u [MPa]	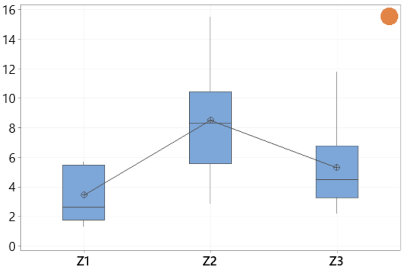	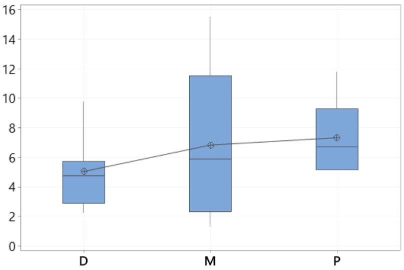
ε_u [%]	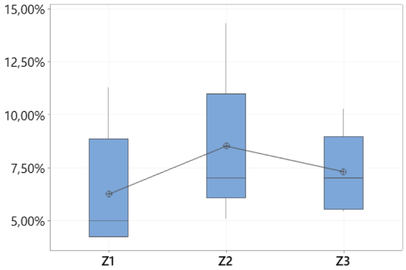	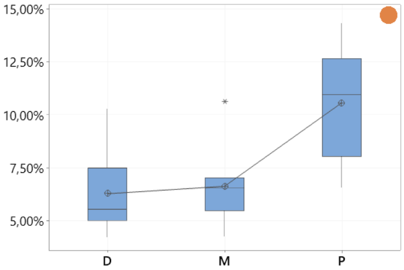

Table 3.8: Statistical comparison between femural zones and subzones in FH6.

FH6	Zones	Subzones
E [MPa]	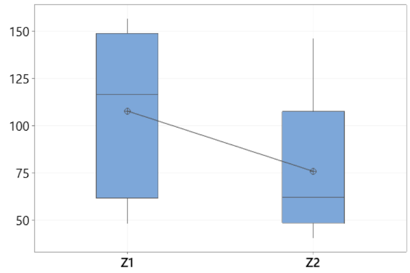	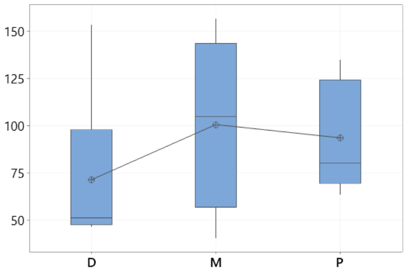
σ_y [MPa]	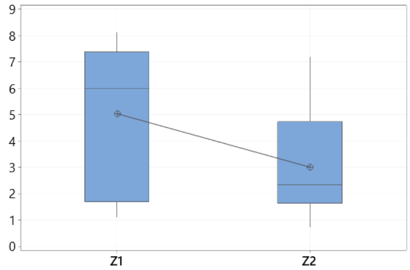	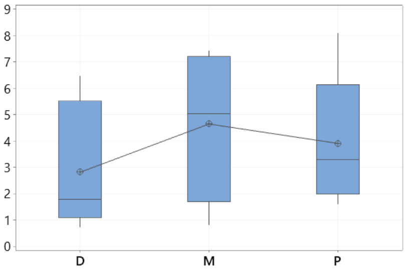
σ_u [MPa]	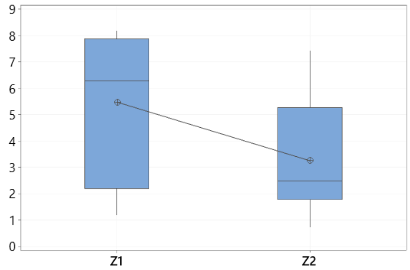	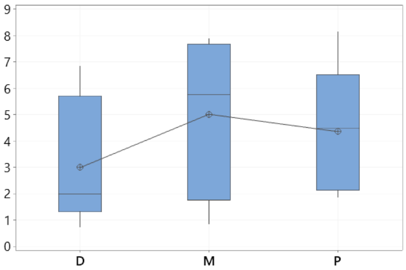
ε_u [%]	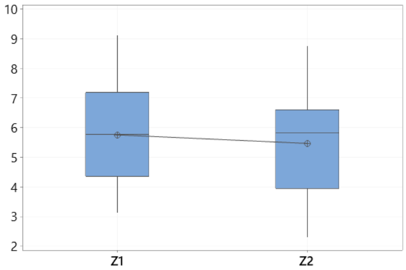	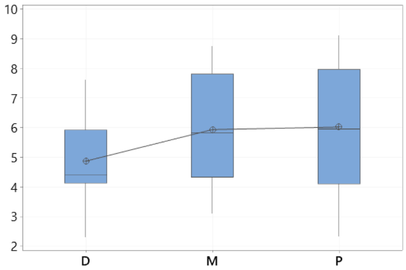

Table 3.9: Statistical comparison between femural zones and subzones in FH7.

FH7	Zones	Subzones
E [MPa]	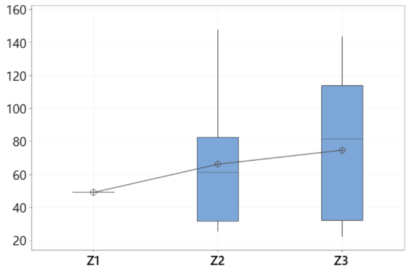	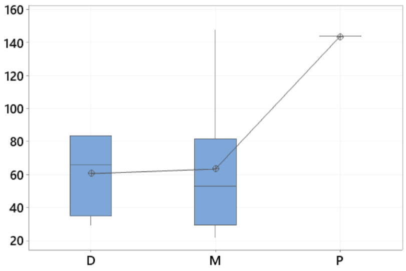
σ_y [MPa]	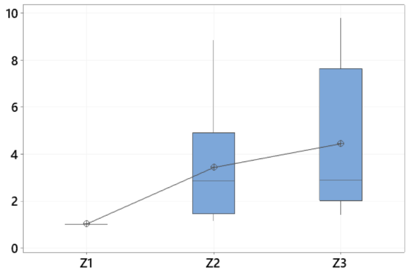	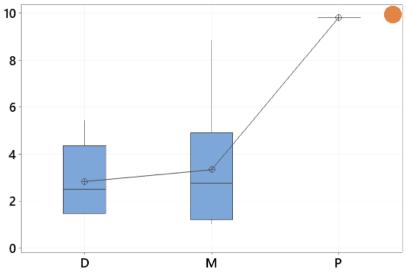
σ_u [MPa]	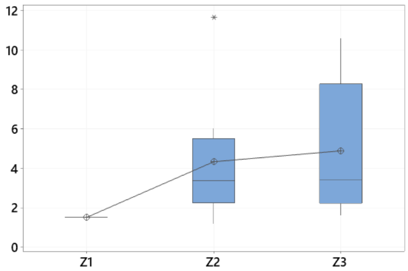	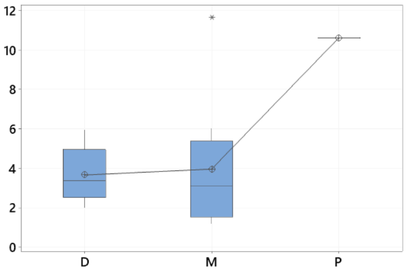
ε_u [%]	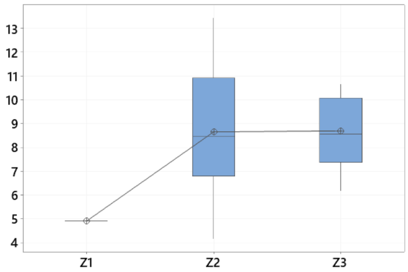	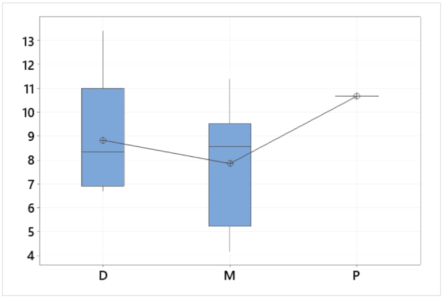

Table 3.10: Statistical comparison between femural zones and subzones in FH8.

FH8	Zones	Subzones
E [MPa]	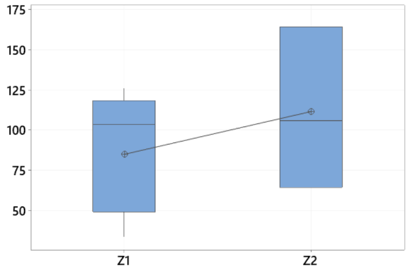	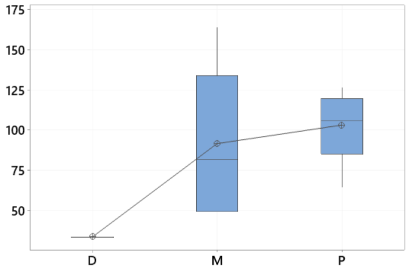
σ_y [MPa]	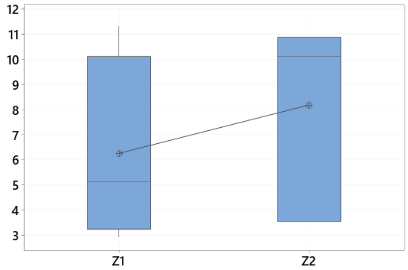	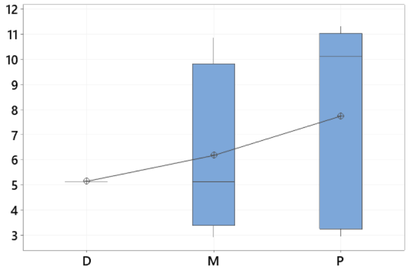
σ_u [MPa]	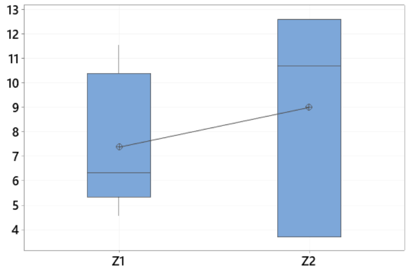	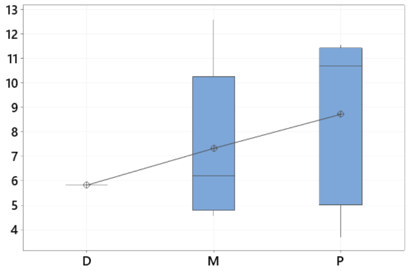
ε_u [%]	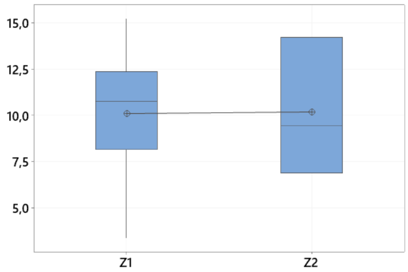	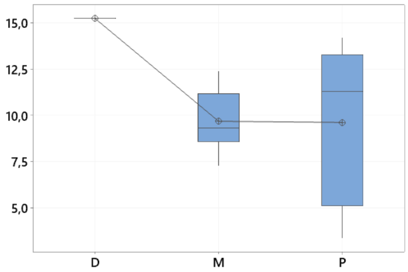

Table 3.11: Statistical comparison between non-osteoporotic and osteoporotic groups.

E [MPa]	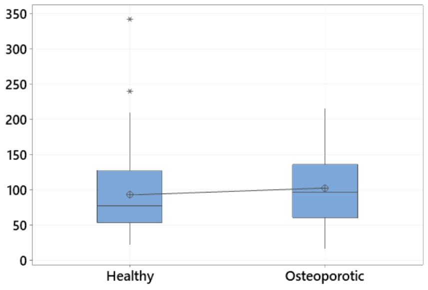
σ_y [MPa]	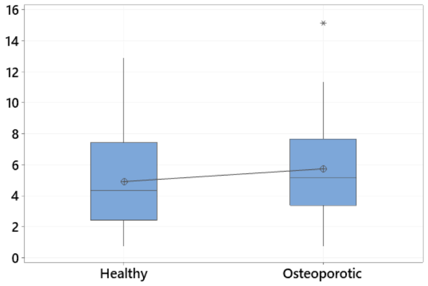
σ_u [MPa]	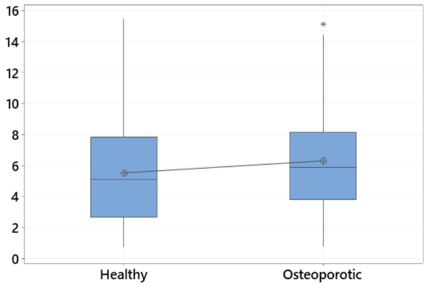
ε_u [%]	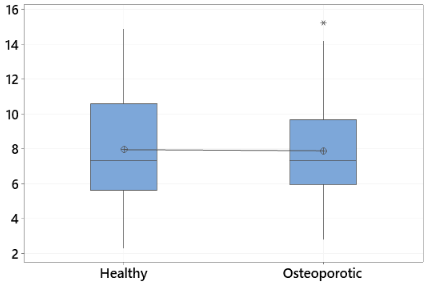

3.2 Tomographic analysis

Regarding the investigation of the synchrotron-based tomographic images, four specimens had been fully reconstructed and analyzed, following the time-consuming and computational-demanding process explained in Section 2.2.3. These four are namely sample 7 and sample 33 from the non-osteoporotic FH1 (FH1-S7) and FH5 (FH5-S33), sample 53 and sample 31 from the osteoporotic FH2 (FH2-S53) and FH4 (FH4-S31). Samples FH1-S7 and FH2-S53 were extracted from the Z1-M site of the two different femoral heads, while FH4-S31 and FH5-S33 belong to Z2-M sites. In this section are therefore reported the principal results about effective displacement check via radiographic analysis, comparisons between mechanical response inside and outside synchrotron, computational model outputs, crack history reconstruction, tridimensional crack visualization and the measurements of the main crack parameters, such as propagation velocity, COD and CTOD.

3.2.1 Radiographic validation

The different radiographs acquired at the ELETTRA Synchrotron in Trieste during the last IGFA campaign in October 2021, are stitched together with dedicated *Matlab* codes. With the purpose of verifying the initial assumption of non-deformation of the new 3D printed PLA endcaps and the effective displacement undergone by the unconstrained bone portion, measurements are taken through the software ImageJ.

As presented in Figure 3.2, the distance between the internal endcap's cavity and the internal cylinder's bottom remains almost constant during the compression test on both specimen's sides. This confirms the correctness of the initial assumption, where the endcaps were considered much stiffer than the bone specimens, allowing the imposed displacement to be entirely applied on the trabecular sample. Regarding the effective displacement undergone by the unconstrained bone's portion in each sample,

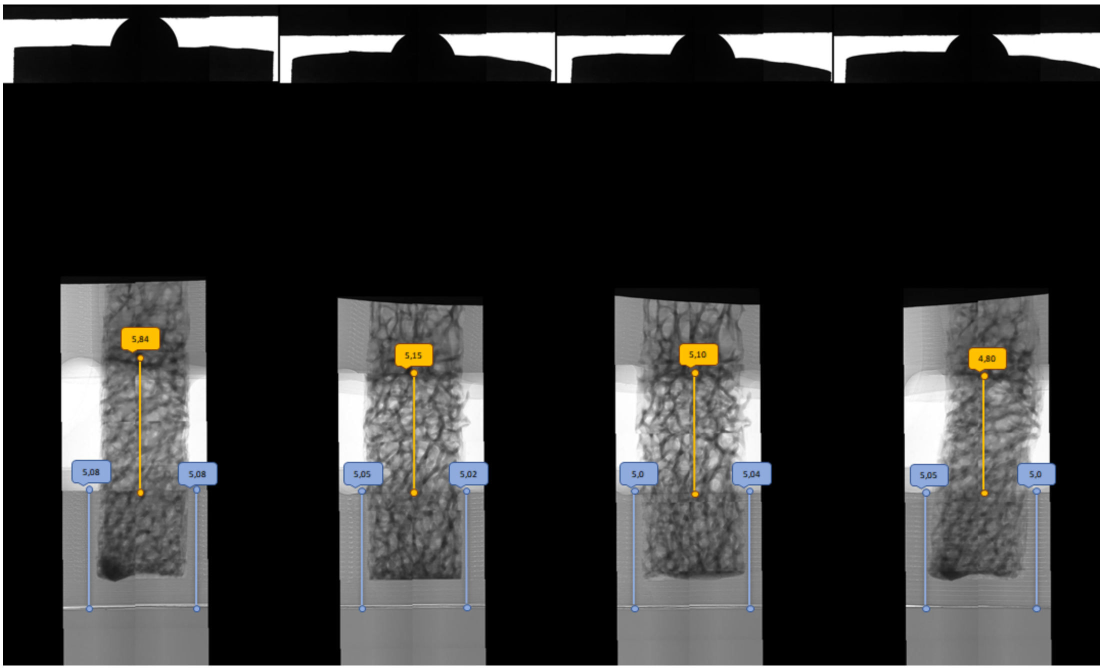

Figure 3.2: Stitching of the radiographies at the different acquisition steps. in blue are displayed measurements of PLA endcaps, while in orange of the unconstrained bone.

the effective length is evaluated at the different compression steps and compared to the displacement applied by the stepper motor during the October 2021 tests. At first they coincide, but then, as expected, being bone a heterogeneous material, the apparent compression of the unconstrained trabecular portion does not coincide with the imposed displacement. Therefore some portions of the specimens are more strained than others, due to buckling and local bendings, resulting in site-dependent measurement assessment.

3.2.2 Synchrotron-tests results validation

It is also important to compare the samples tested under synchrotron radiation with the ones previously tested outside, to check if the radiation has an important role in the degradation of mechanical properties and if the two groups are comparable. To do so, the output mechanical parameters of each synchrotron-tested sample have been compared with the corresponding ones tested at *Politecnico di Milano* Lab of the same femoral head. Afterwards, statistical analysis in *Minitab* was performed, with the exact same procedure discussed in Materials and Methods 2.1.3. For this comparison, all samples tested at Trieste during the various campaigns were considered, even the ones not reconstructed, to have a higher number of data. In the following Figure 3.3 are reported the final results.

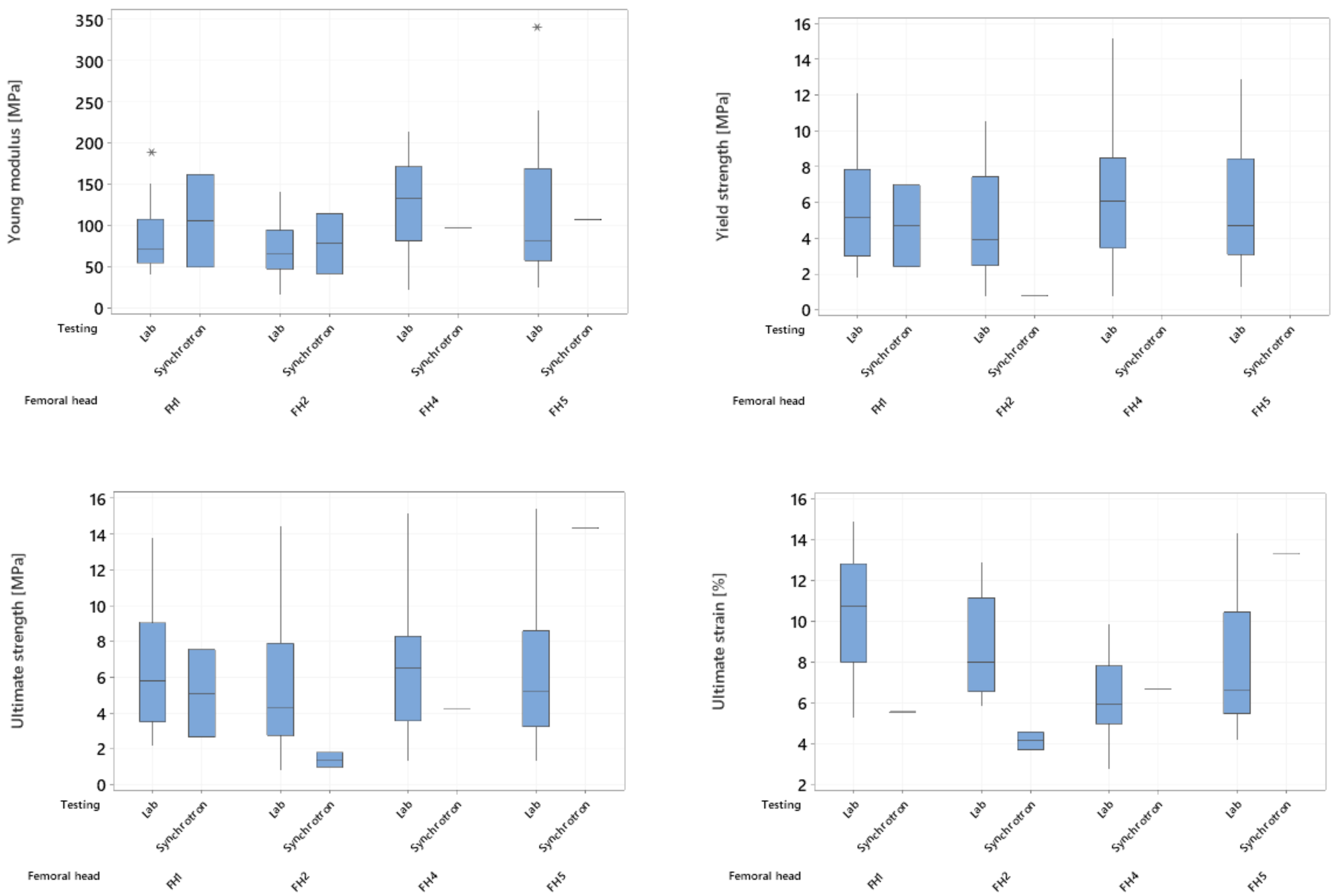

Figure 3.3: Comparisons of Young's modulus, Yield strength, Ultimate strength and Ultimate strain between samples tested at synchrotron and the corresponding tested at university.

3.2.3 Computational model

In the current section the outputs from the proposed computational model described in Section 2.2.4 are shown. As previously stated, computational analysis of the 3D model of the bone helps to better localise the most stressed zone, for this purpose the maximum principal stresses are obtained. The results of the displacement control test simulation are reported in Figure 3.4, in which is possible to define the most stressed zone, called failure band.

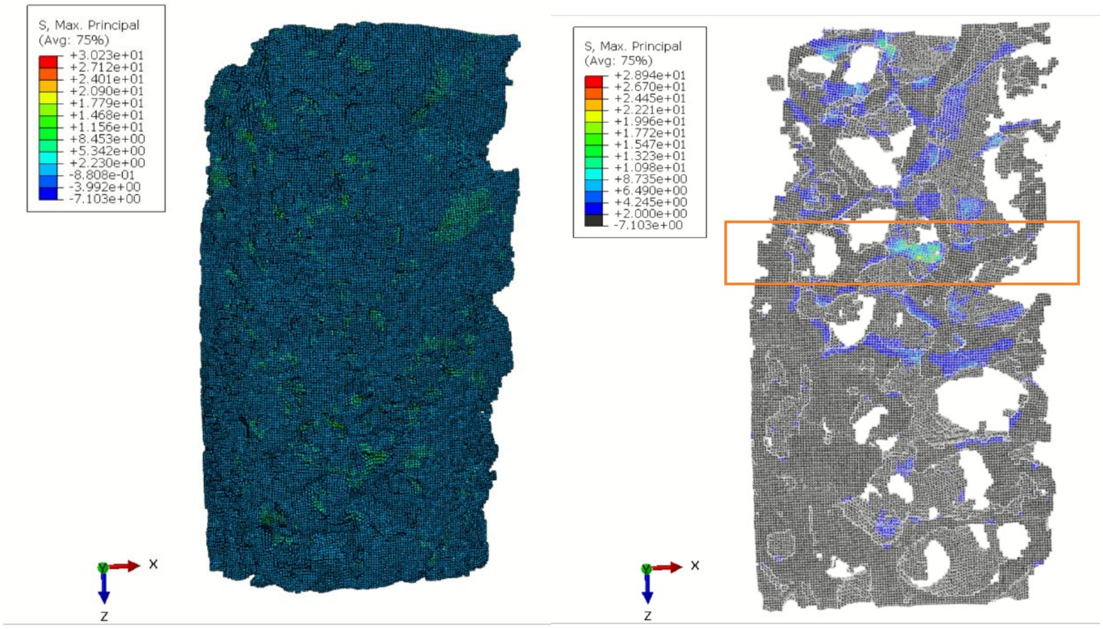

Figure 3.4: Output of the computational analysis on the FH5 sample. On the left the maximum principal stresses for the whole model, on the right a section that displays the failure band.

In Figure 3.5 are shown the force-time curves of the sample of interest, both for the experimental and computational model, that validate the obtained results. The experimental curve presents the four mechanical steps of 0.1 mm each, while the computational curve just shows a single step of 0.4 mm in a linear elastic regime. It is possible to have the actual confirmation that the model used is a good approximation to represent reality.

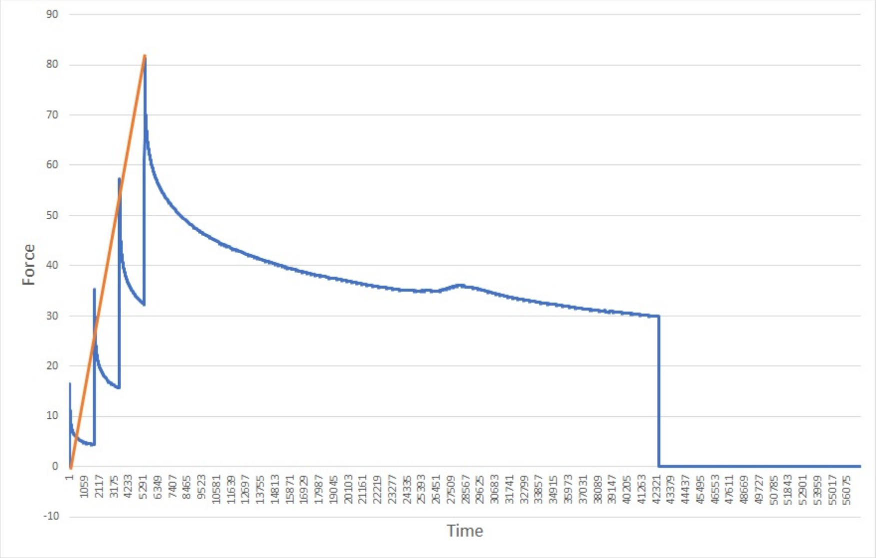

Figure 3.5: Force-time curves for the experimental test (in blue) and for the computational model (in red).

3.2.4 Crack history and visualization

Crack propagation history throughout the tomographic steps has been deeply investigated and here are reported three remarkable examples. Every crack behaves in a peculiar manner and it is greatly influenced by the local trabecular thickness and length, but also by the specific sample characteristics and testing conditions. As fully discussed in the next chapter, cracks are visible mostly from the second tomographic step, after the linear-elastic domain, even if in some cases (especially in zone H3) they are already present at the second scan.

In Figures 3.7 and 3.6 it can be noticed that the cancellous structure is still maintained even at the last tomographic step, while in Figure 3.8 there is an example of how it collapses after a huge number of compressions, with a complete separation of the trabeculae along the crack path.

Along with crack propagation path, also toughening mechanisms can be detected, in particular uncracked ligament bridging is present in numerous cracks encountered

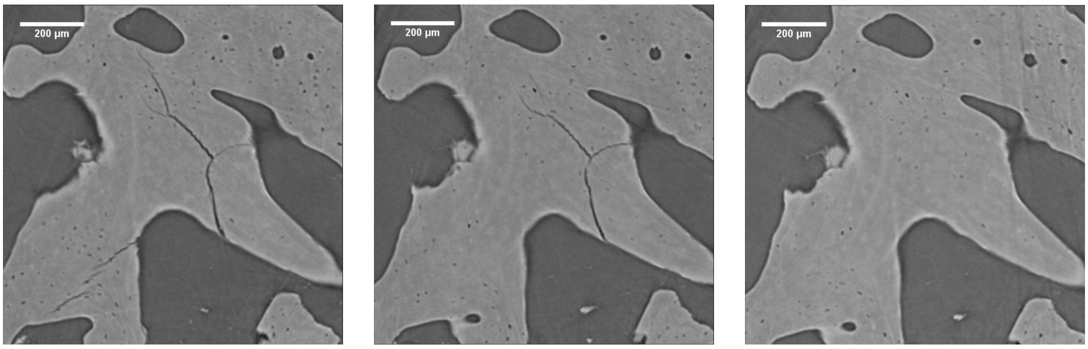

Figure 3.6: History of a crack found in FH5-S33 zone H3. From the left, tomographic STEP 3, STEP 2 and STEP 1-0.

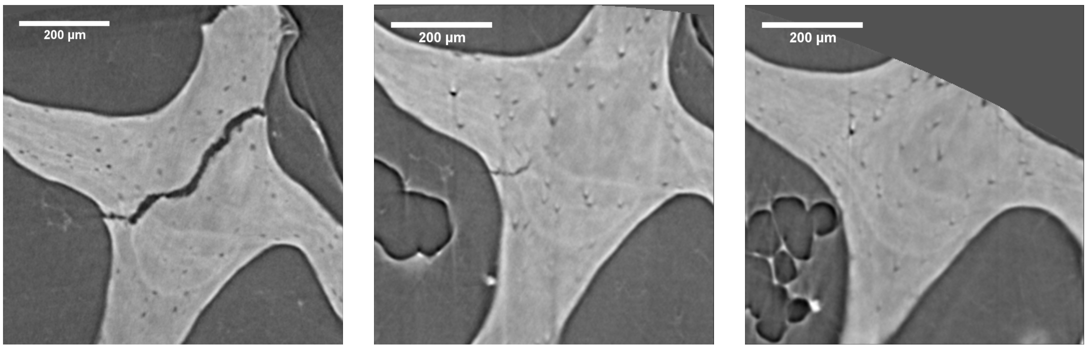

Figure 3.7: History of a crack found in FH4-S31 zone H0. From the left, tomographic STEP 3, STEP 2 and STEP 1-0.

(Figure 3.9). Crack does not develop in a linear continuous way, but it is segmented along parallel planes, appearing discontinuous and consuming more energy, thus slowing down propagation velocity [86].

The 3D representation of some cracks inside the bone was performed in order to show how they propagated in the space, having a more clear idea of where those cracks originated, also in relation to some features of the bone. In particular it is possible to observe in Figure 3.11 how the crack clearly originated from the surface of the trabecula, propagated through the bone and finally ended in a macro-pore, displaying a remarkable difference of length between the two loading steps. Moreover it has to be noticed how the second arm of the crack closed, probably caused by the

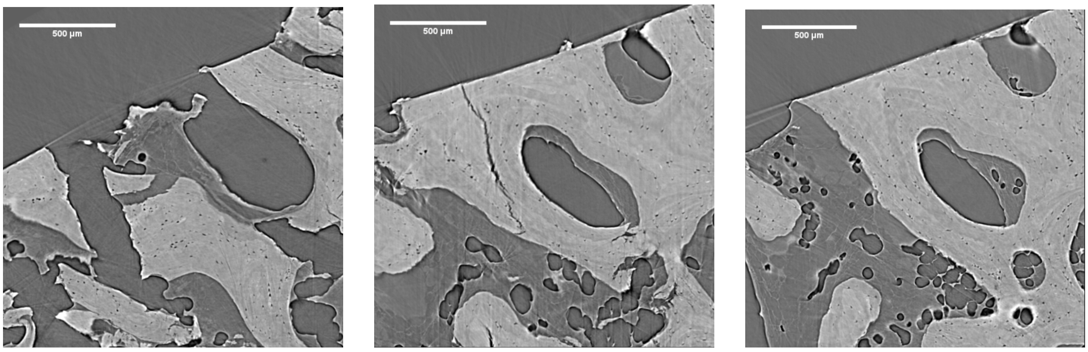

Figure 3.8: History of a crack found in FH1-S7 zone H3. From the left, tomographic STEP 3, STEP 2 and STEP 1-0. It is clear how at STEP 3 the trabecular pattern is completely destroyed.

complex distribution of stresses in that area.

Figure 3.10 enables us to observe even more how the crack changed between the two steps, with a strong increase of its length while spreading in two different directions, following the structure of the trabecula.

Another representation of interest is the one of the crack with the lacunar network, to better understand the relation between them. In the case analysed in Figure 3.12 it is not possible to say that, in general, the crack tends to propagate in a zone with a high lacunae density. Being the architecture in 3D very complex, with also the presence of some artefacts due to the reconstruction process, it is necessary to work in a bi-dimensional environment.

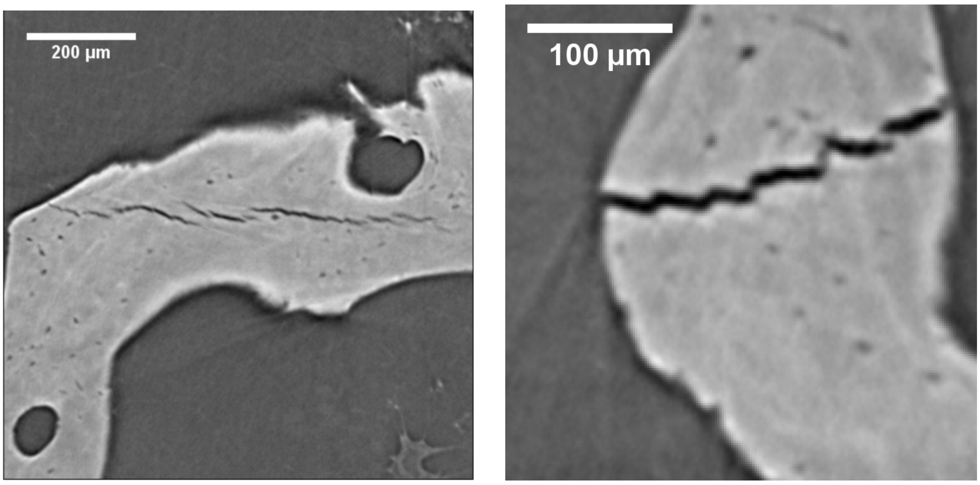

Figure 3.9: Ligament bridging mechanisms found in FH5-S33 zone H3 and FH4-S31 zone H0.

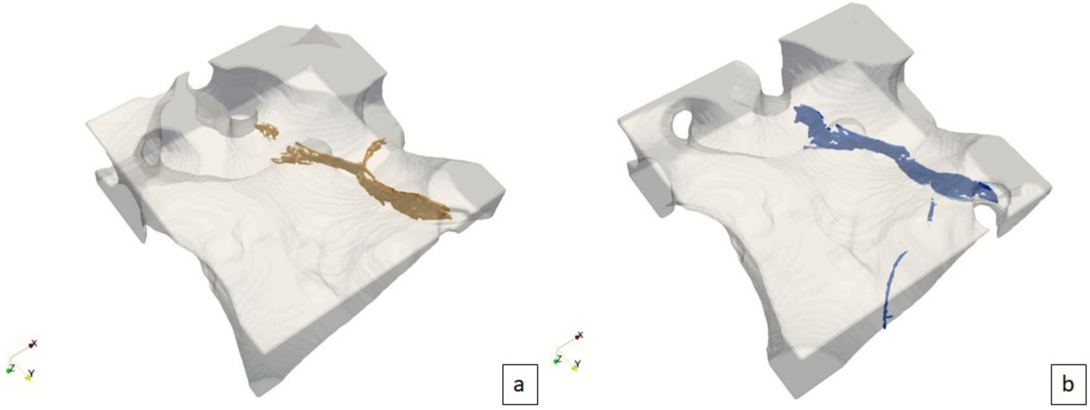

Figure 3.10: 3D visualization of a crack present in the sample FH5 at STEP 2 (a) and at STEP 3 (b).

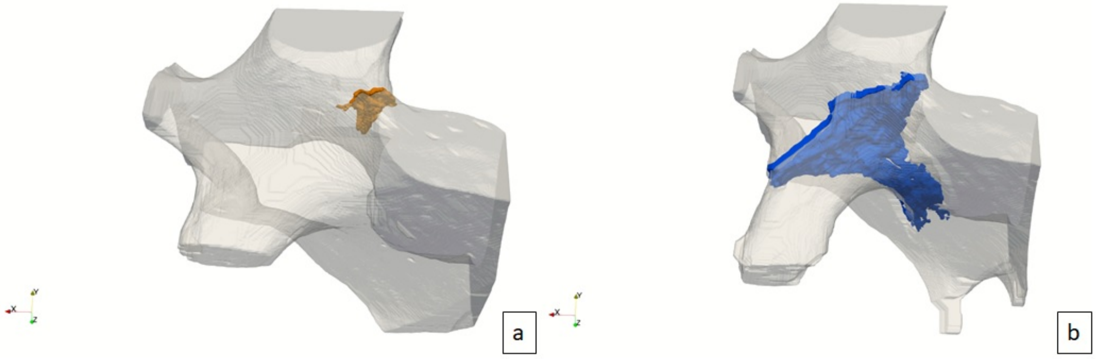

Figure 3.11: 3D visualization of a crack present in the sample FH4 at STEP 2 (a) and at STEP 3 (b).

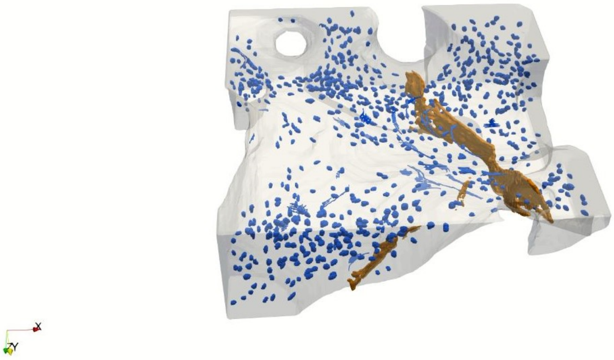

Figure 3.12: 3D visualization of a crack and lacunae present in the sample FH5 at STEP 3. It is possible to see artefacts.

3.2.5 Crack parameters

A deep quantitative study was impossible to perform on 3D visualisations, due to the complexity of the structure itself. Thus, disposing of high resolution SR-µCT images, it has been possible to measure the most relevant crack parameters directly on them, with the procedures explained in Section 2.2.3. Here are reported the results about crack propagation velocity, COD widening velocity and CTOD.

Crack propagation velocity

A number of 10 different cracks per sample has been considered in this study. Depending on the actual presence of the crack in some acquisition steps and the quality of the available reconstructed topographies, some measures may be taken between different steps, and it is specified in the relative graph caption.

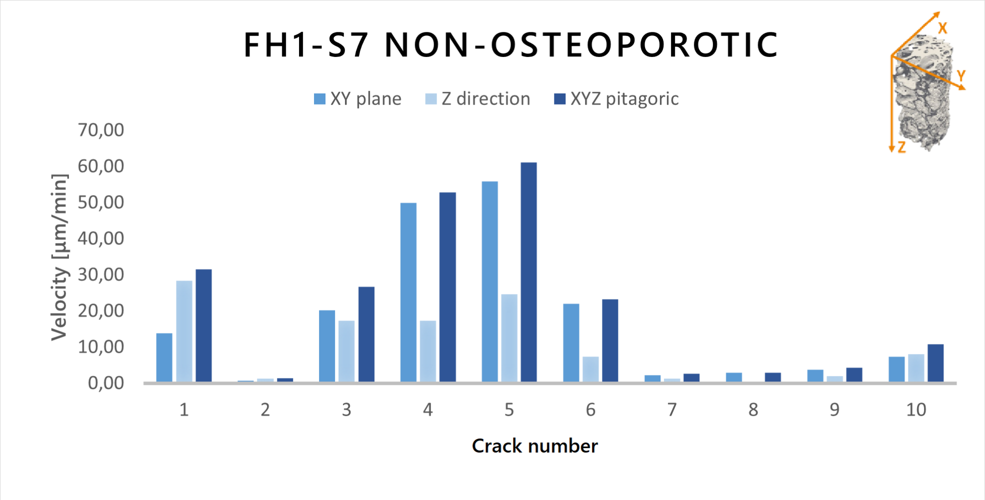

Figure 3.13: Propagation velocities of cracks in FH1-S7. All measures are taken between STEP 2-1.

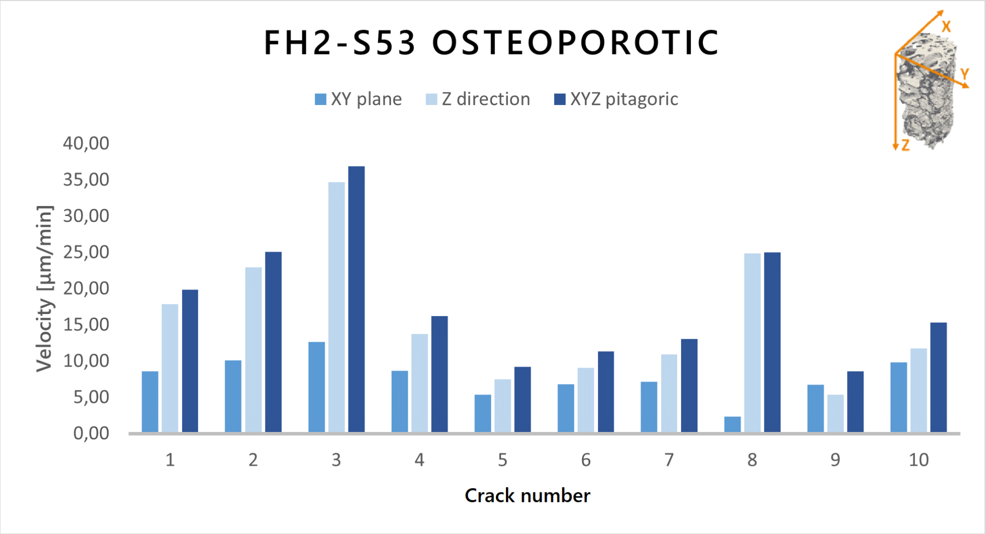

Figure 3.14: Propagation velocities of cracks in FH2-S53. All measures are taken between STEP 3-2, apart from cracks 8 and 9 which are between STEP 2-1.

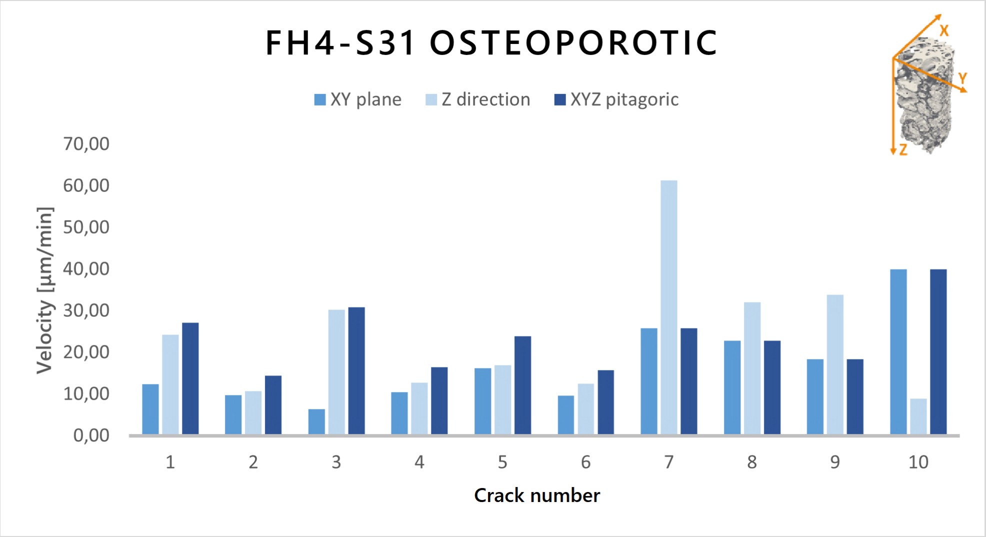

Figure 3.15: Propagation velocities of cracks in FH4-S31. For cracks 1 to 6 measures are taken between STEP 3-2, while for cracks 7 to 10 are between STEP 2-1.

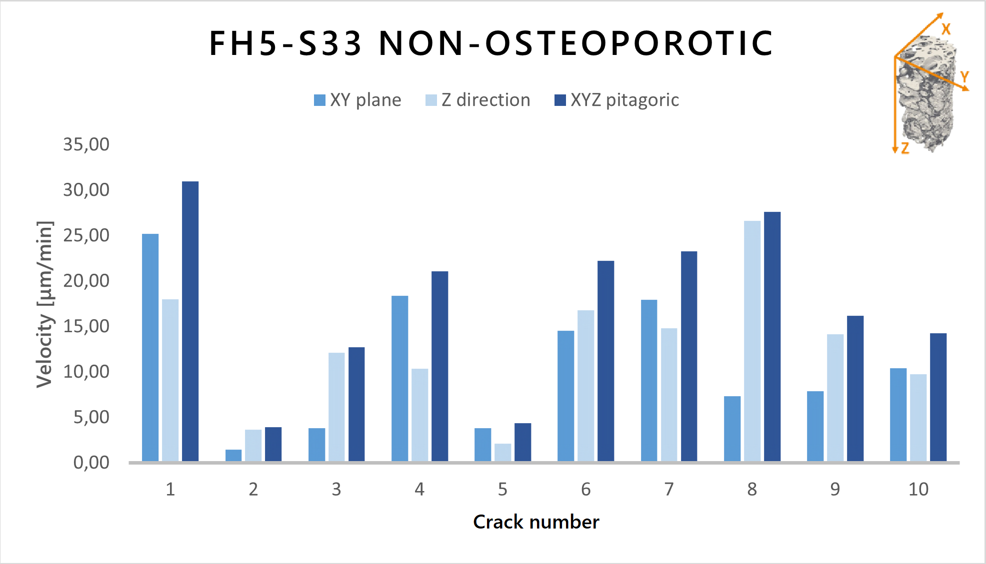

Figure 3.16: Propagation velocities of cracks in FH5-S33. All measures are taken between STEP 3-2.

Crack Opening Displacement

Regarding COD and also CTOD, 5 different cracks for each specimen has been considered. The majority of the cracks in the available slices cross completely the trabeculae, so it is difficult to spot non-crossing ones where to define a crack-tip.

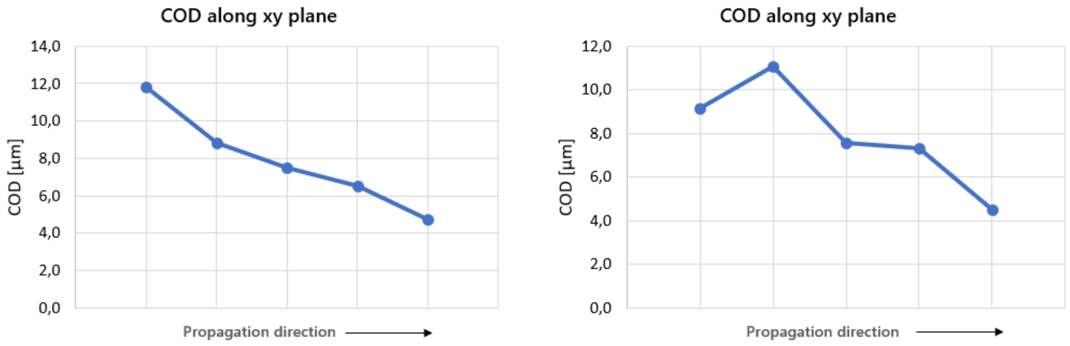

Figure 3.17: COD [µm] trend along the propagation direction on the XY-plane in FH5-S33. The two graphs are referred to the same crack, but in two different heights.

Due to the intrinsic mechanism of crack formation, they show an overall triangle-like shape that thins from the mouth to the tip. This trend is reflected clearly in Figure 3.17 that reports the COD values along the whole crack length. On the right graph is also possible to see that crack opening can locally enlarge; this is due to the presence of lacunar voids or toughening mechanisms such as the already discussed bridging, that alter the crack shape.

For each of the 5 cracks, also a COD widening velocity in µm/min has been calculated, in order to quantify the opening of the crack between two subsequent acquisitions. Being the COD an intrinsically variable quantity, for each crack approximately five measures have been taken both along the XY plane and along the Z direction, and an average value has been considered. Results are reported in Figure 3.18 and do not seem to show any specific trend. Negative values (noticeable in FH5-S33) mean that the crack underwent closing.

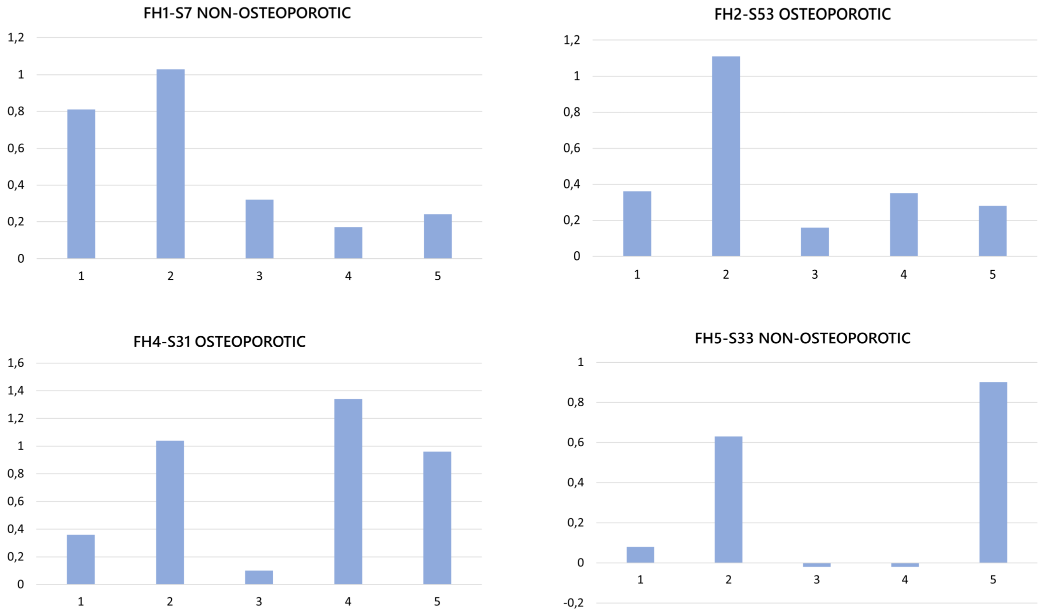

Figure 3.18: COD widening velocities [µm/min] for the four samples.

Crack Tip Opening Displacement

For the same cracks, also CTOD measures were performed. Also here, the presented values are an average between at least three measures taken on different heights, in order to have a more general and representative value. As explicate in Section 2.2.3 K_{CTOD} and K_I were calculated for every sample considering the mechanical parameters reported in Table 2.3. In the following tables are reported the results of these measurements, the values obtained considering the sample as non-porous are indicated with the superscript "sample", the ones obtained taking account of the porosity with the superscript "bone"; where possible, the same crack was considered in more acquisition steps. The values for the nominal stress were directly obtained from the experimental stress-strain curve and were not available for FH2-S53, for this reason it will not be considered.

Table 3.12: Measurements of K$_{CTOD}^{sample}$ K$_{CTOD}^{bone}$ and the CTOD used for the calculus.

Sample	# Crack	CTOD [µm]	STEP	K$_{CTOD}^{sample}$ [MPa$\sqrt{m}$]	K$_{CTOD}^{bone}$ [MPa$\sqrt{m}$]
FH1-S7	1	4.0	2	$6.72\cdot10^{-2}$	$2.24\cdot10^{-1}$
		4.2	1	$6.89\cdot10^{-2}$	$2.30\cdot10^{-1}$
	2	3.5	2	$6.29\cdot10^{-2}$	$2.10\cdot10^{-1}$
		3.7	1	$6.47\cdot10^{-2}$	$2.16\cdot10^{-1}$
	3	3.8	2	$6.55\cdot10^{-2}$	$2.18\cdot10^{-1}$
		3.8	1	$6.55\cdot10^{-2}$	$2.18\cdot10^{-1}$
	4	3.6	2	$6.38\cdot10^{-2}$	$2.13\cdot10^{-1}$
		3.4	1	$6.20\cdot10^{-2}$	$2.07\cdot10^{-1}$
	5	4.3	2	$6.97\cdot10^{-2}$	$2.32\cdot10^{-1}$
		4.2	1	$6.89\cdot10^{-2}$	$2.30\cdot10^{-1}$
FH2-S53	1	4.5	3	$6.15\cdot10^{-3}$	$3.07\cdot10^{-2}$
	2	3.6	3	$5.46\cdot10^{-3}$	$2.73\cdot10^{-2}$
	3	3.3	3	$5.26\cdot10^{-3}$	$2.63\cdot10^{-2}$
	4	3.0	3	$5.05\cdot10^{-3}$	$2.53\cdot10^{-2}$
	5	4.6	3	$6.22\cdot10^{-3}$	$3.11\cdot10^{-2}$
FH4-S31	1	3.7	2	$3.94\cdot10^{-2}$	$1.97\cdot10^{-1}$
	2	4.2	3	$4.20\cdot10^{-2}$	$2.10\cdot10^{-1}$
		5.4	2	$4.76\cdot10^{-2}$	$2.38\cdot10^{-1}$
	3	4.3	3	$4.25\cdot10^{-2}$	$2.12\cdot10^{-1}$
		5.0	2	$4.58\cdot10^{-2}$	$2.29\cdot10^{-1}$
	4	3.7	2	$3.94\cdot10^{-2}$	$1.97\cdot10^{-1}$
	5	4.0	2	$4.10\cdot10^{-2}$	$2.05\cdot10^{-1}$
FH5-S33	1	3.7	3	$5.84\cdot10^{-2}$	$1.95\cdot10^{-1}$
		3.8	2	$5.92\cdot10^{-2}$	$1.97\cdot10^{-1}$
	2	3.8	3	$5.93\cdot10^{-2}$	$1.98\cdot10^{-1}$
	3	4.6	3	$6.56\cdot10^{-2}$	$2.19\cdot10^{-1}$
		3.9	2	$6.04\cdot10^{-2}$	$2.01\cdot10^{-1}$
	4	1.4	3	$3.64\cdot10^{-2}$	$1.21\cdot10^{-1}$
		1.8	2	$4.12\cdot10^{-2}$	$1.37\cdot10^{-1}$
	5	2.1	3	$4.39\cdot10^{-2}$	$1.46\cdot10^{-1}$

Table 3.13: Measurements of K$_I^{sample}$ K$_I^{bone}$, and the corresponding σ_n^{sample} σ_n^{bone} used for the calculi.

Sample	# Crack	σ_n^{sample} [MPa]	σ_n^{bone} [MPa]	STEP	K$_I^{sample}$ [MPa$\sqrt{m}$]	K$_I^{bone}$ [MPa$\sqrt{m}$]
FH1-S7	1	5.4	18.0	2	$1.71\cdot10^{-1}$	$5.71\cdot10^{-1}$
		6.9	23.0	1	$2.09\cdot10^{-1}$	$6.97\cdot10^{-1}$
	2	5.4	18.0	2	$2.31\cdot10^{-1}$	$7.69\cdot10^{-1}$
		6.9	23.0	1	$2.28\cdot10^{-1}$	$7.61\cdot10^{-1}$
	3	5.4	18.0	2	$3.11\cdot10^{-1}$	1.04
		6.9	23.0	1	$2.11\cdot10^{-1}$	$7.05\cdot10^{-1}$
	4	5.4	18.0	2	$1.54\cdot10^{-1}$	$5.13\cdot10^{-1}$
		6.9	23.0	1	$1.81\cdot10^{-1}$	$6.05\cdot10^{-1}$
	5	5.4	18.0	2	$1.66\cdot10^{-1}$	$5.54\cdot10^{-1}$
		6.9	23.0	1	$1.89\cdot10^{-1}$	$6.31\cdot10^{-1}$
FH4-S31	1	4.4	22.0	2	$1.00\cdot10^{-1}$	$5.02\cdot10^{-1}$
	2	6.0	29,9	3	$2.87\cdot10^{-1}$	1.43
		4.4	22.0	2	$1.19\cdot10^{-1}$	$5.93\cdot10^{-1}$
	3	6.0	29,9	3	$1.65\cdot10^{-1}$	$8.23\cdot10^{-1}$
		4.4	22.0	2	$1.21\cdot10^{-1}$	$6.06\cdot10^{-1}$
	4	6.0	29,9	3	$1.61\cdot10^{-1}$	$8.03\cdot10^{-1}$
	5	6.0	29,9	3	$1.28\cdot10^{-1}$	$6.40\cdot10^{-1}$
FH5-S33	1	7.8	26.0	3	$4.02\cdot10^{-1}$	1.34
		9.6	32.1	2	$4.70\cdot10^{-1}$	1.57
	2	7.8	26.0	3	$3.27\cdot10^{-1}$	1.09
	3	7.8	26.0	3	$3.97\cdot10^{-1}$	1.30
		9.6	32.0	2	$4.21\cdot10^{-1}$	1.40
	4	7.8	26.0	3	$3.15\cdot10^{-1}$	1.05
		9.6	32.1	2	$3.53\cdot10^{-1}$	1.18
	5	7.8	26.0	3	$3.51\cdot10^{-1}$	1.17

Chapter 4

Discussion

4.1 Mechanical properties comparisons

The results presented in Section 3.1.2 reflect the complex mechanobiology of the proximal femur's architecture. Furthermore, intra-patient variability is deeply explored, comparing the Young's modulus in the different femoral heads, in Z1, Z2, Z3 zones and P, M, D sub-regions.

For what concerns the comparison of the Young's modulus for the different femoral head, since the inter-patients variability is very high (Figure 4.1), it has been decided to use a normalized Young's modulus (E/Emax), which is more representative of the real situation. In fact, normalizing the Young's modulus with respect to the maximum value detected in each femoral head allows neglecting intrinsic variations linked to the donor age range or additional alterations in the femoral head morphology that are not linked to the osteoporotic condition and could be considered out of the purpose of this work.

A great variability of the results can be noticed in Figure 4.2, even more pronounced for the osteoporotic samples. Some borderline cases could be detected, with FH3, FH4, FH6 and FH8 displaying higher normalized modulus values when compared

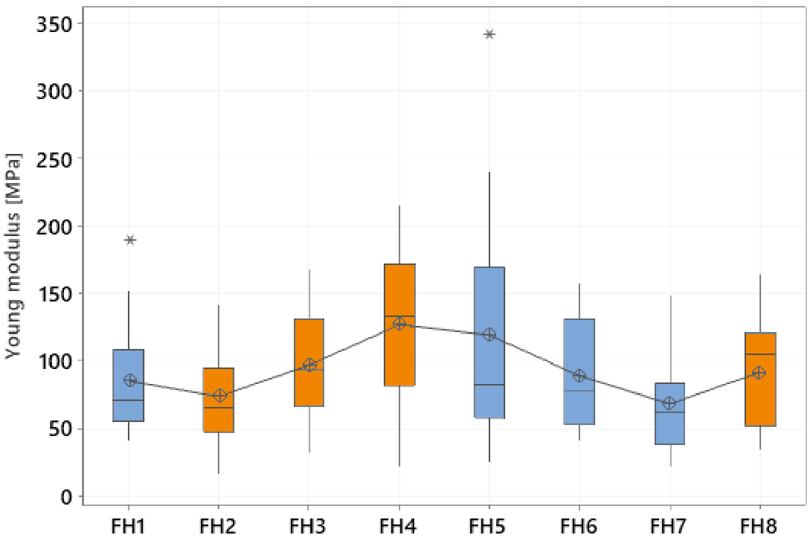

Figure 4.1: Statistical comparison for the Young's modulus between all eight femoral heads. In blue non-OP samples, in orange OP samples.

with osteoporotic FH2 and even in comparison with the non-osteoporotic FH1, FH5 and FH7 cases. Indeed, FH3, FH6 and FH8 presented also local arthritic regions, while FH4 was affected by a thickening of the cortical region in contact with the acetabulum, while showing an overall osteoporotic condition. On the other hand, sample FH5 presents lower values when compared with the others, which may be caused by the fact that the sample was actually osteopenic. Also FH7 was diagnosed with osteopenia, in fact shows values closer to FH5 ones. These considerations are particularly interesting and highlight once more the capability of the experimental protocol and the designed MCD to capture local variations in terms of the mechanical properties.

For the analysis of zones and subzones only the normalized Young's modulus graph is reported, since the yield strength, ultimate strength and ultimate strain have similar trends. The behaviour of these trends is comforting since they follow the normal anatomic conformation and load distribution in the femur. Indeed, higher values for

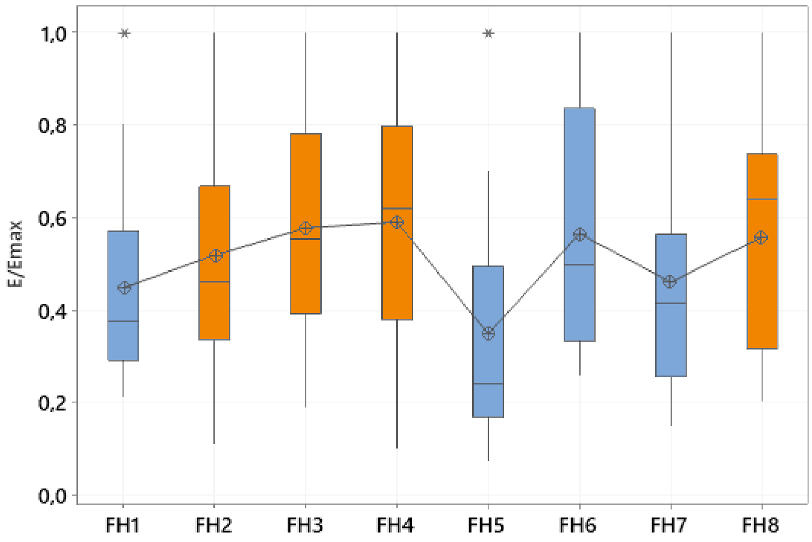

Figure 4.2: Statistical comparison for the normalized Young's modulus between all eight femoral heads. In blue non-OP samples, in orange OP samples.

Z2 and Z1 are displayed (Figure 4.3), since a higher portion of the load is sustained by the central Z2 region and secondly by the frontal Z1 zone, where a large number of intersections between the principal tensile and compressive groups of fiber occur. The repartition in sub-zones allows to better capture the intra-subject variation in the stress trajectories; the proximal region of all the eight analyzed femoral heads shows better mechanical properties (Figure 4.4) followed by the medial and eventually the distal region. In the proximal sub-zone the principal compressive group is predominant, directly sustaining the loads transmitted from the acetabulum. At last, it is interesting to notice that these trends remain unchanged despite the different pathologies and borderline cases, meaning that the transmission of the physiological loads inside bone does not change.

In order to better consider the differences between osteoporotic and non-osteoporotic bone a specific analysis was conducted and reported in (Table 3.11). In this case a significant statistical difference cannot be detected between OP and non-OP samples,

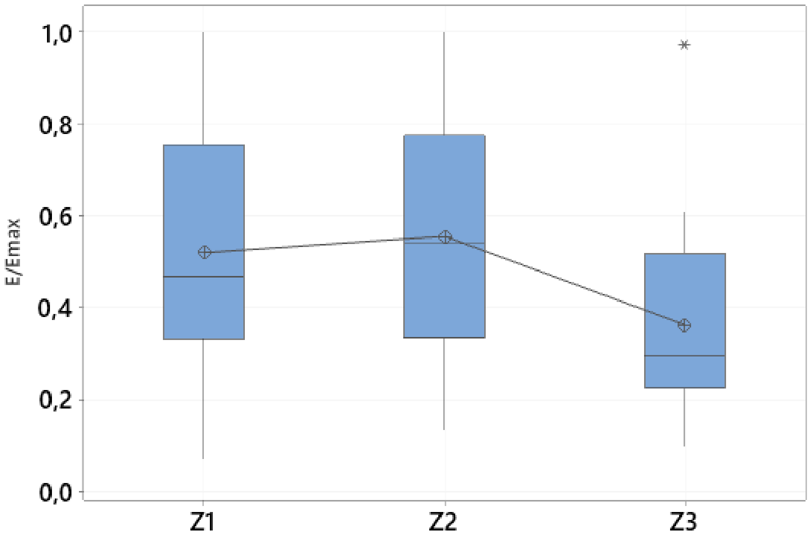

Figure 4.3: Statistical comparison for the normalized Young's modulus between Z1, Z2 and Z3 zones for the eight femoral heads.

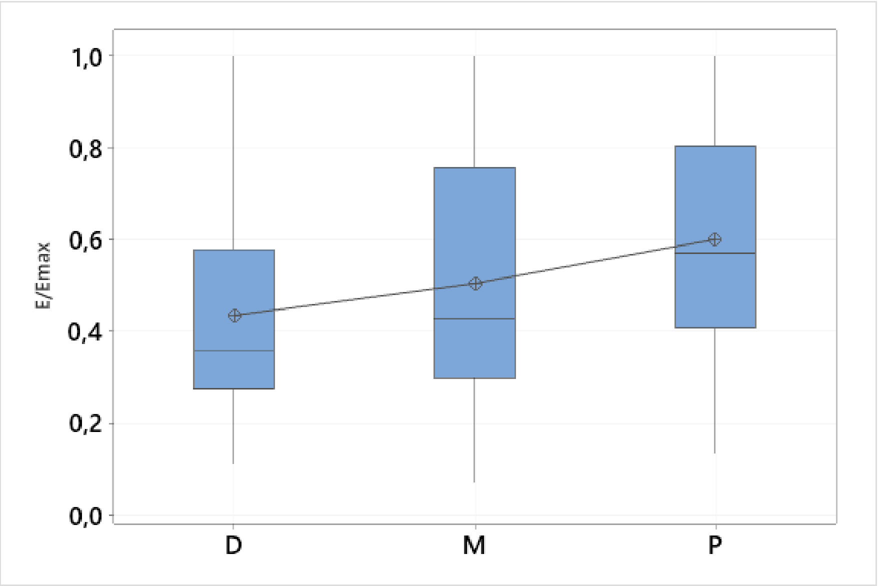

Figure 4.4: Statistical comparison for the normalized Young's modulus between M, P and D subzones for the eight femoral heads.

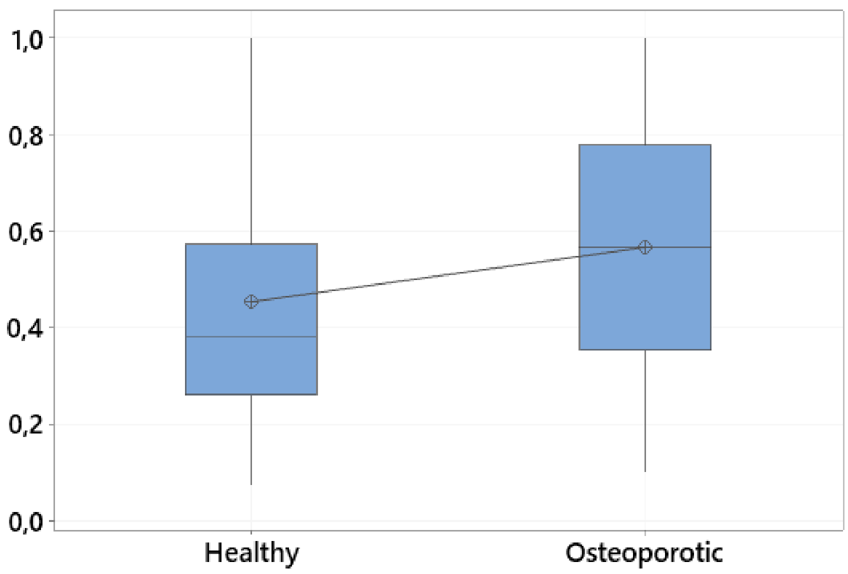

Figure 4.5: Statistical comparison for the normalized Young's modulus between osteoporotic and non-osteoporotic samples.

except for the case of the normalized Young's modulus (Figure 4.5), probably caused by the presence of many borderline cases already mentioned before. An opposite trend is shown by the ultimate strain, where it is slightly lower in the case of osteoporotic groups. Moreover, a great variability of the results can always be detected.

In the end, comparing our work with the main results reported in the literature, our values of the apparent Young Modulus are placed in the lower range of those mentioned before [2, 45, 68, 69], even if they present high variability (Figure 4.6). As already stated, several factors affect the micro-compression outcomes, such as geometry, dimensions (we use thin parallelepiped-shaped specimens), end supports and cross-head speed and bone quality, making their direct comparison slightly uncertain.

On the other hand, considering only samples with bone diseases, our results are still in the lower range, but much closer to the results of other studies (Figure 4.7 & 4.8). In particular, OP samples have values of Young's modulus similar to *Chun Li et al.* [46] and *Li et al.*'s works [45], while OA samples are perfectly aligned with *Chun*

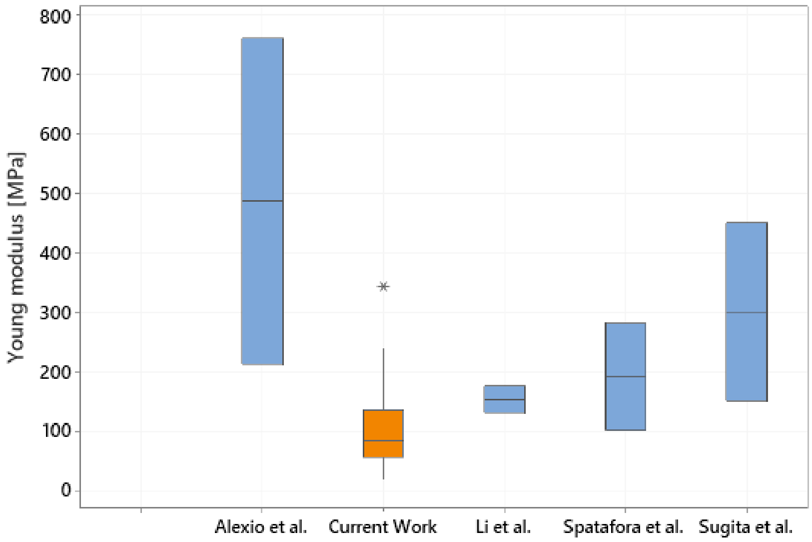

Figure 4.6: Young's modulus comparisons between our whole work and the principal results found in literature.

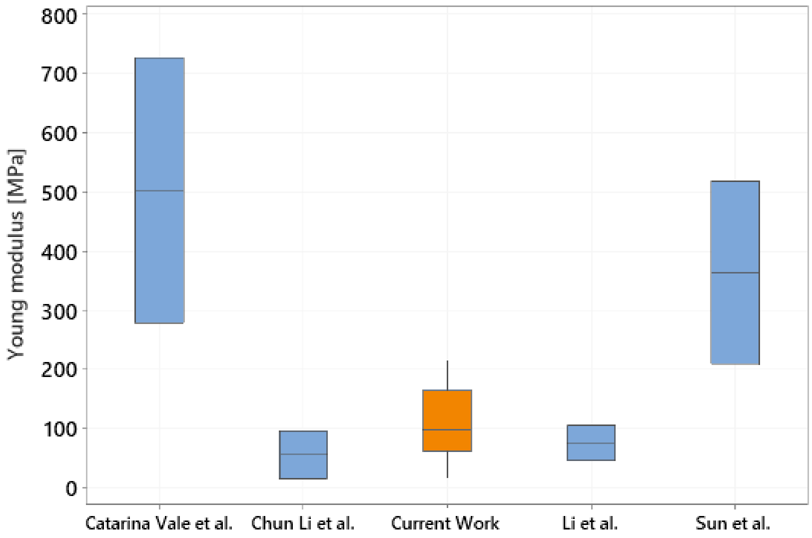

Figure 4.7: Young's modulus comparisons between our work and the principal results found in literature regarding OP samples.

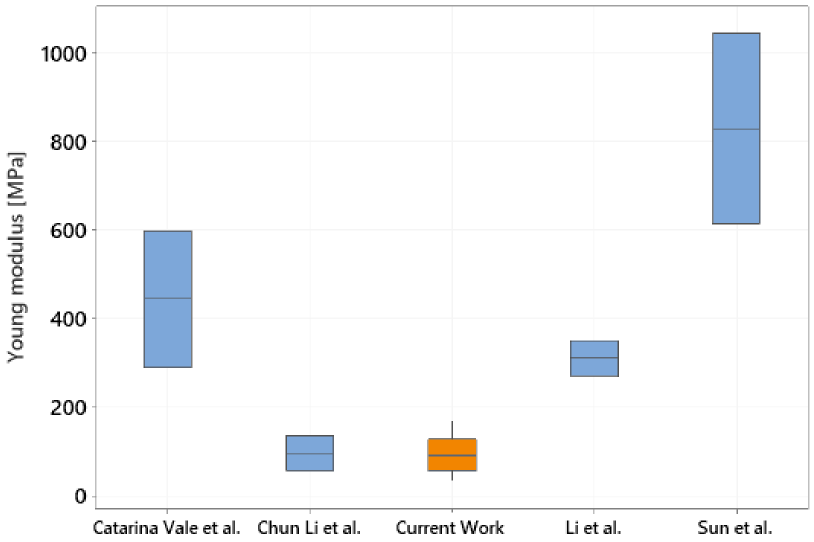

Figure 4.8: Young's modulus comparisons between our work and the principal results found in literature regarding OA samples.

Li et al.'s results [46].

4.1.1 Synchrotron Vs laboratory comparisons

As it is possible to see in boxplots of Figure 3.3, there's not a unique and homogeneous trend in the change of properties in the irradiated samples, but scattered values that are peculiar for each sample:

- Young's Modulus does not show any sign of changes, but all values fall inside the respective reference interval. It is an encouraging result since it is our main mechanical parameter.
- regarding Yield strength, only for synchrotron-samples belonging to FH1 and FH2 were available these parameters: the former is in line with the other samples, while the latter shows a significative ($p<0.05$) decrease.
- the ultimate strength shows significative differences ($p<0.05$) only for samples

of FH2 (OP) and FH5 (non-OP), but they have opposite trends.

- similar situation for the ultimate strain, where 2 groups (FH1 and FH2) show a significative ($p<0.05$) decay, while FH4 is in line and FH5 shows an increased value.

In conclusion we could state that the properties are strongly sample-dependent even in the case of high-energy radiation, so to draw a more precise trend it would be necessary a much huge number of synchrotron-tested samples to include in the analysis. By now, it seems that radiation does not affect significantly and with a unique clear trend the mechanical properties, especially in terms of Young's modulus, so our results are comparable with the observations done during laboratory tests.

4.2 Computational model and cracks

First of all it is possible to observe in Figure 2.14 that the most stressed region corresponds to a BV/TV which is lower than the average, so a region with a high percentage of voids. This correspondence has been also found in other similar studies [54].

As already stated in the previous chapters, the processing of the images is complex, hence, the model greatly helps to identify at priori where the cracks would form. In fact, the most stressed region highlighted by the computation analysis corresponds to a broken trabecula visible in the tomographic images (Figure 4.9). The trabecula is mainly undergoing a compressive load, indeed *Nagaraja et al.* [52] suggested that actually, inside the micro architecture, the effect of the compressive load in the single trabecula is crucial for the damage initiation. Therefore, after this trabecula fails, a domino effect is unchained leading to the failure of the complete structure.

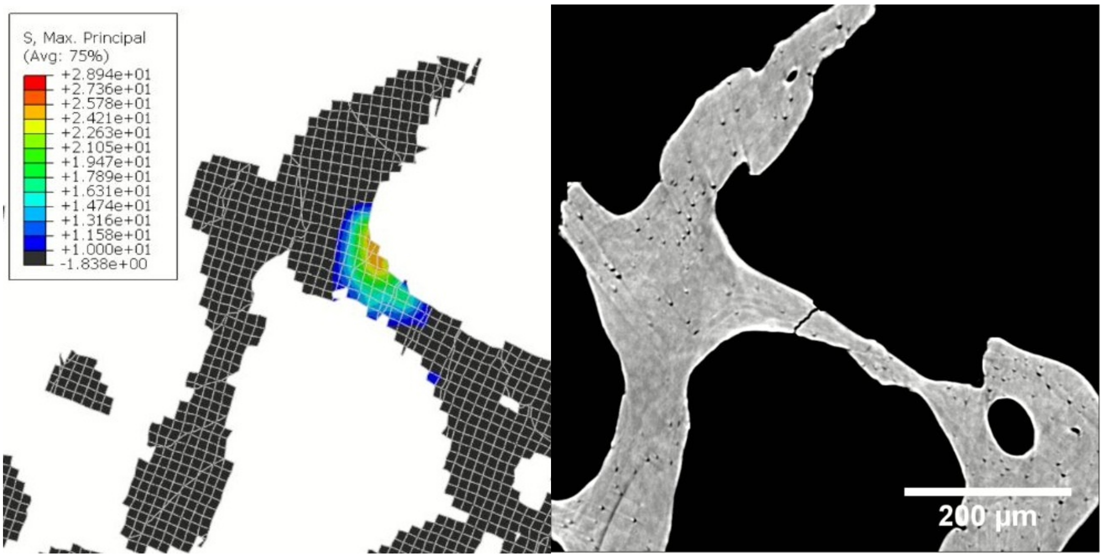

Figure 4.9: Most stressed region of the computational model (on the left), corresponding to a cracked trabecula (on the right) at STEP 1.

4.3 Crack features comparisons

Reconstructing the propagation history of cracks along the different acquisition steps is a time-demanding procedure and can be sometimes really hard due to intrinsic factors. The biggest obstacle is the image reconstruction itself; finding the right parameters and values for the process explained in Section 2.2.3 requires experience and specific skills, and, above all, the computation itself is elaborated and memory-demanding. Moreover also a clean and firm acquisition setup is needed, in order to minimize eventual misalignment and background noise. The second major issue is the level of damage of the trabecular pattern: it happens in fact that the acquisitions of STEP 3, especially in H3 zone, shows a complete destructed bone (Figure 4.10), making it impossible to recognize the corresponding situation in the previous step.

After zone H3, the most damaged zone is the inferior part of H0. On the other hand, zone H6, the lower one, is the less damaged, and in some cases does not even show the presence of cracks after all the compressive steps. This aspect is

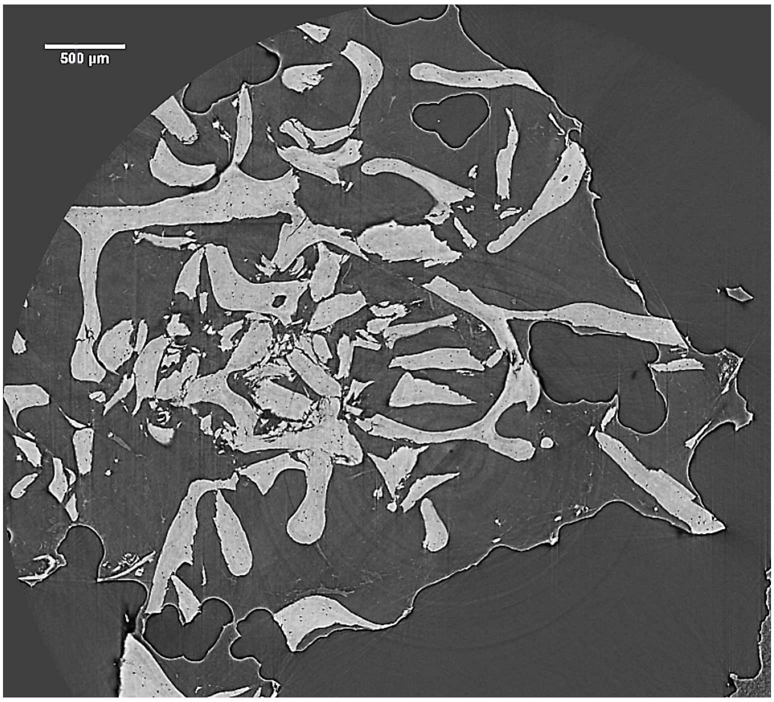

Figure 4.10: Collapsed trabecular pattern in FH4-S31 zone H3 STEP 3.

in complete accordance with the experimental evidence: the tested bone specimens often collapse and break into two parts in the middle, so here is expected a complete disgregation of the cancellous network. The middle region is where the distance from the endcaps is higher and also it is more probable to have buckling phenomena. Moreover, the fact that the lower region is less damaged, means that the deformation is not homogeneously transferred along the specimen length, due to the peculiar cellular structure of bone.

An important and highly investigated aspect is crack origin and its relationship with lacunae. We observed different behaviours, which are not univocal, but seem to be highly site and specimen-dependent and found examples for each of the main theories stated in the literature. Lacunae could act as stress concentrators [80], and, especially when they are close to a border, they could originate a crack as visible in Figure 4.11. Nevertheless, this behaviour has been observed only in very few

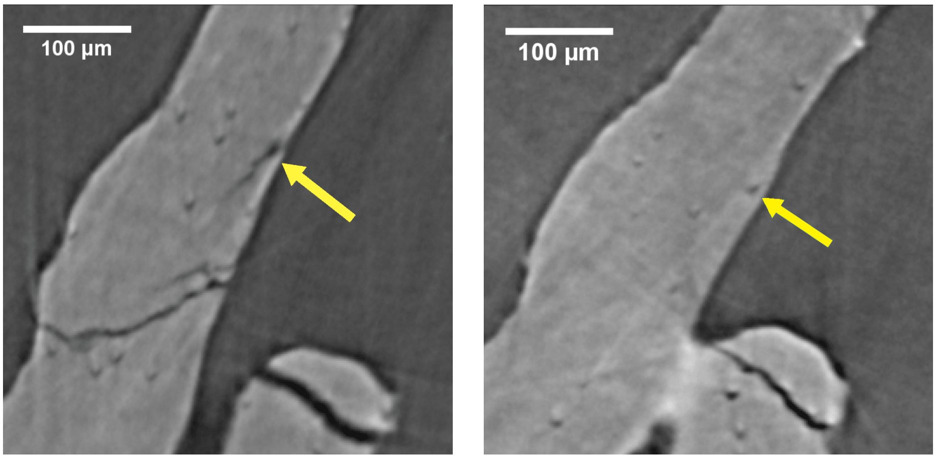

Figure 4.11: Crack originated from a lacuna near the border (yellow arrow) in FH5-S33 zone H3.

cracks, especially due to the difficulty in finding the precise correspondence between slices. In the majority of cases it is possible to notice that cracks tend to appear near sharp trabecular bends, macro-porosities, and surface discontinuities. Moreover, in numerous cracks, another peculiar aspect regards the presence of interfaces and different mineralization lines. As depicted in Figure 4.12 these zones have a crucial role both in crack initiation, due to the higher brittle mineral content, but also guide its propagation along them, offering a preferential pathway.

In addition to fracture initiation, also its propagation and interaction with lacunae has been investigated. Even in this case, there is not a unique trend, but a prism of different possibilities (Figure 4.13) depending on the crack examined.

As we can see, it is often possible to find opposite mechanisms and interactions; in Figure 4.13a we can see that a lacuna acts as a pinpoint, stopping crack propagation. This is another toughening mechanism reported in the literature, where lacunae become the crack tip, thus lowering the stress intensification due to their higher diameter. But this is not very common in our analysis, in Figure 4.13d, as an example, even a big and transverse lacuna is unable to stop fracture propagation.

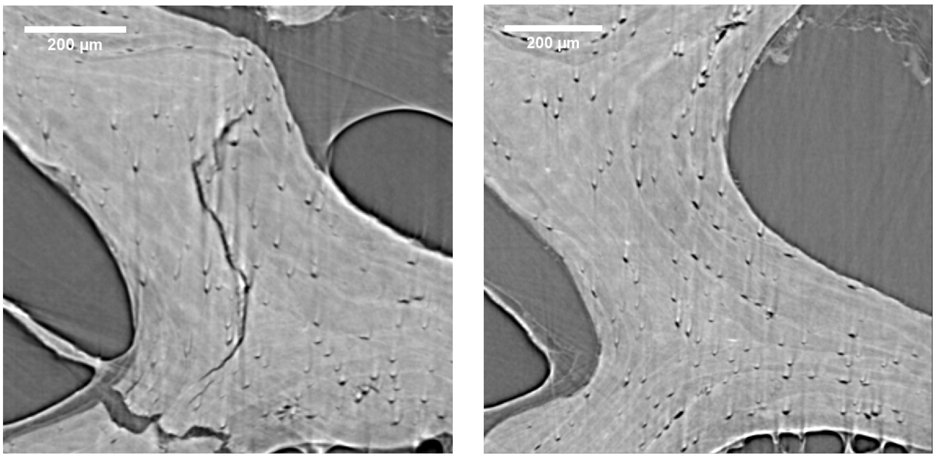

Figure 4.12: Crack following the mineralization interface line (lighter line) in FH1-S7 H3.

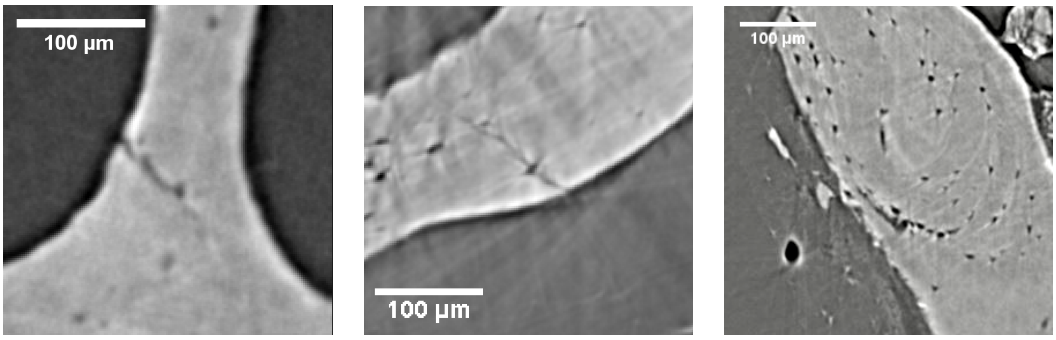

(a) crack stopped by lacuna in FH4-S31 H0

(b) crack not affected by lacuna in FH5-S33 H0

(c) crack crossing multiple lacunae in FH1-S7 H3

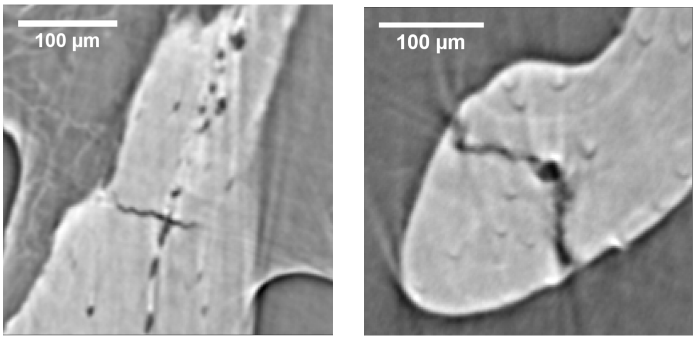

(d) Crack avoiding lacunae in FH1-S7 H3

(e) Crack crossing a macropore in FH5-S33 H3

Figure 4.13: Different crack-lacunae interactions and features.

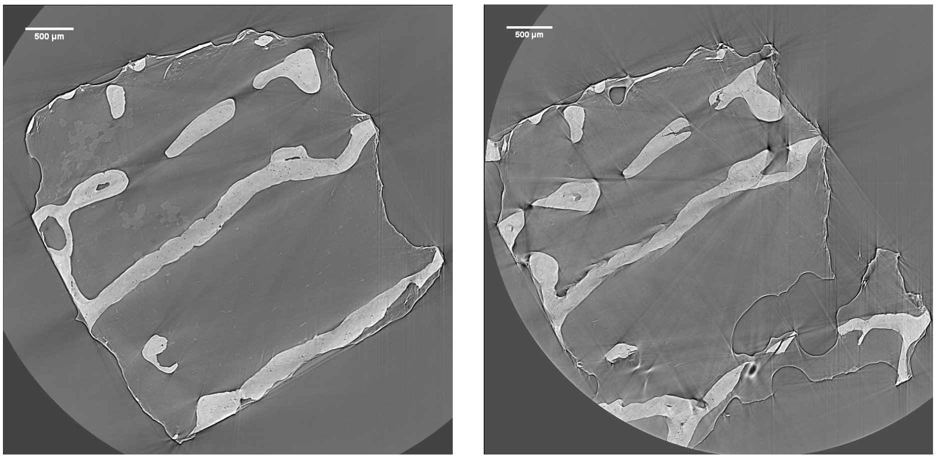

Figure 4.14: Fracture originated in formaldehyde instead of in bone, due to low BV/TV in FH2-S53.

Another discussed phenomenon is whether or not the crack path is influenced by lacunar disposition and orientation. About this aspect, we can have three different situations: cracks which are evidently guided by the lacunar disposition, especially in zones with high lacunar density (Figure 4.13c), but also cracks that do not follow at all the marked lacunar pathway, propagating along an opposite direction (Figure 4.13d). Finally, another commonly detected feature is that fractures tend to cross macro-pores and trabecular voids if they are in the surroundings of the propagation path. A remarkable example is shown in Figure 4.13e, where the crack does not cross apparently any lacuna but seems to deviate and dive into the macro-pore of that trabecula.

To summarize, numerous cracks have been examined and different types of features have been detected. Crack origin takes place generally on the trabecular surface, near bends or discontinuities, and, sometimes, from superficial lacunae. Propagation, on the other hand, is much complex, and several mechanisms can be found. Principally, propagation seems to be guided by the presence of high lacunar density zones, and, even more, by mineralization lines, that provide a preferential brittle pathway.

Also macro-pores seem to influence fracture, and often cracks are attracted by them.

One final remarkable observation must be done on the osteoporotic samples; due to their disease they show very low BV/TV, so the majority of their volume is filled with formaldehyde in the sample preparation process. As shown in Figure 4.14, there is sometimes so little bone that the compressive load bears on the formaldehyde itself, bringing to its rupture instead of bone's. This could affect the output mechanical properties, bringing to higher values, and so must be revised in future works.

4.4 Crack parameters comparisons

Examining the graphs presented in Section 3.2.5 about crack propagation velocity in different directions, it is possible to notice how the different conformation of the bone is influencing the way cracks propagate. The crack propagation velocities for non-OP samples do not display any specific trend, while for the OP ones the velocities along Z axis are visibly higher than the ones on the XY plane. This can be explained by the fact that OP bones, in general, present thin trabeculae and a lower BV/TV when compared to non-OP bones. Indeed, the thickness of the trabeculae in this work had an average value of 180 μm for the OP and 350 μm for the non-OP (up to 800 μm in the intersection points). The samples were extracted along the principal compressive direction, so the trabeculae tend to be naturally oriented in that direction; as a consequence, Z axis of the samples becomes a preferential direction for crack propagation, especially in comparison with the XY plane of the OP samples. Nevertheless, the average values of crack propagation velocities are relatively similar (Table 4.1), but this can be caused by the procedure adopted for the calculation of the velocities themselves.

For what concerns CTOD, the values measured are consistent for all the samples, as shown in Table 4.2, with values around 3-4 μm. Although, it is needed to take into

Table 4.1: Average propagation velocities along the XY plane, Z direction and their pythagoric sum for the 4 specimens.

	FH1-S7	**FH2-S53 (OP)**	**FH4-S31 (OP)**	**FH5-S33**
V_{XY} [µm/min]	17.89	7.81	12.91	11.07
V_{Z} [µm/min]	10.76	15.83	24.07	12.83
$V_{pythagoric}$ [µm/min]	20.65	18.05	21.42	17.65

account that the measures are performed at the limiting resolution for the images and, as a consequence, an intrinsic error of ±1.6 µm has to be considered. For this reason, it is not possible to easily compare the samples. Despite this, the variability of the crack-tip opening values, between 2 and 5 µm, is the result of the local state of stress acting on the trabecula as well as the presence of lacunae in which the crack is ending.

Table 4.2: Average CTOD values for each sample.

Sample	**CTOD average value [µm]**
FH1-S7	3.9
FH2-S53	3.8
FH4-S31	4.3
FH5-S33	3.1

It is interesting to compare the calculated value of K_{CTOD} to the K_{I}, as well as confronting the results considering the bone as a porous material or not. The results are displayed in Table 4.3, and it is possible to notice that, in general, there is a difference of one order of magnitude between K_{CTOD} and K_{I}, maintained in all the samples. The obtained results differ from the ones reported in literature in Section 1.5.1, of another order of magnitude. Indeed *Taylor et al.* [73] reported values of 1-5 MPa$\sqrt{m}$ for a large section of the population, from the young to the elders. Here making a distinction is important, since age affects the values of K, leading to lower values for elder people, as in our case. Moreover, all our samples come from patients who have undergone hip surgery after fracture and bone disease diagnoses, so are not in normal physiological conditions. Another aspect to be considered is that the values from the literature refer to cortical human bone, while there is a lack of data regarding trabecular bone due to its complexity. Indeed it is reasonable to advance the hypothesis of lower values of K in the trabecular bone in comparison with cortical one.

On the other hand, it is interesting to notice that accounting for bone porosity leads to values of K_{CTOD}^{bone} and K_{I}^{bone} which are very similar, and are also approaching even more the values present in literature. As a final consideration, it is important to remark that the methodology for the measurement of crack parameters performed in this work is tailored on the small dimension of the samples, and may differ from the one used in other papers [66, 3]. Moreover, the images available for this work are at an extremely high resolution (1.6 µm per pixel) that may not have been accessible to other studies. Because of that, it is possible to see very fine cracks that otherwise would not be possible to observe, leading to smaller CTOD and, consequently, an average lower value of K_{CTOD}.

Table 4.3: Comparison of K_I^{sample}, $\mathrm{K}_{CTOD}^{sample}$, K_I^{bone} and K_{CTOD}^{bone}.

Sample	# Crack	STEP	K_I^{sample} [MPa$\sqrt{m}$]	$\mathrm{K}_{CTOD}^{sample}$ [MPa$\sqrt{m}$]	K_I^{bone} [MPa$\sqrt{m}$]	K_{CTOD}^{bone} [MPa$\sqrt{m}$]
FH1-S7	1	2	$1.71 \cdot 10^{-1}$	$6.72 \cdot 10^{-2}$	$5.71 \cdot 10^{-1}$	$2.24 \cdot 10^{-1}$
		1	$2.09 \cdot 10^{-1}$	$6.89 \cdot 10^{-2}$	$6.97 \cdot 10^{-1}$	$2.30 \cdot 10^{-1}$
	2	2	$2.31 \cdot 10^{-1}$	$6.29 \cdot 10^{-2}$	$7.69 \cdot 10^{-1}$	$2.10 \cdot 10^{-1}$
		1	$2.28 \cdot 10^{-1}$	$6.47 \cdot 10^{-2}$	$7.61 \cdot 10^{-1}$	$2.16 \cdot 10^{-1}$
	3	2	$3.11 \cdot 10^{-1}$	$6.55 \cdot 10^{-2}$	1.04	$2.18 \cdot 10^{-1}$
		1	$2.11 \cdot 10^{-1}$	$6.55 \cdot 10^{-2}$	$7.05 \cdot 10^{-1}$	$2.18 \cdot 10^{-1}$
	4	2	$1.54 \cdot 10^{-1}$	$6.38 \cdot 10^{-2}$	$5.13 \cdot 10^{-1}$	$2.13 \cdot 10^{-1}$
		1	$1.81 \cdot 10^{-1}$	$6.20 \cdot 10^{-2}$	$6.05 \cdot 10^{-1}$	$2.07 \cdot 10^{-1}$
	5	2	$1.66 \cdot 10^{-1}$	$6.97 \cdot 10^{-2}$	$5.54 \cdot 10^{-1}$	$2.32 \cdot 10^{-1}$
		1	$1.89 \cdot 10^{-1}$	$6.89 \cdot 10^{-2}$	$6.31 \cdot 10^{-1}$	$2.30 \cdot 10^{-1}$
FH4-S31	1	2	$1.00 \cdot 10^{-1}$	$3.94 \cdot 10^{-2}$	$5.02 \cdot 10^{-1}$	$1.97 \cdot 10^{-1}$
	2	3	$2.87 \cdot 10^{-1}$	$4.20 \cdot 10^{-2}$	1.43	$2.10 \cdot 10^{-1}$
		2	$1.19 \cdot 10^{-1}$	$4.76 \cdot 10^{-2}$	$5.93 \cdot 10^{-1}$	$2.38 \cdot 10^{-1}$
	3	3	$1.65 \cdot 10^{-1}$	$4.25 \cdot 10^{-2}$	$8.23 \cdot 10^{-1}$	$2.12 \cdot 10^{-1}$
		2	$1.21 \cdot 10^{-1}$	$4.58 \cdot 10^{-2}$	$6.06 \cdot 10^{-1}$	$2.29 \cdot 10^{-1}$
	4	3	$1.61 \cdot 10^{-1}$	$3.94 \cdot 10^{-2}$	$8.03 \cdot 10^{-1}$	$1.97 \cdot 10^{-1}$
	5	3	$1.28 \cdot 10^{-1}$	$4.10 \cdot 10^{-2}$	$6.40 \cdot 10^{-1}$	$2.05 \cdot 10^{-1}$
FH5-S33	1	3	$4.02 \cdot 10^{-1}$	$5.84 \cdot 10^{-2}$	1.34	$1.95 \cdot 10^{-1}$
		2	$4.70 \cdot 10^{-1}$	$5.92 \cdot 10^{-2}$	1.57	$1.97 \cdot 10^{-1}$
	2	3	$3.27 \cdot 10^{-1}$	$5.93 \cdot 10^{-2}$	1.09	$1.98 \cdot 10^{-1}$
	3	3	$3.97 \cdot 10^{-1}$	$6.56 \cdot 10^{-2}$	1.30	$2.19 \cdot 10^{-1}$
		2	$4.21 \cdot 10^{-1}$	$6.04 \cdot 10^{-2}$	1.40	$2.01 \cdot 10^{-1}$
	4	3	$3.15 \cdot 10^{-1}$	$3.64 \cdot 10^{-2}$	1.05	$1.21 \cdot 10^{-1}$
		2	$3.53 \cdot 10^{-1}$	$4.12 \cdot 10^{-2}$	1.18	$1.37 \cdot 10^{-1}$
	5	3	$3.51 \cdot 10^{-1}$	$4.39 \cdot 10^{-2}$	1.17	$1.46 \cdot 10^{-1}$

Chapter 5

Conclusions

In this thesis work, part of the wider GAP project, we continued working on the mechanical tests and the mapping of mechanical properties of the femoral trabecular bone, analyzing the differences in the mechanical response between healthy and pathological (OP, OA) patients. It was possible to find interesting trends of the properties in the different zones and sub-zones, with the best results in terms of mechanical properties for Z2 zone and P sub-zone, as expected. We also improved the outcome of the mechanical tests by solving a technical problem related to the endcaps of the samples, 3D-printing new ones for a precise outcome.

Moreover, we meticulously analyzed the tomographic images obtained from synchrotron radiation, to study the behaviour of cracks and to measure the most relevant parameters. Crack's path seems to be influenced by a lot of factors as the trabecular shape and dimension, the mineralization lines, and the presence of microporosities and lacunae. In addition, a large number of toughening mechanisms have been identified and, among them, ligament bridging is the most common. In summary, we can say that cracks in OP patients mainly develop along the vertical direction of the sample, because of the low thickness of the trabeculae in the slicing plane. Furthermore, calculating the values of K based on the collected data, we found lower values than the ones reported in literature, probably because of the different methodology we used, based on direct measurement of the parameters and tailored for the small samples we have, and the bone quality of our donors. In the end, we developed a full-specimen FEM model capable of providing, with good precision, which are the most critical zones where the first fractures will form. This will help lightening the tomographic analysis procedure.

5.1 Future insights

Being this thesis work part of a wider project, which involves a collaborative network among several research institutions through many years, there is still a lot to investigate and learn about the complexity of bones. As future developments, additional experimental micro-compression tests will be carried on, considering a higher number of healthy and osteoporotic femoral heads, in order to strengthen the statistical analysis and allow a clearer comprehension of the relationship between apparent mechanical response and bone disease. Similarly, further synchrotron acquisition sessions will be useful to increase the analyzed samples and enhance crack pattern observations in both healthy and osteoporotic bones. About this topic, it will be important to develop a better acquisition timing, tailored on the specific femoral head; in this way it will be possible to detect cracks at their very first stages, allowing a more precise esteem of their propagation velocity and initiation mechanism. Finally, also the FEM computational model needs some upgrades; firstly it could be focused on a specific sub-volume of the entire sample, but with an increased resolution and a smaller mesh size, to simulate the stresses acting on a precise group of trabeculae. Then, also the lacunar network could be inserted in the model, to study its role on stresses distribution and transfer: to do so, good modelling skills and higher computational power will surely be required.

Bibliography

[1] N. Aldegaither, G. Sernicola, A. Mesgarnejad, A. Karma, D. Balint, J. Wang, E. Saiz, S. J. Shefelbine, A. E. Porter, and F. Giuliani. Fracture toughness of bone at the microscale. *Acta Biomaterialia*, 121:475–483, 2021.

[2] I. Aleixo, A. C. Vale, M. Lúcio, P. M. Amaral, L. G. Rosa, J. Caetano-Lopes, A. Rodrigues, H. Canhão, J. E. Fonseca, and M. F. Vaz. A method for the evaluation of femoral head trabecular bone compressive properties. *Materials Science Forum*, 730-732:3–8, 2013.

[3] B. A. Beda, B. A. Bedaiwi, and A. F. Abdul-Kareem. Experimental and numerical fracture toughness of human bone in linear elastic and elastic-plastic fracture mechanics in vitro. *Journal of Engineering and development*, 20(2), 2016.

[4] N. Bertolini and F. Bracco. Synchrotron-based damage analysis and micro-FE modelling in human trabecular bone. *Politecnico di Milano*, 2021.

[5] C. Bes, M. Güven, B. Akman, E. F. Atay, E. Ceviz, and M. Soy. Can bone quality be predicted accurately by singh index in patients with rheumatoid arthritis? *Clinical rheumatology*, 31(1):85–89, 2012.

[6] F. Bini, A. Marinozzi, F. Marinozzi, and F. Patanè. Microtensile measurements of single trabeculae stiffness in human femur. *Journal of Biomechanics*, 35(11):1515–1519, 2002.

[7] M. W. Bolger, G. E. Romanowicz, E. M. Bigelow, F. S. Ward, A. Ciarelli, K. J. Jepsen, and D. H. Kohn. External bone size identifies different strength-decline trajectories for the male human femora. *Journal of Structural Biology*, 212(3):107650, 2020.

[8] W. Bonfield, J. Behiri, and C. Charalambides. Orientation and age-related dependence of the fracture toughness of cortical bone. pages 185–189, 1985.

[9] M. L. Bouxsein. Bone quality: where do we go from here? *Osteoporosis international*, 14(5):118–127, 2003.

[10] F. Buccino, C. Colombo, and L. M. Vergani. A review on multiscale bone damage: From the clinical to the research perspective. *Materials*, 14(5):1240, 2021.

[11] F. Buccino, L. Zagra, P. Savadori, A. Galluzzo, C. Colombo, G. Grossi, G. Banfi, and L. M. Vergani. Mapping local mechanical properties of human healthy and osteoporotic femoral heads. *Materialia*, 20:101229, 2021.

[12] F. M. Burdekin and D. Stone. The crack opening displacement approach to fracture mechanics in yielding materials. *Journal of Strain Analysis*, 1(2):145–153, 1966.

[13] T. A. Burkhart, D. M. Andrews, and C. E. Dunning. Finite element modeling mesh quality, energy balance and validation methods: A review with recommendations associated with the modeling of bone tissue. *Journal of biomechanics*, 46(9):1477–1488, 2013.

[14] D. B. Burr and M. A. Gallant. Bone remodelling in osteoarthritis. *Nature Reviews Rheumatology*, 8(11):665–673, 2012.

[15] X. Cai, H. Follet, L. Peralta, M. Gardegaront, D. Farlay, R. Gauthier, B. Yu, E. Gineyts, C. Olivier, M. Langer, et al. Anisotropic elastic properties of human femoral cortical bone and relationships with composition and microstructure in elderly. *Acta biomaterialia*, 90:254–266, 2019.

[16] D. Casari, J. Michler, P. Zysset, and J. Schwiedrzik. Microtensile properties and failure mechanisms of cortical bone at the lamellar level. *Acta biomaterialia*, 120:135–145, 2021.

[17] L.-R. Chen, N.-Y. Ko, and K.-H. Chen. Medical treatment for osteoporosis: From molecular to clinical opinions. *International journal of molecular sciences*, 20(9):2213, 2019.

[18] D. Christen, A. Levchuk, S. Schori, P. Schneider, S. K. Boyd, and R. Müller. Deformable image registration and 3d strain mapping for the quantitative assessment of cortical bone microdamage. *Journal of the mechanical behavior of biomedical materials*, 8:184–193, 2012.

[19] B. Clarke. Normal bone anatomy and physiology. *Clinical journal of the American Society of Nephrology*, 3(Supplement 3):S131–S139, 2008.

[20] E. S. Clayton and M. C. Hochberg. Osteoporosis and osteoarthritis, rheumatoid arthritis and spondylarthropathies. *Current Osteoporosis Reports*, 11(4):257–262, 2013.

[21] E. Cory, A. Nazarian, V. Entezari, V. Vartanians, R. Müller, and B. D. Snyder. Compressive axial mechanical properties of rat bone as functions of bone volume fraction, apparent density and micro-ct based mineral density. *Journal of biomechanics*, 43(5):953–960, 2010.

[22] K. S. Davison, K. Siminoski, J. Adachi, D. A. Hanley, D. Goltzman, A. B. Hodsman, R. Josse, S. Kaiser, W. P. Olszynski, A. Papaioannou, et al. Bone

strength: the whole is greater than the sum of its parts. In *Seminars in arthritis and rheumatism*, volume 36, pages 22–31. Elsevier, 2006.

[23] J. Dequeker, J. Aerssens, and F. P. Luyten. Osteoarthritis and osteoporosis: clinical and research evidence of inverse relationship. *Aging clinical and experimental research*, 15(5):426–439, 2003.

[24] E. F. Eriksen, D. W. Axelrod, and F. Melsen. *Bone histomorphometry*. Raven Press, 1994.

[25] I. Fleps, H. Bahaloo, P. K. Zysset, S. J. Ferguson, H. Pálsson, and B. Helgason. Empirical relationships between bone density and ultimate strength: A literature review. *journal of the mechanical behavior of biomedical materials*, 110:103866, 2020.

[26] F. Galluccio. Artrosi o Osteoartrite. *www.felicegalluccio.it*, Public notes.

[27] D. Gastaldi, M. Baleani, R. Fognani, F. Airaghi, L. Bonanni, and P. Vena. An experimental procedure to perform mechanical characterization of small-sized bone specimens from thin femoral cortical wall. *Journal of the Mechanical Behavior of Biomedical Materials*, 112:104046, 2020.

[28] D. M. Geraldes. Orthotropic Modelling of the Skeletal System Diogo Miguel Geraldes. *PhD Thesis*, C(March 2013), 2014.

[29] I. Gibson and M. F. Ashby. The mechanics of three-dimensional cellular materials. *Proceedings of the royal society of London. A. Mathematical and physical sciences*, 382(1782):43–59, 1982.

[30] J. Glowacki. Osteoarthritis and osteoporosis: coexistence of osteoporosis in patients with osteoarthritis. *Minerva Ortop Traumatol*, 61(2):115–22, 2010.

[31] R. W. Goulet, S. A. Goldstein, M. J. Ciarelli, J. L. Kuhn, M. Brown, and L. Feldkamp. The relationship between the structural and orthogonal compressive properties of trabecular bone. *Journal of biomechanics*, 27(4):375–389, 1994.

[32] G. Grossi. A micro-compression device for the study of human trabecular bone local mechanical properties. *Politecnico di Milano*, 2020.

[33] A. Gustafsson, N. Mathavan, M. J. Turunen, J. Engqvist, H. Khayyeri, S. A. Hall, and H. Isaksson. Linking multiscale deformation to microstructure in cortical bone using in situ loading, digital image correlation and synchrotron x-ray scattering. *Acta biomaterialia*, 69:323–331, 2018.

[34] R. Hambli. Evaluation of apparent stress and strain at fracture of human trabecular bone under quasi-static compression load using micro-ct. (May 2013), 2015.

[35] J. G. Hazenberg, D. Taylor, and T. C. Lee. Mechanisms of short crack growth at constant stress in bone. *Biomaterials*, 27(9):2114–2122, 2006.

[36] E. Hernlund, A. Svedbom, M. Ivergård, J. Compston, C. Cooper, J. Stenmark, E. V. McCloskey, B. Jönsson, and J. A. Kanis. Osteoporosis in the european union: medical management, epidemiology and economic burden. *Archives of osteoporosis*, 8(1):1–115, 2013.

[37] T. Hollstein and J. Blauel. On the relation of the crack opening displacement to the j-integral. *International Journal of Fracture*, 13(3):385–390, 1977.

[38] M. Janssen, J. Zuidema, and R. Wanhill. Fracture mechanics: Fundamentals and applications. *Taylor & Francis*, 2:397–401, 2006.

[39] M. Kleerekoper, A. Villanueva, J. Stanciu, D. S. Rao, and A. Parfitt. The role of three-dimensional trabecular microstructure in the pathogenesis of vertebral compression fractures. *Calcified tissue international*, 37(6):594–597, 1985.

[40] K. Koester, H. Barth, and R. Ritchie. Effect of aging on the transverse toughness of human cortical bone: evaluation by r-curves. *Journal of the mechanical behavior of biomedical materials*, 4(7):1504–1513, 2011.

[41] D. L. Kopperdahl and T. M. Keaveny. Yield strain behavior of trabecular bone. *Journal of biomechanics*, 31(7):601–608, 1998.

[42] A. Larrue, A. Rattner, Z.-A. Peter, C. Olivier, N. Laroche, L. Vico, and F. Peyrin. Synchrotron radiation micro-ct at the micrometer scale for the analysis of the three-dimensional morphology of microcracks in human trabecular bone. *PLoS one*, 6(7):e21297, 2011.

[43] A. Levchuk, P. Schneider, M. Meier, P. Vogel, F. Donaldson, and R. Müller. An automated step-wise micro-compression device for 3d dynamic image-guided failure assessment of bone tissue on a microstructural level using time-lapsed tomography. *Frontiers in Materials*, 5:32, 2018.

[44] C. A. Lewinsohn. Mechanical behavior of materials by norman e. dowling, 2000.

[45] B. Li and R. Aspden. Material properties of bone from the femoral neck and calcar femorale of patients with osteoporosis or osteoarthritis. *Osteoporosis International*, 7(5):450–456, 1997.

[46] Z. C. Li, L. Y. Dai, L. S. Jiang, and S. Qiu. Difference in subchondral cancellous bone between postmenopausal women with hip osteoarthritis and osteoporotic fracture: Implication for fatigue microdamage, bone microarchitecture, and biomechanical properties. *Arthritis and Rheumatism*, 64(12):3955–3962, 2012.

[47] J. Liu, E. Curtis, C. Cooper, and N. C. Harvey. State of the art in osteoporosis risk assessment and treatment. *Journal of Endocrinological Investigation*, 42(10):1149–1164, 2019.

[48] S. Ma, O. Boughton, A. Karunaratne, A. Jin, J. Cobb, U. Hansen, and R. Abel. Synchrotron imaging assessment of bone quality. *Clinical Reviews in Bone and Mineral Metabolism*, 14(3):150–160, 2016.

[49] J. Martel-Pelletier, A. J. Barr, F. M. Cicuttini, P. G. Conaghan, C. Cooper, M. B. Goldring, S. R. Goldring, G. Jones, A. J. Teichtahl, and J. P. Pelletier. Osteoarthritis. *Nature Reviews Disease Primers*, 2, 2016.

[50] B. MF. Crack opening displacement: a review of principles and methods. *International Journal of Fracture Mechanics*, 5(4):C1–12, 1969.

[51] L. Mullins, V. Sassi, P. McHugh, and M. Bruzzi. Differences in the crack resistance of interstitial, osteonal and trabecular bone tissue. *Annals of biomedical engineering*, 37(12):2574, 2009.

[52] S. Nagaraja, T. L. Couse, and R. E. Guldberg. Trabecular bone microdamage and microstructural stresses under uniaxial compression. *Journal of biomechanics*, 38(4):707–716, 2005.

[53] R. K. Nalla, J. J. Kruzic, and R. O. Ritchie. On the origin of the toughness of mineralized tissue: microcracking or crack bridging? *Bone*, 34(5):790–798, 2004.

[54] A. Nazarian, M. Stauber, D. Zurakowski, B. D. Snyder, and R. Müller. The interaction of microstructure and volume fraction in predicting failure in cancellous bone. *Bone*, 39(6):1196–1202, 2006.

[55] S. A. Oliveria, D. T. Felson, J. I. Reed, P. A. Cirillo, and A. M. Walker. Incidence of symptomatic hand, hip, and knee osteoarthritis among patients in a health maintenance organization. *Arthritis & Rheumatism: Official Journal of the American College of Rheumatology*, 38(8):1134–1141, 1995.

[56] D. Pereira, B. Peleteiro, J. Araujo, J. Branco, R. Santos, and E. Ramos. The effect of osteoarthritis definition on prevalence and incidence estimates: a systematic review. *Osteoarthritis and cartilage*, 19(11):1270–1285, 2011.

[57] E. Perilli, M. Baleani, C. Öhman, R. Fognani, F. Baruffaldi, and M. Viceconti. Dependence of mechanical compressive strength on local variations in microarchitecture in cancellous bone of proximal human femur. *Journal of biomechanics*, 41(2):438–446, 2008.

[58] G. C. Reilly. Observations of microdamage around osteocyte lacunae in bone. *Journal of biomechanics*, 33(9):1131–1134, 2000.

[59] J.-Y. Rho, L. Kuhn-Spearing, and P. Zioupos. Mechanical properties and the hierarchical structure of bone. *Medical engineering & physics*, 20(2):92–102, 1998.

[60] R. O. Ritchie, M. J. Buehler, and P. Hansma. Plasticity and toughness in bone. *Physics Today*, 2009.

[61] F. Röder, M. Schwab, T. Aleker, K. Mörike, K.-P. Thon, and U. Klotz. Proximal femur fracture in older patients–rehabilitation and clinical outcome. *Age and ageing*, 32(1):74–80, 2003.

[62] A. Rubinacci, D. Tresoldi, E. Scalco, I. Villa, F. Adorni, G. L. Moro, G. F. Fraschini, and G. Rizzo. Comparative high-resolution pQCT analysis of femoral neck indicates different bone mass distribution in osteoporosis and osteoarthritis. *Osteoporosis International*, 23(7):1967–1975, 2012.

[63] F. A. Sabet, A. Raeisi Najafi, E. Hamed, and I. Jasiuk. Modelling of bone fracture and strength at different length scales: a review. *Interface focus*, 6(1):20150055, 2016.

[64] S. Schuit, M. Van der Klift, A. Weel, C. De Laet, H. Burger, E. Seeman, A. Hofman, A. Uitterlinden, J. Van Leeuwen, and H. Pols. Fracture incidence and association with bone mineral density in elderly men and women: the rotterdam study. *Bone*, 34(1):195–202, 2004.

[65] E. Seeman. Bone quality: the material and structural basis of bone strength. *Journal of bone and mineral metabolism*, 26(1):1–8, 2008.

[66] N. Sharma, D. Sehgal, and R. Pandey. Orientation dependence of elastic-plastic fracture toughness and micro-fracture mechanism in cortical bone. *Engineering letters*, 19(4), 2011.

[67] M. Singh, A. R. Nagrath, and P. S. Maini. Changes in trabecular pattern of the upper end of the femur as an index of osteoporosis. *JBJS*, 52(3), 1970.

[68] G. Spatafora. Optical Mechanical and Biochemical characterization of trabecular bone. 2014.

[69] H. Sugita, M. Oka, J. Toguchida, T. Nakamura, T. Ueo, and T. Hayami. Anisotropy of osteoporotic cancellous bone. *Bone*, 24(5):513–516, 1999.

[70] S. S. Sun, H. L. Ma, C. L. Liu, C. H. Huang, C. K. Cheng, and H. W. Wei. Difference in femoral head and neck material properties between osteoarthritis and osteoporosis. *Clinical Biomechanics*, 23(SUPLL.1), 2008.

[71] I. Tamimi, A. R. G. Cortes, J.-M. Sánchez-Siles, J. L. Ackerman, D. González-Quevedo, Á. García, F. Yaghoubi, M.-N. Abdallah, H. Eimar, A. Alsheghri,

et al. Composition and characteristics of trabecular bone in osteoporosis and osteoarthritis. *Bone*, 140:115558, 2020.

[72] U. Tarantino, M. Celi, C. Rao, M. Feola, I. Cerocchi, E. Gasbarra, A. Ferlosio, and A. Orlandi. Hip osteoarthritis and osteoporosis: clinical and histomorphometric considerations. *International journal of endocrinology*, 2014, 2014.

[73] D. Taylor, J. G. Hazenberg, and T. C. Lee. Living with cracks: damage and repair in human bone. *Nature materials*, 6(4):263–268, 2007.

[74] K.-i. Tsubota, Y. Suzuki, T. Yamada, M. Hojo, A. Makinouchi, and T. Adachi. Computer simulation of trabecular remodeling in human proximal femur using large-scale voxel fe models: Approach to understanding wolff's law. *Journal of biomechanics*, 42(8):1088–1094, 2009.

[75] Y. Ukon, T. Makino, J. Kodama, H. Tsukazaki, D. Tateiwa, H. Yoshikawa, and T. Kaito. Molecular-based treatment strategies for osteoporosis: a literature review. *International journal of molecular sciences*, 20(10):2557, 2019.

[76] A. Ural and D. Vashishth. Hierarchical perspective of bone toughness–from molecules to fracture. *International Materials Reviews*, 59(5):245–263, 2014.

[77] A. C. Vale, M. F. Pereira, A. Maurício, P. Amaral, L. G. Rosa, A. Lopes, A. Rodrigues, J. Caetano-Lopes, B. Vidal, J. Monteiro, J. E. Fonseca, H. Canhão, and M. F. Vaz. Micro-computed tomography and compressive characterization of trabecular bone. *Colloids and Surfaces A: Physicochemical and Engineering Aspects*, 438:199–205, 2013.

[78] R. Van der Velde, C. Wyers, E. Teesselink, P. Geusens, J. van den Bergh, F. de Vries, C. Cooper, N. Harvey, and T. van Staa. Trends in oral anti-osteoporosis drug prescription in the united kingdom between 1990 and 2012: variation by age, sex, geographic location and ethnicity. *Bone*, 94:50–55, 2017.

[79] T. Van Staa, E. Dennison, H. a. Leufkens, and C. Cooper. Epidemiology of fractures in england and wales. *Bone*, 29(6):517–522, 2001.

[80] R. Voide, P. Schneider, M. Stauber, P. Wyss, M. Stampanoni, U. Sennhauser, G. H. van Lenthe, and R. Müller. Time-lapsed assessment of microcrack initiation and propagation in murine cortical bone at submicrometer resolution. *Bone*, 45(2):164–173, 2009.

[81] C. M. Weaver, C. M. Gordon, K. F. Janz, H. Kalkwarf, J. M. Lappe, R. Lewis, M. O'Karma, T. C. Wallace, and B. S. Zemel. The national osteoporosis foundation's position statement on peak bone mass development and lifestyle factors: a systematic review and implementation recommendations. *Osteoporosis international*, 27(4):1281–1386, 2016.

[82] A. Wells. Application of fracture mechanics at and beyond general yielding. *British Welding Journal*, 10, 1963.

[83] J. Wolff. Das gesetz der transformation der knochen. *DMW-Deutsche Medizinische Wochenschrift*, 19(47):1222–1224, 1893.

[84] D. Wu, P. Isaksson, S. J. Ferguson, and C. Persson. Young's modulus of trabecular bone at the tissue level: A review. *Acta biomaterialia*, 78:1–12, 2018.

[85] X.-K. Zhu and J. A. Joyce. Review of fracture toughness (g, k, j, ctod, ctoa) testing and standardization. *Engineering Fracture Mechanics*, 85:1–46, 2012.

[86] E. A. Zimmermann, B. Busse, and R. O. Ritchie. The fracture mechanics of human bone: influence of disease and treatment. *BoneKEy reports*, 4, 2015.